SHIFTING NICHE DYNAMICS DURING ABLATION OF REG4+ SUPPORT CELLS IN THE MURINE COLONIC EPITHELIUM

by

TIMOTHY WILLIAM WHEELER

A DISSERTATION

Presented to the Department of Biology
and the Division of Graduate Studies of the University of Oregon
in partial fulfillment of the requirements
for the degree of
Doctor of Philosophy

June 2022

DISSERTATION APPROVAL PAGE

Student: Timothy William Wheeler

Title: Shifting Niche Dynamics During Ablation of Reg4+ Support Cells in the Murine Colonic Epithelium

This dissertation has been accepted and approved in partial fulfillment of the requirements for the Doctor of Philosophy degree in the Department of Biology by:

Tory Herman	Chairperson
Anne Zemper	Advisor
Karen Guillemin	Core Member
Kryn Stankunas	Core Member
Kenneth Prehoda	Institutional Representative

and

Krista Chronister	Vice Provost for Graduate Studies

Original approval signatures are on file with the University of Oregon Division of Graduate Studies.

Degree awarded June 2022

DISSERTATION ABSTRACT

Timothy William Wheeler

Doctor of Philosophy

Department of Biology

June 2022

Title: Shifting Niche Dynamics During Ablation of Reg4+ Support Cells in the Murine Colonic Epithelium

A stem cell niche is the microenvironment in which a stem cell receives the necessary signals to fulfill its specific roles to support homeostasis of its tissue. The niche of the colonic epithelium in both mice and humans are found within crypts of Lieberkühn, which are test-tube shaped invaginations comprised of several hundred cells which fulfill a variety of roles. A typical mouse colon is lined by hundreds of thousands of these stereotyped niche units, which replace their own equivalent in cells approximately once a week, making the colon one of the most proliferative tissues in the developed body. This makes it an excellent model for understanding epithelial stem cell maintenance in a mammalian context. The colon is also prone to inflammatory bowel diseases and cancers, making it a critical research target to unravel mechanisms that may underlie these disease states. Despite these factors, the colon remains a secondary target of research for murine gastrointestinal epithelial homeostasis, with the bulk of characterizing research being performed in the small intestine. A primary goal of my thesis is to lay out analysis methodology and then elucidate key molecular tissue patterns within colon crypt homeostasis to lay the groundwork for more comprehensive modeling in the mouse colon. There are two important characteristic cell types. The first are stem cells identified by Lgr5 expression and the second are secretory support cell population identified by Reg4 expression. I use transgenic reporter mice to characterize the cells that express these key markers. I further go on to ablate the Reg4+ lineage to identify perturbations within the niche. I identified a paradoxical shift in signaling that, which results in increased Notch pathway activation during ablation of Reg4+ cells, the primary supplier of Notch ligands in the colon. I also characterized remodeling of stromal cell populations within the mesenchyme surrounding crypts, implicating Reg4+ cell ablation as a mediator of epithelial-mesenchymal signaling. This is a critical avenue for future research, as mesenchymal remodeling is linked to chronic colon disease, yet no strong models exist to explore the role and mechanisms of epithelial-to-mesenchymal crosstalk.

This dissertation includes previously published co-authored material.

CURRICULUM VITAE

NAME OF AUTHOR: Timothy William Wheeler

GRADUATE AND UNDERGRADUATE SCHOOLS ATTENDED:

University of Oregon, Eugene
Colorado State University - Pueblo

DEGREES AWARDED:

Doctor of Philosophy, Biology, 2022, University of Oregon
Bachelor of Science, Biochemistry, 2011, Colorado State University - Pueblo

AREAS OF SPECIAL INTEREST:

Cell Biology
Molecular Biology

PROFESSIONAL EXPERIENCE:

Teaching Assistant, Department of Biology, University of Oregon, Eugene, 2019-2022

Analytical Technician, Boulder Scientific Company, Mead, CO, 2013-2016

Laboratory Instructor, Department of Chemistry, Colorado State University, Pueblo, 2010-2011

GRANTS, AWARDS, AND HONORS:

National Institute of Health Graduate Training in Molecular Biology and Biophysics (T32GM007759), University of Oregon, 2017-2019

ACS Division of Analytical Chemistry Undergraduate Award, 2010.

Merck/AAAAS Grant, Isolation and characterization of cellulase from *Penicillium spinulosum*, Colorado State University - Pueblo, 2010.

University Research Grant, Reactions of acylhydrazides and sulfonohydrazides, Colorado State University – Pueblo, 2008.

PUBLICATIONS:

Wheeler TW, Zemper AE. Ablation of Reg4+ support cells induces Notch-independent regeneration and mesenchymal remodeling. (In revisions, Life Science Alliance) Preprint doi: https://doi.org/10.1101/2022.01.28.478243

Stevenson JG, Ryan Sayegh R, Pedicino N, Pellitier NA, Wheeler TW, Bechard ME, Huh WJ, Coffey RJ, Zemper AE. Lrig3 restricts the size of the colon stem cell compartment. (In revisions, American Journal of Physiology, Gastrointestinal and Liver Physiology) Preprint doi: https://doi.org/10.1101/2022.03.08.483523

ACKNOWLEDGMENTS

I wish to express my sincere gratitude to Professor Annie Zemper for her assistance in preparing this manuscript and for her assistance and mentorship throughout the course of my graduate education, which was foundational to shape and grow my work into a coherent scientific endeavor, and to drive me to grow as a scientist and person. I also wish to express my sincere thanks to my committee – Dr. Tory Herman, Dr. Kryn Stankunas, Dr. Karen Guillemin, and Dr. Ken Prehoda – for their well-considered efforts to advise and help shape this project. I also wish to extend a special thanks to Bree Mohr and Natalie Pellitier for their extensive technical assistance in mouse management, and to thank Janelle Stevenson for myriad scientific discussions and general banter which helped me to get through grad school. I'd also like to express my appreciation to my parents and grandparents for helping me to get here by being a loving and supportive family, despite my insufferability. The investigation was supported in part by a funding from the National Institute of Health (T32GM007759).

This dissertation is dedicated to everyone who helped me to get here and beyond,
but especially to my Grandma, Rose-Marie,
and her dreams of becoming a biologist.

TABLE OF CONTENTS

LIST OF FIGURES

LIST OF TABLES

Table Page

CHAPTER I

INTRODUCTION

Somatic stem cells

The human body is made up of trillions cells, the majority of which are replaced and replenished many times over the course of our lifespan. We have hundreds of specialized types of cells, all with distinctive behaviors. Even within a single tissue, there can be more than ten different cell types that all arise from a single population of somatic stem cells. In order to fulfill their function, these stem cells need cues in order to direct their behavior – to proliferate to maintain their own population, to commit to differentiation and generate specialized cells, to become inactive by either quiescing or senescing, and to apoptose when necessary to remove the cell from the system. The cues that govern these behaviors can come from events from both inside the cell and from its environment, the latter coming in the form of signaling molecules, support cells, and extracellular matrix. The extrinsic cues are collectively known as a stem cell niche – the collection of extrinsic signals necessary for a stem cell to maintain its behavior (Figure 1.1). The source of these signals can vary widely depending on the home of the specific stem cell. The loose scaffold of bone marrow in which hematopoietic stem cells reside is much different from the stratified epithelium under which epidermal stem cells maintain our skin. Different niches present different models through which we can study the mechanisms of stem cell behavior, but it is also important to consider the purpose of study when selecting a model. It's generally more beneficial to select a model based on its applicability to human needs rather than for its novel nature, especially in more translational models that more closely resemble human physiology.

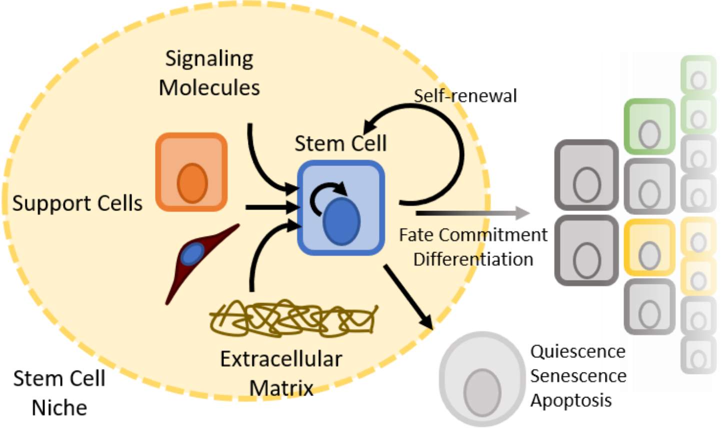

Figure 1.1. Stem cells rely on cues from a niche to direct their activity and maintain homeostasis

The colon as a niche model

A particular stem cell niche that bridges basic science to translational relevance is in the colonic epithelium. The niche of the colonic epithelium is found within crypts of Lieberkühn, which are invaginations that are stacked side-by-side like test tubes throughout this organ. This epithelium is columnar, meaning that cells form a monolayer that press together laterally, forming 'columns' in a sheet with apical and basal domains. In the colon, stem cells are found at the base of these niches, and receive their cues from support cells in the epithelium as well as the underlying mesenchyme (Figure 1.2). Progenitor cells go through 4-5 divisions to give rise to several dozen daughter cells (Snippert et al., 2010) within a transit-amplifying (TA) region located from the edge of the stem cell compartment to the mid-crypt. The upper crypt is occupied by terminally differentiated cells that are destined to be removed from the system through anoikis, a subset of apoptosis where a cell is apically extruded in coordination with surrounding cells to maintain a contiguous epithelium. The organization of the crypt tends to move in relation to an axis from the muscularis mucosa to the lumen of the colon, known as the crypt axis. This axis is the primary axis on which any intra-crypt study is modeled on. There is a rotational component of this axis that can be important if modeling for specific clonality, but generally a cross-section of a crypt is a sufficient model to understand how niche dynamics occur in aggregate. It is on this basis that most research in in this organ is founded, even extending to the gastrointestinal epithelium at large: crypt cross-sections represent the stereotyped unit within which cellular events are measured.

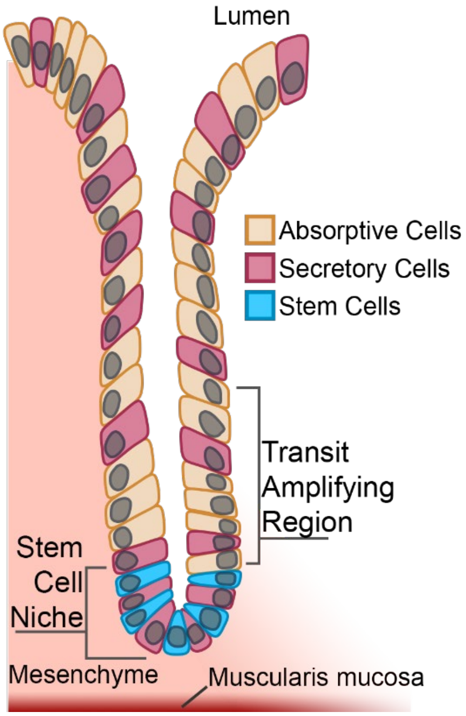

Figure 1.2. Diagram of a colonic crypt cross-section

This stereotyped structure and columnar multicellular model can allow for powerful statistical analysis. This feature is only infrequently taken advantage of in the field of crypt biology, however, which may be due to the difficulty in acquiring properly formatted data for such analysis using hand-counting methods. I address this challenge in Chapter 2 by presenting an algorithm-assisted phenotyping method which enables the collection of richer data with only a marginal increase in effort and utilizing open access image analysis tools.

Relevance of the colonic epithelium

The colonic epithelial niche is of especial interest for a few key reasons: the proliferative rate, the modeling potential, and the clinical significance. The colonic epithelium is one of the most proliferative tissues in the developed body. Since it is a columnar epithelium with cells stacked side-by-side and moving upward through the crypt during proliferation, it makes for a simple model of a complex mammalian stem cell system. The colon is also of major clinical relevance due to a high prevalence of colorectal cancer and inflammatory bowel disease (Dahlhamer et al., 2016; Xi & Xu, 2021). Many critical questions in this field are directed toward understanding the mechanisms and dynamics of these bowel diseases, and an important aspect of this is understanding the fundamental mechanisms that govern colonic epithelial homeostasis. By understanding how this system is regulated we can better understand how dysregulation gives rise to these diseases, which will give insight on how to approach the problem of restoring homeostasis from a disease state.

The mouse as a model for crypt dynamics

The tissue biology of human and mouse gastrointestinal tracts are strongly homologous (Bonis et al., 2021), making the mouse a good model for translating breakthroughs in basic science to pre-clinical medical research. Within the field of murine gastrointestinal cell biology, two areas of study stand out prominently: the dynamics of small intestinal crypts, and disease states of the colon. The latter can be understood to result from the prevalence of colon-affecting inflammatory bowel diseases and cancers in the western world (Dahlhamer et al., 2016; Xi & Xu, 2021). The former can be attributed to the identification of the highly proliferative crypts of Lieberkühn in the small intestine as a tractable model of epithelial stem cell dynamics for mechanistic study (Meineke et al., 2001; Snippert et al., 2010). However, much recent literature shows that the crypts of the colon and the small intestine are vastly different in the cellular dances that their constituent members perform to yield the key behaviors within each organ. Despite the two types of crypts sharing most of the key signaling pathways in broadly similar ways, each has its own distinct pattern of dynamics that frustrate nuanced comparisons and translation of specific manipulation techniques (Otsuka & Suzuki, 2016). As such, there's a gap between small intestinal homeostasis and colonic disease; developing an understanding the behaviors of colonic crypts in homeostasis will greatly impact how we're able to understand and thereby translate research on colonic disease. Based on this, I assembled an atlas of several important markers for cell types and pathways in homeostasis, presented in Chapter 3.

In Chapter 3, I use tissue from the distal colon to create a crypt atlas. To clarify, the colon itself is separated into a number of distinct regions, with variances in crypt dynamics and mucosal structure (E. Kim et al., 2016; King et al., 2012; Sasaki et al., 2016). Typically, the colon is separated into equidistant proximal-mid-distal or proximal-distal domains for the purpose of specifying regions of similar crypt dynamics. In my own data I have analyzed only the distal colon in a proximal-distal split. This keeps my results more constrained, creating less variance between regional differences and allowing for more specificity of interpretation.

Niche perturbation can yield novel insights

A key aspect of crypt activity lies in the pathways that govern their behavior. Bulk and single cellular characterization techniques have identified many of the key pathways regulating homeostasis of the crypt niche (Brügger et al., 2020; T.-H. Kim et al., 2016; Sasaki et al., 2016). While these techniques highlight pathways of interest, they do not address the question of how cellular constituents of this system respond to perturbations, which is a critical question when connecting this model to clinical relevance. To probe the mechanisms of disrupted homeostasis, we need to perturb the system along meaningful axes of regulation. Two of the main routes to achieve this are via chemical interference of specific pathways and perturbation of specific cell populations. The former approach can be useful for observing a systemic response but comes with the caveat of a systemic response that may not fully correspond to a more nuanced perturbation of cellular populations as we might expect in a natural perturbation scenario. The latter route of perturbing a specific subpopulation of cells has the benefit of gaining information on the contributions of that cell type by observing how the rest of the system adapts to the change. This can carry a similar caveat to chemical probes, that this may not accurately reflect a state change that could occur naturally. Conversely, this can reveal unexpected nuances in interactions and adaptations which can elucidate the inner workings of cell behaviors.

A central frontier of research in the colonic epithelium is in probing the crypt niche by injuring the system or ablating specific types of cells and measuring the outcomes of stem and other cell populations (Eichele & Kharbanda, 2017; Harnack et al., 2019; Sasaki et al., 2016; Serrano Martinez et al., 2021; Tian et al., 2011). In these approaches, the outcome is typically measured after either several days of exposure to the perturbing force, or after several days of recovery. This allows the system to stabilize into a steady state which allows for easier phenotypic resolution. However, this approach ignores the finer dynamics of cell populations as they rearrange and adapt to shifts in their system, an approach which can yield novel insights into the nuances of niche rearrangement and give new perspectives on cell behaviors (Bohin et al., 2020). In Chapter 4, I present my own research demonstrating this approach, in which I ablate an epithelial support cell population and make novel observations of a transient hyperproliferative state that is accompanied by novel shifts in signaling pathways and other niche-adjacent populations.

The primary goal of this dissertation is to convey advances I have made in methodology, background data, and experimental work expanding on the field's mechanistic understanding of the function of the murine colonic crypt. In Chapter 2, I present a new algorithm-assisted method to analyze crypts for the purpose of increased richness of data and rigor of analysis. In Chapter 3, I present an atlas of many notable markers and reporters with histological data acquired with the method described in the previous chapter, giving a unified overview of the crypt with which to base future experimentation. In Chapter 4, I use the data from the previous chapter as a control basis for a set of experiments in which I ablate an epithelial support cell population and observe a series of novel behaviors in response, including epithelial hyperproliferation, a paradoxical increase in key signaling pathways, and remodeling of the mesenchyme. These last findings offer novel and significant pathways forward for research, and the data and tools I have presented here will also serve to aid any future research in this direction.

CHAPTER II

ALGORITHM-ASSISTED CRYPT QUANTIFICATION TO OPTIMIZE INFORMATION EXRACTION

Introduction

The colonic epithelium is comprised of crypts of Lieberkuhn, test tube-shaped invaginations with a stem cell population residing at the base. Stem cells divide in the lowest portions of the crypt, giving rise to daughter cells that can fate-commit and further proliferate through a transit amplifying region in the lower crypt, giving rise to differentiated daughter cells in the upper crypt, eventually to be sloughed off into the colonic lumen.

The flow of cells within the crypt is mainly along the axis from crypt base to lumen, known as the crypt axis. As there is an obvious origin at the crypt base with cells moving upward in a single cell-thick columnar epithelium, this system can be abstracted to a linear model if we take the cross-section of a crypt along the crypt axis, with cell positions taken with respect to connections from the origin or position zero (0) cell at the base (Figure 2.1). Since a significant amount of cell interactions within this system are governed by cell-cell contact, cell connections as a metric of relative distance serves as a useful model for mapping the crypt structure with respect to cross-sections (Meineke et al., 2001). A common metric is using cell positions to map marker expression to examine expression

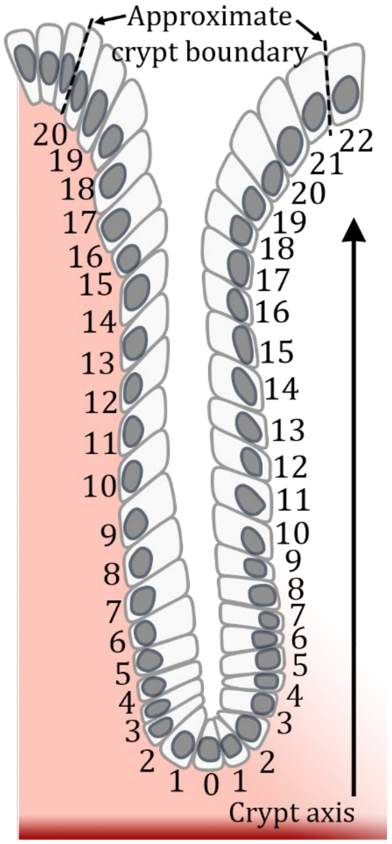

Figure 2.1. Diagram of crypt axis and positions.

domains within the crypt, yielding the field's current understanding of the structure of the stem cell niche and TA regions.

As this niche has discretely organized regions that broadly match to relative cell positions, this system has a strong potential to be phenometrically profiled by marker expression relative to cell position within the crypt. The field standard for crypt quantification is to hand-count marker frequency within the crypt, with data typically logged using spreadsheets. This can prove to be especially laborious if multiple assays are to be carried out on single image sets, as it often requires re-counting crypts for the features of interest due to the inflexible format that spreadsheet data is typically collated in. An alternative approach to this would be to annotate all epithelial phenotypes of interest and then reconstruct it with respect to individual crypts and the crypt axis. However, since there can be many crypts in a single image, simply aggregating the counts of annotations would be insufficient for the purposes of tracking how many events per crypt as well as where in the crypt this occurs. As a solution to this problem, I have designed an algorithm for the purpose of reconstructing essential crypt cross-sectional geometry to infer connectivity between cells, thereby generating crypt- and position-relative data from image annotations to create more tractable and rich data with a similar degree of effort to other hand-counting methods.

Algorithm Design

Purpose

The purpose of this algorithm is to parse annotations made on crypt images into a linearized data structure recapitulating the crypt axis, by assigning each cell a crypt position relative to the base (Figure 2.2). This data format is intended to create data that allows for

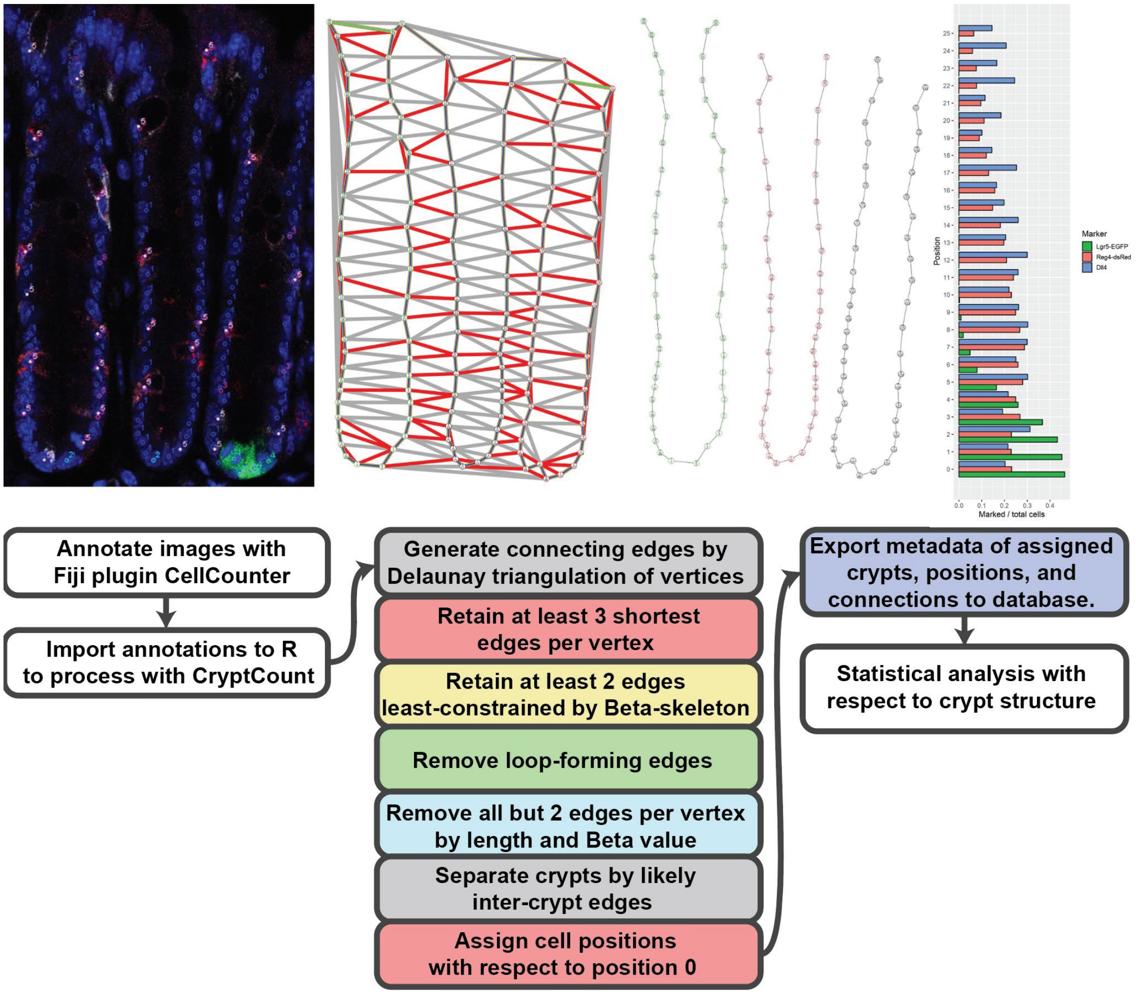

Figure 2.2. A graphic overview of the CryptCount algorithm

Images of crypt cross-sections are annotated by hand (left), processed through several logical and parametric steps (middle), and aggregated as data for connected points with example positional expression graph (right).

flexible and comprehensive analysis. This format is intended to provide more flexibility in data handling compared to hand-counting methods, by allowing re-analysis and auditing without needing to re-count images.

Data Structure

The data structure that the algorithm parses is an XML annotation file generated using the Fiji plugin Cell Counter (v3.0.0+) (https://imagej.net/plugins/cell-counter). Only cross-sections of whole crypts which extend from the muscularis mucosae to the lumen should be used for both robust application of this algorithm and representational accuracy of accumulated data. This algorithm is designed with the assumption that each crypt is contiguous, so only complete crypts from base to lumen should be included. A z axis may be used as a component of determining a contiguous series of cells so long as only a single column of cells per each side of the crypt are used. Columns of cells within whole crypts must be annotated using a marker type which labels it as a cell (“nuclei”, “cell”, “DAPI”). All position 0 cells within the crypt must also be labeled to indicate the crypt base (“0”, “pos0”). Markers of interest from probes or reporters that can be designated with a binary response (i.e. is a cell positive or negative) should be included (Figure 2.3).

The data structure of processed files takes the form of a nested series of classes. The first level is a CellCounterDatabase, which aggregates individual cell data with respective metadata from image and crypt of origin, along with coexpression, position, any other added experimental metadata added by the user, along with references to CellCounterObject classes. The next level is the CellCounterObject class, which stores the overall data loaded from XML annotation files, associated image metadata, processed vector data, and CryptObject class references. The final level is the CryptObject class, which contains specific positional structure related to vectors from the parent CellCounterObject class. Package and source code is available at: https://github.com/twheele3/ccproc

Technique

Images are loaded into Fiji/ImageJ and annotated using CellCounter, identifying single columns of cells per each side of contiguous crypt using a marker designated as cell, nucleus, or DAPI. Crypt base cells are labeled as position 0 cells with a marker designated as pos0. Any other reporters or probes that can have a binary response (TRUE/FALSE) are labeled with additional markers designated as appropriate (Figure 2.3B). Markers are exported as XML annotation files, which are loaded and parsed into R using CryptCount package. Files are parsed as two-dimensional vertex data based on cell markers. Cells are tagged as TRUE or FALSE for secondary marker channels based on secondary label proximity to the primary cell label. Specific cells designated as position 0 (pos0) cells are used to determine the number and starting point of crypts.

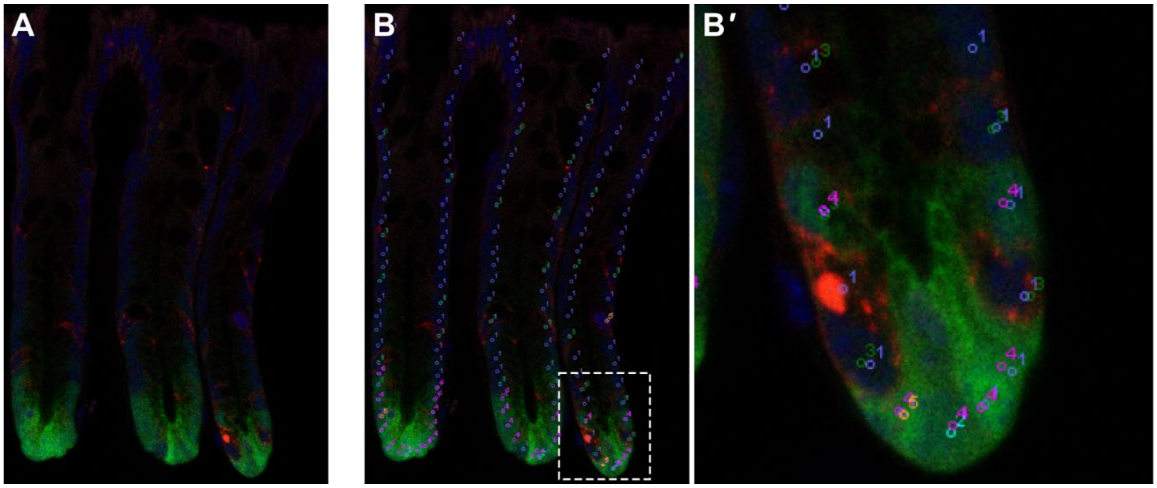

Figure 2.3. Images are annotated in Fiji using the CellCounter plugin

A. Image of crypts with several reporters in red and green, with nuclei marked in blue. **B**. Image of annotated crypts. All cells are marked with 'cell' labels (type 1, blue), with one cell at the base of each crypt additionally marked with 'pos0' label (type 2, cyan). Reporters and other stains are marked with additional labels as applicable (types 3-5). Non 'cell' markers are associated with the nearest 'cell' marker.

A Delaunay triangulation is generated for all cell vertices (Figure 2.4), which describes a set of non-conflicting connections (edges) between vertices (Shewchuk, 1996). This method is used as it optimizes for the set of triangles which are as close to equilateral as possible, which tends include likely meaningful connections within the vertices. This makes it a good foundation to generate a meaningful pattern through erosion of edges through a series of logical and parametric decisions. The goal of this series of erosions is to reduce the number of edges to a maximum of two edges per vector, to represent the linear set of cells assembled in the cross-section of a crypt. Each vertex begins with a set of edges describing the Delaunay triangulation. Subsequent steps of this algorithm erode these edges through a series of logical and parametric decisions until each vertex has a maximum of two edges, to represent the linear set of cells assembled in the cross-section of a crypt.

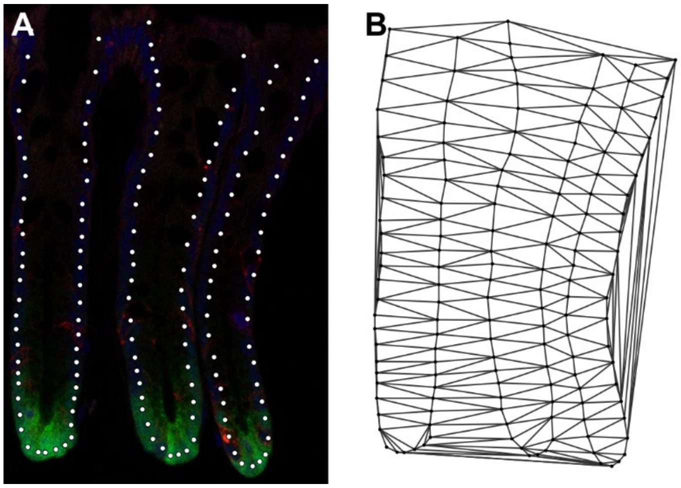

Figure 2.4. Crypt annotations are used to generate a Delaunay triangulation
A. Image annotations are processed to vector data based on markers designated 'cells'. **B**. A Delaunay triangulation of vector data.

Edges are first eroded to include the shortest three edges per vertex (Figure 2.5). Retained edges are unified between sets for different vertices to prevent premature decoupling of paired cells by over exclusion. My rationale for including three edges per vertex is to prevent exclusion of truly adjacent cells that are not as apparently close as a proximal cell in another crypt, which can be a common occurrence in tightly packed mucosa. This step tends to remove edges between separate sides of a crypt, longer inter-crypt edges, and structural edges formed as part of the Delaunay triangulation generating all possible non-conflicting edges.

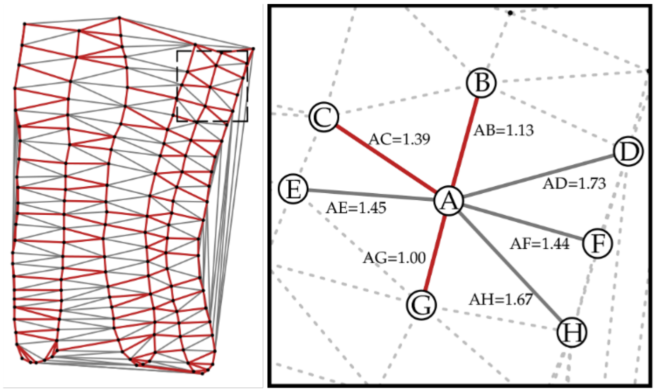

Figure 2.5. Edge erosion by distance

(left) Edges are eroded by distance relative to other edges per vector. Retained edges are labeled in red, with discarded edges labeled in gray. Each vector retains its the 3 shortest connected edges, inclusive between vectors. (right) Example set focused around center vertex A, with 3 shortest edges (AG, AB, AC) highlighted in red, other connected edges in solid grey, and unconnected edges in dashed grey. Values given in arbitrary units of length.

Edges are next eroded by selecting for edges that are more linear with each other. To accomplish this, I chose an approach that approximates a β-skeleton method which selects for edges which are more distant from other vertices (Adamatzky, 2013). However, a β-skeleton takes a parametric approach to set a threshold to erode edges, which differs from my approach of choosing a subset based on ordered values. As a proper β-skeleton method tests all points against each other, I instead opt to approximate a β value by only calculating for adjacent partners as defined by Delaunay triangulation to save on calculation time. As such, I define β_{edge} in this case to mean the maximum angle between the two angles opposite each edge, such that if edge AB is part of triangles ABC and ABD, then β_{AB} will be the maximum of angles θ_{ACB} and θ_{ADB} (Figure 2.6). Each vertex retains the two edges with the lowest β inclusively as per the previous erosion step. The rationale for this step is that β calculated as such tends to indicate the relative proximity of other points to each edge. The closer that a proximal point is to an edge, the larger the angle. The smallest β values between edges for each vertex tend to indicate the least conflicting probability of a different edge being a real connection. This tends to leave a largely contiguous and unbranching set of edges that resemble the desired crypt architecture.

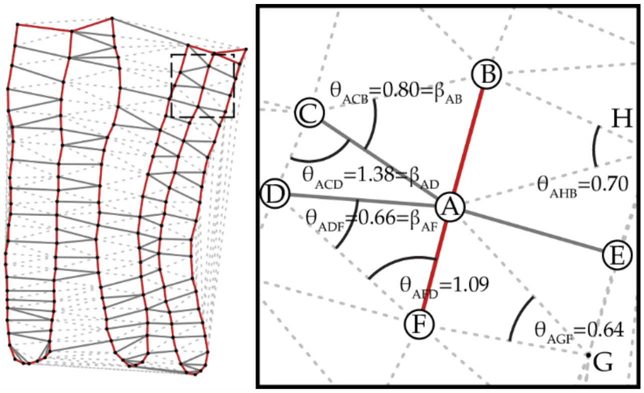

Figure 2.6. Edge erosion by angle

(left) Retained edges are labeled in red, discarded edges labeled in solid gray, and Delaunay triangulation labeled by dotted lines. (right) Each vertex retains the two edges with the smallest β values, defined as the maximum angle with respect to the angle opposite the edge in each component triangle. In example, for edge AF, θ_{ADF} is the larger compared to θ_{AGF}, and is used as β_{AF}. Angles given in radians.

Edges are further eroded to remove non-linear (looping) segments. By this stage, most edge sets will resemble the intended morphology with only a few instances of extraneous edge retention. Based on this, edges are eroded if each vertex is a component of 3 or more edges (Figure 2.7). This removes edges that overconnect contiguous sets of vertices. This is a functional step at this stage due to the rarity of paired vertices retaining 3 or more edges, otherwise it would likely erode too many edges creating gaps between significant vertices.

A final erosion is performed to retain a maximum of two edges per vertex exclusive to other vertices to prevent any instances of a single vertex retaining more than 2 edges. The comparative statistic C_{edge} for this case is $C_{edge} = l_{edge} * \beta_{edge}$, where $\mathrm{l}_{\mathrm{edge}}$ is the edge length and β_{edge} is the maximum angle formed by opposing triangles as described in Figure 2.6. This statistic is used to attempt to retain edges that are shorter and more likely

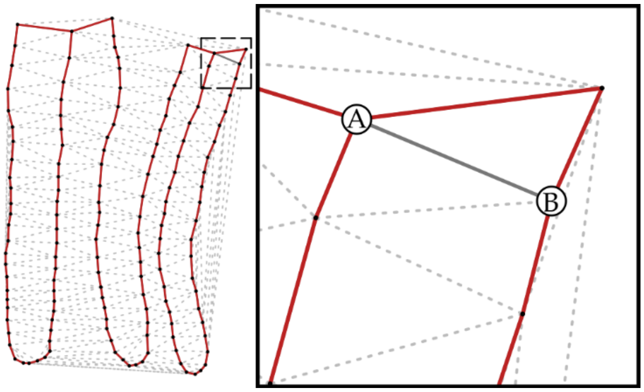

Figure 2.7. Looping edge segments are eroded

Edges are eroded if each vertex has 3 or more edges. Retained edges are labeled in red, with discarded edges labeled in solid gray, and Delaunay triangulation labeled by dotted lines. Edge AB is eroded as vertices A and B are both connected by 3 or more edges.

linear with connecting edges. This step is useful for eroding edges at the top of crypts, generally either edges across the opening of or between crypts (Figure 2.8). This leaves one or more linear sets of vertices which can be treated as an ordered vector. These ordered vectors can then be processed into crypts after identifying which edges represent transitions, either across the top of a crypt or between crypts.

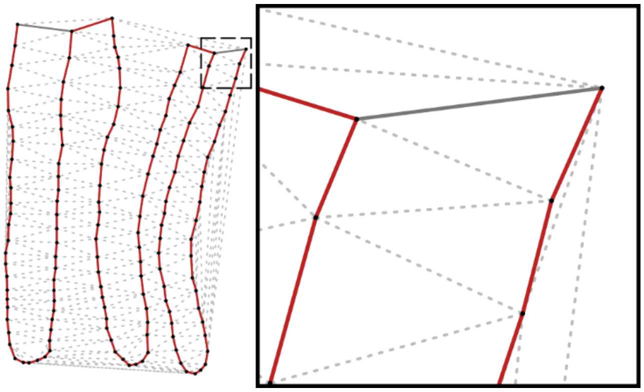

Figure 2.8. Edges are eroded by length and angle to permit no more than two connections per vertex

Vertices with 3 or more edges are eroded to 2 edges based on length and opposing angles. Retained edges are labeled in red, discarded edges labeled in solid gray, and Delaunay triangulation labeled by dotted lines.

Linear sets of connected vertices are assembled into vectors of vertices spanning between crypt origins with edges then parametrically selected to cut to separate vector sets into separate crypts (Figure 2.9A). Vertices which were annotated as crypt origins (position 0 cells) delineate start and end points for each parametric determination window, with the edge to cut within this window determined by calculating C_i for each edge i within the vector edgeset n such that

$$C_i = \widetilde{l_i} * \theta_i * \Gamma_i$$

where $\widetilde{l_i}$ represents a normalized length factor, θ_i represents dihedral angle, and Γ_i represents the connections from each pos0 vertex. The length factor $\widetilde{l_i}$ is described as $\widetilde{l_i} = 1 + \left(\frac{l_i - \mu_l}{\sigma_l} \right)^2$ indicating that edge length l_i is normalized to vector mean length μ_l and standard deviation σ_l, further taking the square plus one to create a baseline multiplier that increases as it deviates from vector mean. θ_i indicates the dihedral around an edge from the adjacent edges such that for edge BC in edgeset $ABCD$, the angle θ_{BC} is taken from $\cos^{-1} \overrightarrow{AB} \cdot \overrightarrow{CD}$. The connection distance term $\Gamma_i = \log i * \log(n - i)$, indicating the relative connected distance from the origin vertices, which increases the likelihood that the highest C value will be distant from either origin. All of these parameters unify to identify edges which are unlikely to be connections between columnar epithelium and likely to be distant from crypt bases. This is demonstrated in Figure 2.9B, where the maximum represents the edge bridging separate crypts, with selected edges shown separated in Figure 2.9C.

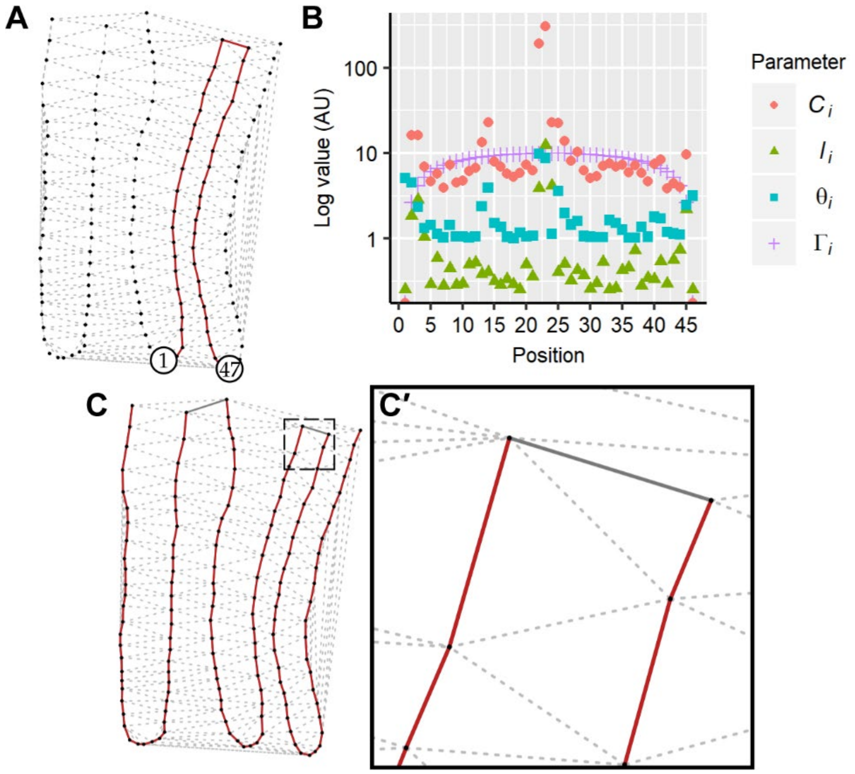

Figure 2.9. Vectors are separated into crypts by parametric analysis between crypt origins

A. A single line of vectors spanning two crypts is highlighted, representing a set of vertices to be separated by determining the most likely edge. B. Normalized length (l_i), dihedral angle (θ_i), and connected distance (Γ_i) parameters of each edge (A) are shown separately and multiplied together to make a single determinant parameter C_i. C. Edges between crypts with the largest determinant parameter C_i are eroded, leaving separate sets of arranged vertices.

After this step, all crypts are separated and each cell is set in a position in a linear vector, which allows each cell to be assigned a position relative to the number of connections from the origin cell (pos0). This data may be mapped showing all connected cells per crypt, allowing visual identification and debugging of any errors within the algorithm (Figure 2.10). Each cell vertex is then loaded into a database with metadata information on image of origin, assigned crypt, position within the crypt, and associated secondary markers such as antigen expression. This is the final data form and now ready for processing and statistical analysis.

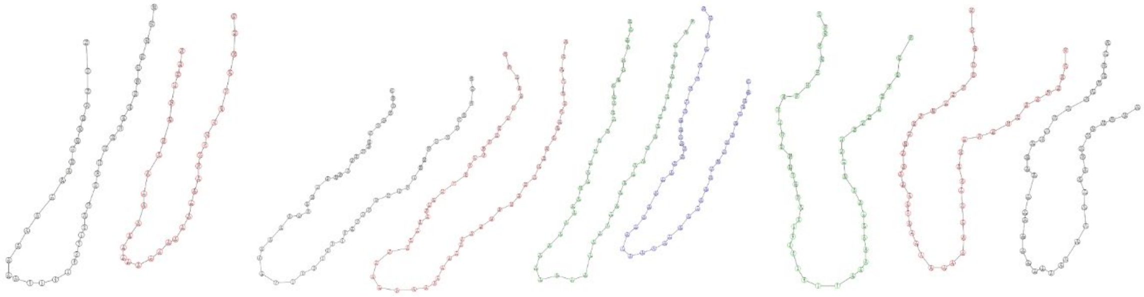

Figure 2.10. Example debugging images of crypt data after algorithm processing

Justification

This algorithm is intended to translate raw positional count data into the context of the whole crypt with positional nuance while giving the user the ability to verify the output. Throughout the course of my work, I've processed 1858 images; approximately 30-40 required correction after initial processing. This represents a 98% initial success rate, with the remainder able to be corrected. Correction involved slight shifts to the position of markers to better conform to the algorithm's rules to allow for processing; these changes typically shift the vertex less than a micron and should not significantly impact any statistical outcomes. Since debug images can be easily generated and visually scanned to verify and correct any algorithmic errors (Figure 2.10), this represents a reliable method to obtain rigorous, reproducible, auditable, and rich data. A caveat to my own processing success rate: since I personally developed the rules of this algorithm, it would be expected that I intuitively adjust my annotations to smooth the processing; this set of rules may not hold up as well in others' hands or with their crypt tissue. However, as the software package includes debugging tools, this should be correctable by the end user. Additionally, when building this algorithm, I had to set up a series of tools to execute the logical scanning over edge sets. I developed these tools with flexibility in mind, to allow for future development and refinement of similar algorithms. These tools can be applied by others through experimentation to develop and refine two-dimensional tissue parsing and connectivity analyses.

This method of data collection is slow compared to classic hand-counting methods, taking 3-5 minutes per image to annotate and 3-5 seconds per annotation file to compute as compared to 1-2 minutes with direct entry of count data into a spreadsheet. The slower speed can lead to substantial processing times in especially large datasets. The richness of data is enhanced in this algorithm versus transcribing count data to a spreadsheet, as nested positional data is retained and can be mined later. The processed results can be stored and reloaded instantly for immediate postprocessing and auditing, demonstrating more utility for reproducibility than hand-counting.

Discussion

This algorithm presents a method to expand the richness of data derived from crypt analysis with a small increase in user investment at the start. This method generates data which can be used for rich nested analyses including positional, coexpressional, and juxtacrine information (for examples see Chapters 3,4). These analyses only require the analyst to conceive of a framework to process the data from the database, which is an important distinction compared to classic hand-counting methods; if a user wished to conduct a new analysis using classically hand-counted data, they would have to re-analyze all the images in their dataset again by hand. This method also provides an auditing trail for image analysis, giving the ability to trace each count to a specific cell on an image, and allowing greater flexibility in reviewing data processing. Since this method is only parsing user-generated annotations into a geometric context, it should retain the full data reliability of classically hand-counted data.

Data derived from this algorithm may prove useful to integrate into statistical models of crypt function. There has been a significant amount of theoretical work on the formation of crypt morphology (Almet et al., 2020; Ingham-Dempster et al., 2017; Kagawa et al., 2014), but it has remained problematic to unify theory with experimental results. This dataset and future potential data derived from this sort of algorithm could prove invaluable in legitimizing theoretical models based on empirical measurements.

This algorithmic method also has other potential future applications for further development and use. This algorithm presents a method to form raw annotations into meaningful patterns for tissue analysis. While it presently requires a significant amount of annotation-based orientating (requiring user input on crypt position 0), it may be further refined to identify structures and crypt orientations by geometry alone. Ideally, this structural analysis might in the future be paired with automated image annotation to fully automate the processing of data for higher throughput. As a caveat to this approach, the microenvironment that the colonic epithelium inhabits is prone to significant amounts of noise and false positives for probing within the upper lumen and mesenchyme, so this higher throughput data would need to offset any decreased accuracy that automated image analysis may have. This would still likely prove a net benefit, as researchers may spend more time focusing on generating high quality images and contemplating meaningful interpretations of their analyzed data. This method would also likely allow the recovery of more metric data than with classical methods as more crypts are more comprehensively quantified.

This approach also represents a bit of a step aside from a classical mode of thinking in the mammalian biological sciences: qualitative observation is often placed above phenomic quantification. Yet, in our increasingly computerized world we have the potential to quantify classically qualitative events. Data acquired in this fashion should be regarded with a skeptical eye due to the complexities involved in any tissue context, but also with a discerning eye with regards to how to best integrate these sorts of digitized technologies with analog nuances to yield a more complete whole of data with available resources.

Bridge to Chapter III

In this chapter I have demonstrated a novel analytical platform for measuring the colonic epithelium. This method allows the collection of versatile data from histological imaging, which is the gold standard of phenotypic measurement in the colonic epithelium. In Chapter 3, I utilize this algorithmic method to collect a series of characterizing data for the colonic epithelium, creating an atlas of the colonic crypt which details frequency, position, and coexpression of many markers of importance in crypt homeostasis.

CHAPTER III

AN ATLAS OF THE DISTAL COLON CRYPT WITH RESPECT TO REG4- AND LGR5-REPORTING CELLS

Introduction

The distal colonic crypt represents a model to explore stem cell niche dynamics in a mammalian context with a high degree of clinical relevance. However, to properly utilize this model we must first have a good understanding of the dynamics of the crypt in homeostasis. Many modern experimental techniques have been put to effective use in characterizing cell expression profiles by transcriptomics, proteomics, and epigenetics, generating data characterizing a diverse and nuanced range of cell types within the colonic epithelium. However, as these techniques tend to rely on cell dissociation, we tend to lose resolution of cell identity and localization with respect to the crypt and tissue. To understand how the cell expression relates to epithelial structure we must physically observe these markers in the context of their environment by using histological probes. Within the literature this is typically only done within the context of a specific experiment as a control, making it difficult to access a breadth of markers identifying cell types and behaviors, especially with respect to uniformity of data acquisition and measurement. This sort of data can be invaluable for planning studies, from gaining an understanding of the histological resolution available by a probe to having the statistical data available to predict a power analysis.

These are some of the goals I set out to fulfill with the data in this chapter. I have acquired an extensive amount of control data from the mid-distal colon across many markers of interest to crypt biology, processed through the algorithm described in Chapter 2. This characterization data provides immunofluorescent images to give a baseline expectation for future experimental imaging, as well as providing statistical data of marker frequency as well as positionality with respect to the crypt axis.

In addition, the mice used to generate this data were from transgenic reporter lines. A transgenic reporter has a gene for a detectable protein or peptide sequence inserted downstream of a promoter for a marker gene of interest. In this case I utilised two fluorescent reporter lines to conduct coexpression analysis, helping to identify correlation between markers of interest and the reporter cell lineage. The first reporter is based on the *Lgr5* gene, which in the colonic epithelium is characteristically expressed exclusively in stem cells. This makes the mouse reporter line of $Lgr5^{tm1(cre/ERT2)Cle}$/J useful for stem cell respective coexpressional analysis, as an *EGFP* green fluorescent protein is expressed from the *Lgr5* promoter (*Lgr5-GFP*) (Barker et al., 2007). The second reporter line used is $Reg4^{tm1(HBEGF/DsRed)Cle}$/J, with a component of its transgenic expression comprised of a *dsRed* red fluorescent protein from the *Reg4* promoter (*Reg4-RFP*). *Reg4* is a marker for epithelial secretory support cells, defined as a support cell based on the loss of *Lgr5* expression after ablation of the *Reg4* cell population (Sasaki et al., 2016). In this chapter I present data utilizing small cohorts of $Reg4^{dsRed}$ and $Reg4^{dsRed};Lgr5^{EGFP}$ transgenic mice, which allowed me to conduct coexpressional analysis of markers with respect to these reporters and therefore gain the ability to determine whether markers of interest might be correlated to either lineage of reporting cells.

Within this chapter I aim to provide a more comprehensive and unified perspective of the colonic crypt with histological data, with the goal of providing a solid frame of reference for future research. As I am presenting a spectrum of data, I present discussion alongside contextualizing some of the state of knowledge and relevance to each point.

Results and Discussion

The morphimetry of crypt cross-sections

To begin my presentation of crypt data, I want to first give an outline of some key crypt parameters to lend some context to future metrics. In crypt histology, we see cross-sections of a 3-dimensional structure that presents as columns of cells extending through the mucosa (Figure 1.2). All the data I present are taken from crypt cross-sections that only are contiguous from near the muscularis mucosa to the lumen. Due to the organic nature of this system, despite the stereotyped nature of crypt subunits, it is common for the crypt axis to be bent or out of plane to some known or unknown degree. Similarly, any count data is merely taking an effectively random two-dimensional sample from any given crypt, rather than identifying the full three-dimensional quantity of a cell population within that crypt. As such, any crypt metric data comes with several degrees of intrinsic error with respect to total counts and actual position relative to crypt axis and crypt base. Using my crypt counting algorithm (see Chapter 2), I was able to collect several different measures of crypt morphology to better assess the structure, key statistics, and correlation of morphometry with active regions of the crypt. The median maximum position within crypts was 22 cells (Figure 3.1A). I used this median maximum as a maximum point to display positional data of marker expression in subsequent characterization data; since count data diminishes past this positional mark, any positional statistics taken above it would be increasingly prone to outliers and so I judged them to be of too poor in fidelity to include. The curvature of the crypt cross-section was acutely increased below position five (Figure 3.1B), which comports with the established region that the niche resides; positions 0-4 are typically regarded as the stem cell niche region within the colonic epithelium (Barker et al., 2007).

This correlation between curvature and niche region may suggest that the curvature plays a function in specifying stem cell position or enabling stem cell behavior (or likely both). Cells within the crypt have a lateral diameter of 5-6 microns near the base of the crypt and through the TA region, expanding to 6-8 microns as they fully differentiate in the upper crypt (Figure 3.1A). Crypt length in absolute distance is occasionally used as a metric but comes with a caveat that histological sectioning often warps the tissue, introducing errors that confound absolute measurements along this axis. As such, this data should be used more as an indicator of a general trend that epithelial cells tend to expand in lateral size as they move upward along the crypt axis.

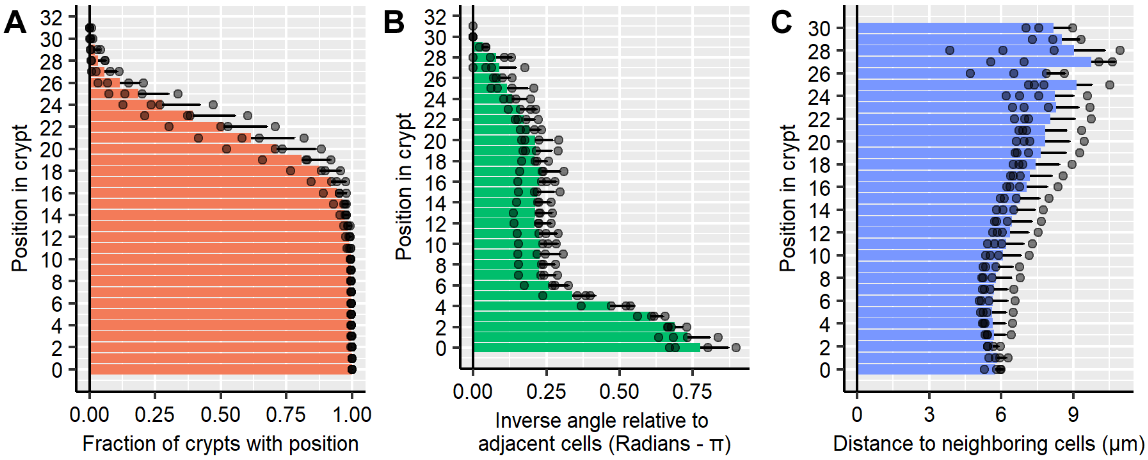

Figure 3.1. Summary morphometric statistics of murine colonic crypts

A. Normalized cells per position indicate overall number of cells from base of crypt to crypt cuff. B. Inverse angle (radians - π) is given with respect to adjacent cells, indicating average curvature of the epithelium relative to position. C. Distance to neighboring cells given per position, approximately equating to cell diameter on the lateral axis.

Comparative analysis of reporters for Lgr5 stem cells and Reg4 support cells

Lgr5 is a determinant stem cell marker in the murine colonic and small intestinal epithelium. However, no functional antibodies have yet been reported for probing Lgr5 protein in histology, instead requiring *in situ* hybridization methods for detection of *Lgr5*.

These methods can be problematic for studies seeking to analyze coexpression, as *in situ* hybridization typically requires heat and chemical treatment which denatures sensitive antigens (Ramos-Vara & Miller, 2014). In lieu of this, I used an Lgr5-GFP reporter line to quantify Lgr5-lineage stem cells co-expression in a more permissive environment. This *Lgr5-GFP* reporter line has two notable caveats: perdurance and incomplete penetrance. GFP tends to perdure within cells for hours to days beyond the original point of expression, which often leads to the appearance of a gradient that streaks upward from the base of reporting crypts. I compensated for this in my analysis by only counting cells with intense GFP signal as Lgr5-GFP+ cells. The second issue of incomplete penetrance is an epigenetic property of this reporter line in which only a subset of all crypts express the reporter. In my own results, only 68% of total crypts express any GFP (Figure 3.2F), and even this number is an overestimate as I was biased toward imaging fields with GFP-expressing crypts. As a consequence of this partial penetrance, I have only included counts with any Lgr5-GFP+ crypts for co-expression statistics with respect to Lgr5-GFP reporting cells. Lgr5-GFP is most expressed in positions 0-5, tapering toward the edge of this region (Figure 3.2C). This comports with *Lgr5 in situ* hybridization which shows that expression is constrained to the 0-4 positions (Figure 3.3C), and with literature which indicates the same region of expression (Barker et al., 2007). However, there is nearly twice the number of Lgr5-GFP+ cells as there are *Lgr5*+ cells (Figure 3.2B, Figure 3.3B), further indicating some of the issues of perdurance with respect to this reporter and indicating that expectations should be tempered with respect to Lgr5-GFP coexpression. Of other note within the Lgr5-GFP+ region, reporting cells make up less than half of all cells, indicating that supporting cells may be retained past the point of perdurance in juxtaposition to stem

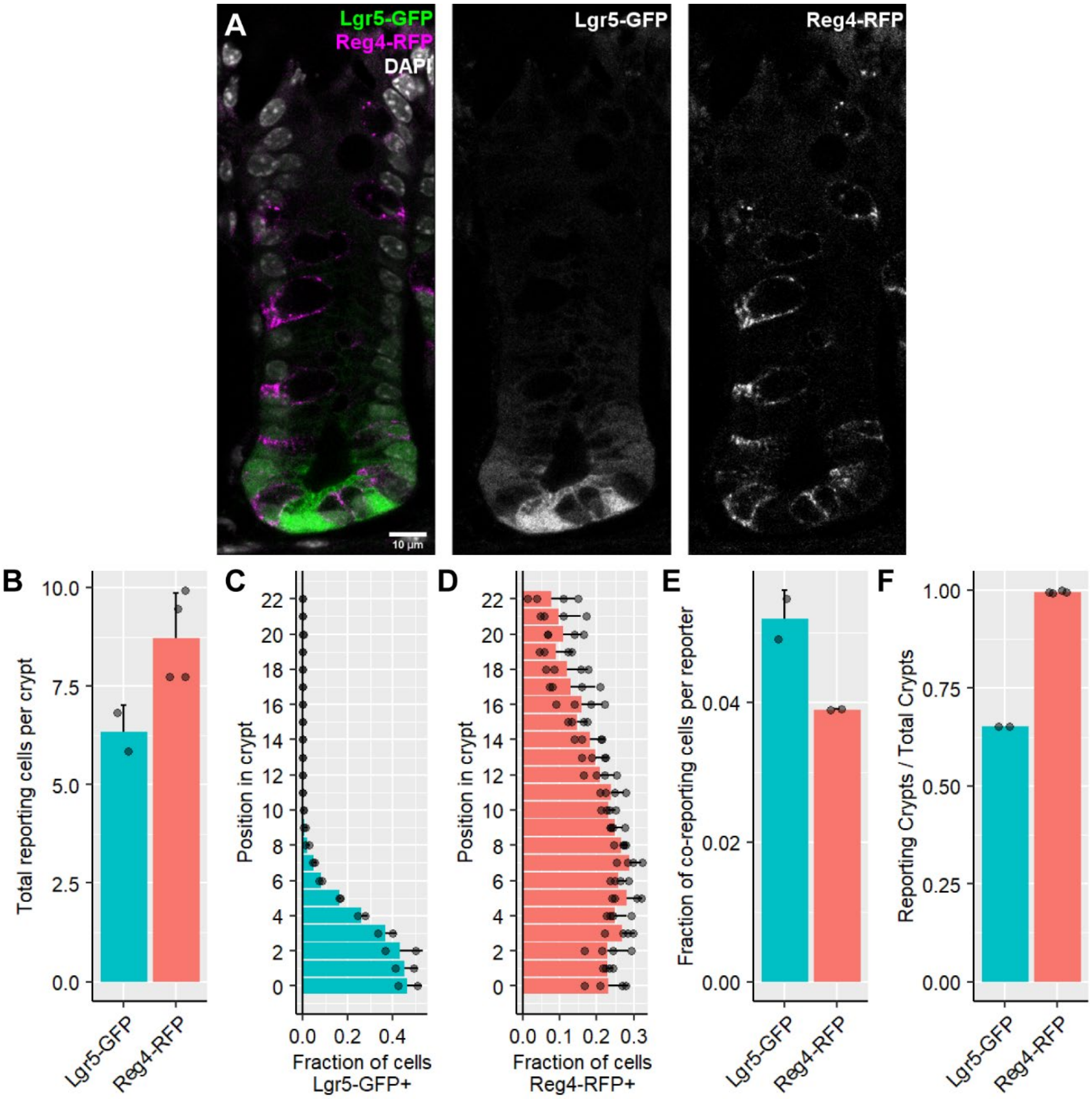

Figure 3.2. Morphometrics and coexpression of Lgr5-GFP and Reg4-RFP reporters

A. Histology of a colon crypt from an *Lgr5-GFP;Reg4-RFP* reporter mouse, with nuclei indicated by DAPI. B. Total reporting cells per crypt are given with respect to individual reporters. C. Fraction of cells reporting Lgr5-GFP per position. D. Fraction of cells reporting Reg4-RFP per position. E. Fraction of indicated reporting cells that coexpress the other reporter (e.g. Lgr5-GFP+;Reg4-RFP+ over total Lgr5-GFP+ cells). F. Crypts that contain any reporting cells over total crypts counted per sample. Biological replicate n = 2 mice for Lgr5-GFP;Reg4-RFP, 4 mice for Reg4-RFP. 150-200 crypts per mouse. Barplots and error bars represent overall mean ± sd, with points indicating individual mouse means.

cells. Further data taken from Reg4-RFP reporting cells indicates that these adjacent cells express Reg4-RFP (Figure 3.2A); these cells often lack even middling levels of GFP expression, which suggests that these cells are retained long enough for perduring GFP to be eliminated. As with Lgr5-GFP, the Reg4-RFP reporter perdures throughout the length of the crypt, although there is a distinct concentration of Reg4-RFP+ cells in the lower half of the crypt (Figure 3.2D). There is only a small amount of coexpression between Reg4-RFP and Lgr5-GFP going in both directions (ie, indicating that neither is a subset of the other) (Figure 3.2E). The *Reg4-RFP* reporter line indicates full penetrance of reporter expression (Figure 3.2F), indicating a greater reliability for use in coexpressional analysis.

Lgr5 marks colonic epithelial stem cells

Lgr5 is an effector of canonical Wnt/R-spondin signaling that assists in maintaining Wnt-related transcriptional activity (Leung et al., 2018). In the colonic epithelium, it is only expressed by the furthest upstream stem cells in homeostasis (Barker et al., 2007). One problematic aspect of Lgr5 as a marker is that there has been no success to date in developing an antibody for immunohistology, and reporter lines have poor penetrance (Figure 3.2F). *In situ* hybridization can reliably detect *Lgr5* (Figure 3.3A), although this process tends to be incompatible with coexpression analysis as it tends to denature reporter proteins and many antigens (Ramos-Vara & Miller, 2014). There tend to only be a few *Lgr5*+ cells per crypt (Figure 3.3B)., and these are concentrated below position 4 (Figure 3.3C). These cells tend to be narrow compared to surrounding secretory support cells which interdigitate the crypt with them.

Reg4 is expressed by secretory cells in the lower crypt

A subset of secretory cells characterized by Reg4 expression was identified as a supporting cell population to Lgr5+ stem cells (Sasaki et al., 2016). Reg4 is a protein that has been associated with Egfr activation and enhancement through the Akt pathway, as

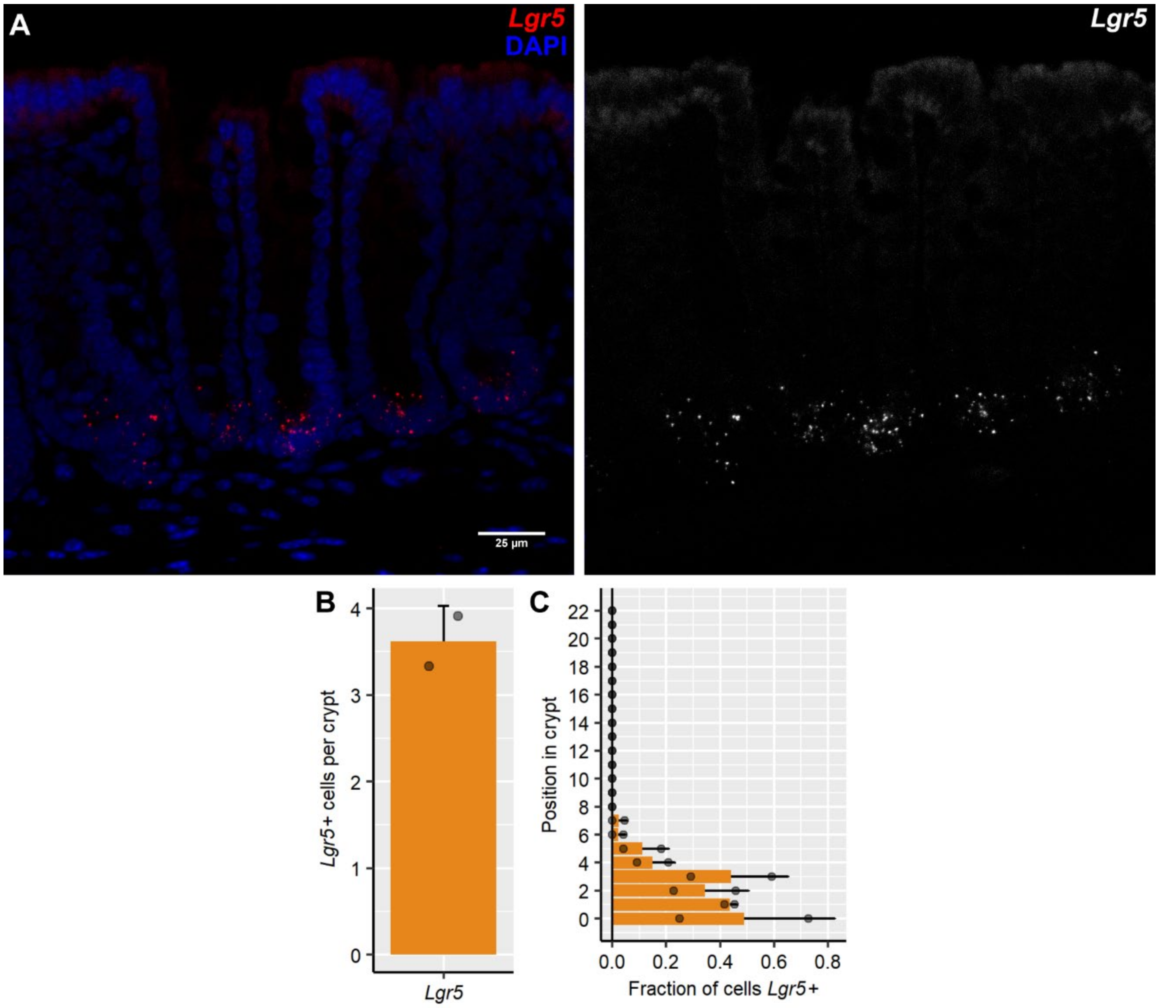

Figure 3.3. Lgr5 characterizes stem cells at the crypt base

A. Fluorescent *in situ* hybridization of *Lgr5* identifies stem cells by clusters of punctae near the crypt base. B. Total *Lgr5*+ cells per crypt. C. The fraction of *Lgr5*+ cells relative to total cells counted per position is given per sample. Barplots and error bars represent overall mean ± sd, with points indicating individual mouse means.

well as having potential antimicrobial activity (Z. Chen et al., 2019). Reg4 expression tends to be concentrated in the apical cytosol of cells that tend to be slightly more bulbous than surrounding cell types (Figure 3.4A), a morphological characteristic shared by most cells in the secretory lineage. Reg4 expression is constrained to the lower half of the crypt, primarily based within the niche and early TA region (Figure 3.4C), extending beyond the stem cell compartment. Reg4 expression is only found within a subset of Reg4-RFP

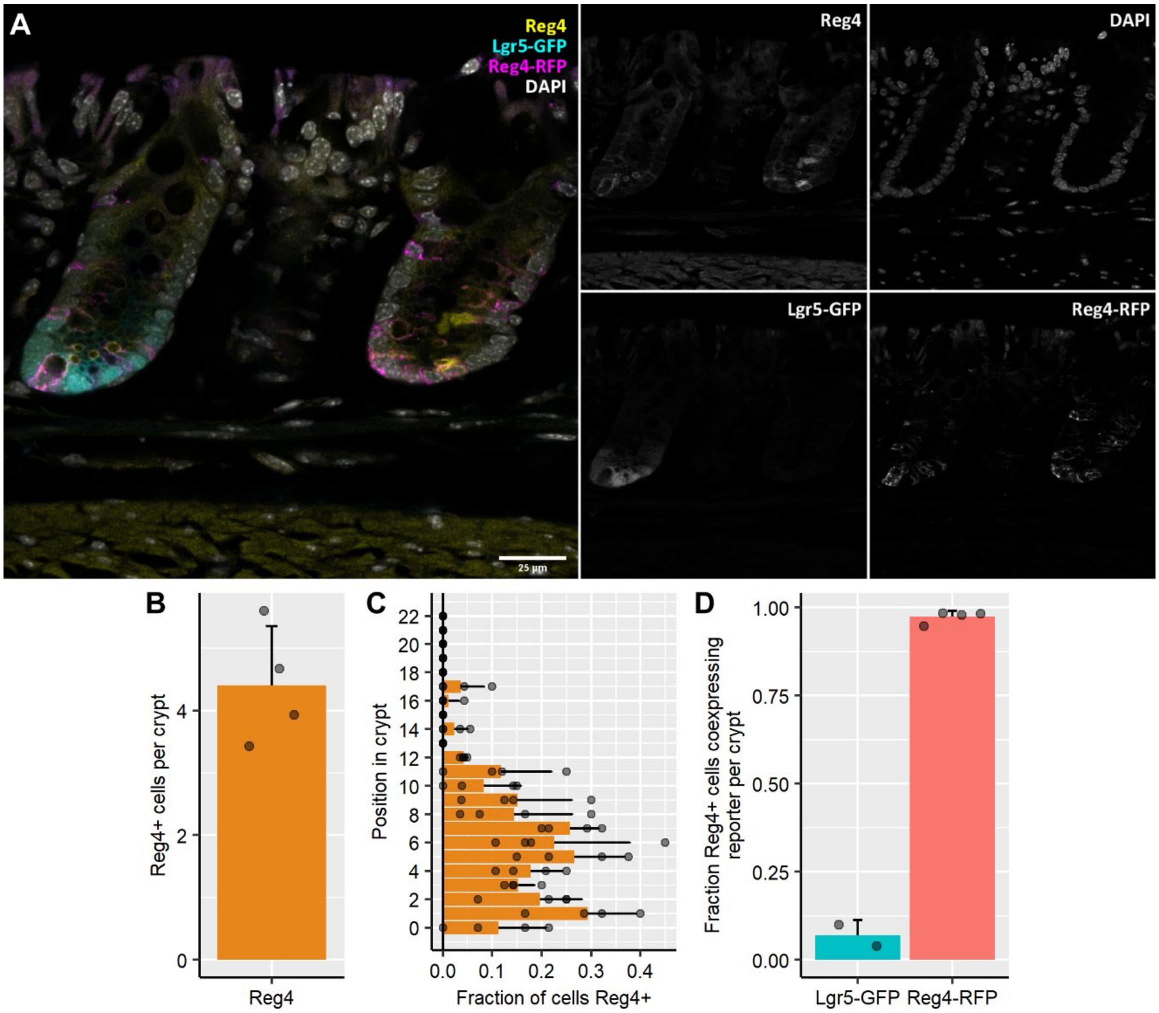

Figure 3.4. Reg4 crypt metrics and coexpression with Reg4 and Lgr5 reporters

A. Immunohistology of Reg4 in the colonic mucosa of an *Lgr5-GFP;Reg4-RFP* reporter mouse, with nuclei indicated by DAPI. B. Total Reg4+ cells per crypt. C. The fraction of Reg4+ cells relative to total cells counted per position is given per sample. D. The fraction of Reg4+ reporter cells is given as a fraction of total Reg4+ cells per sample. Barplots and error bars represent overall mean ± sd, with points indicating individual mouse means.

reporting cells (Figure 3.4D), suggesting that Reg4-expression occurs early in the development of secretory cells and eventually diminishes as they move upward on the crypt axis, with Reg4-RFP perduring through the lifecycle of the secretory cell.

Lrig1 is expressed in the stem and progenitor compartment

Lrig1 is a transmembrane negative regulator of Egfr and ErbB receptors (Powell et al., 2012), and is broadly expressed in stem and progenitor cells within the colonic crypt

(Poulin et al., 2014). This breadth of applicability makes it especially useful in assaying for shifts in the expected proliferative capacity of the niche. In homeostasis, Lrig1 expression is found on the basolateral membranes of expressing cells (Figure 3.5A), with its expression constrained to nearly the entirety of the stem cell niche and lower TA region (Figure 3.5C). As it is broadly expressed in this region, it coexpresses with Lgr5-GFP, and to a lesser extent Reg4-RFP (Figure 3.5D).

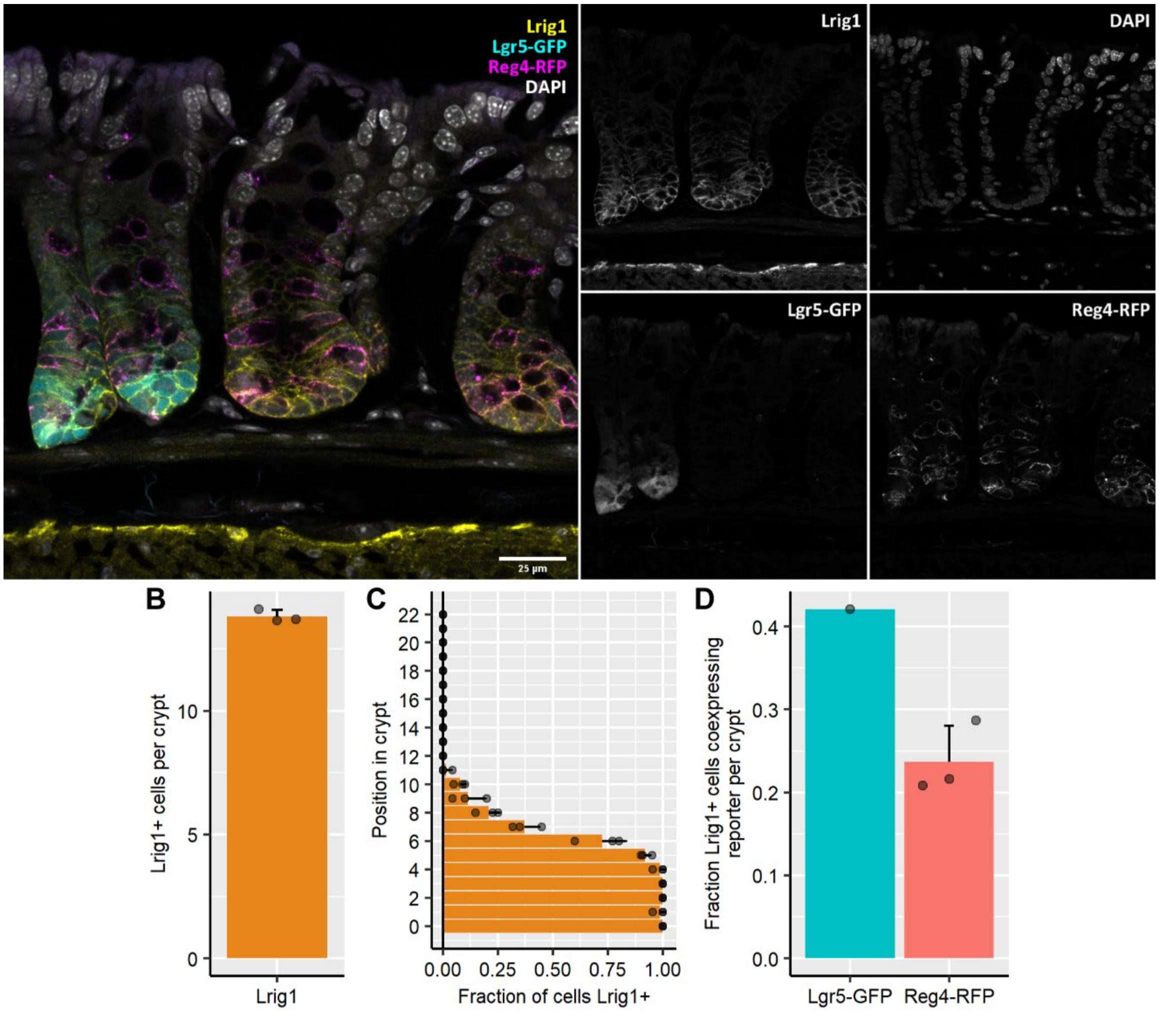

Figure 3.5. Lrig1 crypt metrics and coexpression with Reg4 and Lgr5 reporters

A. Immunohistology of Lrig1 in the colonic mucosa of an *Lgr5-GFP;Reg4-RFP* reporter mouse, with nuclei indicated by DAPI. B. Total Lrig1+ cells per crypt. C. The fraction of Reg4+ cells relative to total cells counted per position is given per sample. D. The fraction of Lrig1+ reporter cells is given as a fraction of total Lrig1+ cells per sample. Barplots and error bars represent overall mean ± sd, with points indicating individual mouse means.

Ki67 is expressed in proliferating cells

Ki67 is a nuclear protein that is expressed throughout mitosis, localizing to the nucleus in actively cycling cells (Figure 3.6A). The level of Ki67 expression varies depending on the phase of the cell cycle, with increased expression during G2 phase and peak expression during mitosis (X. Sun & Kaufman, 2018). In crypt homeostasis, Ki67 is normally expressed within the lower half of the crypt, throughout both niche and TA

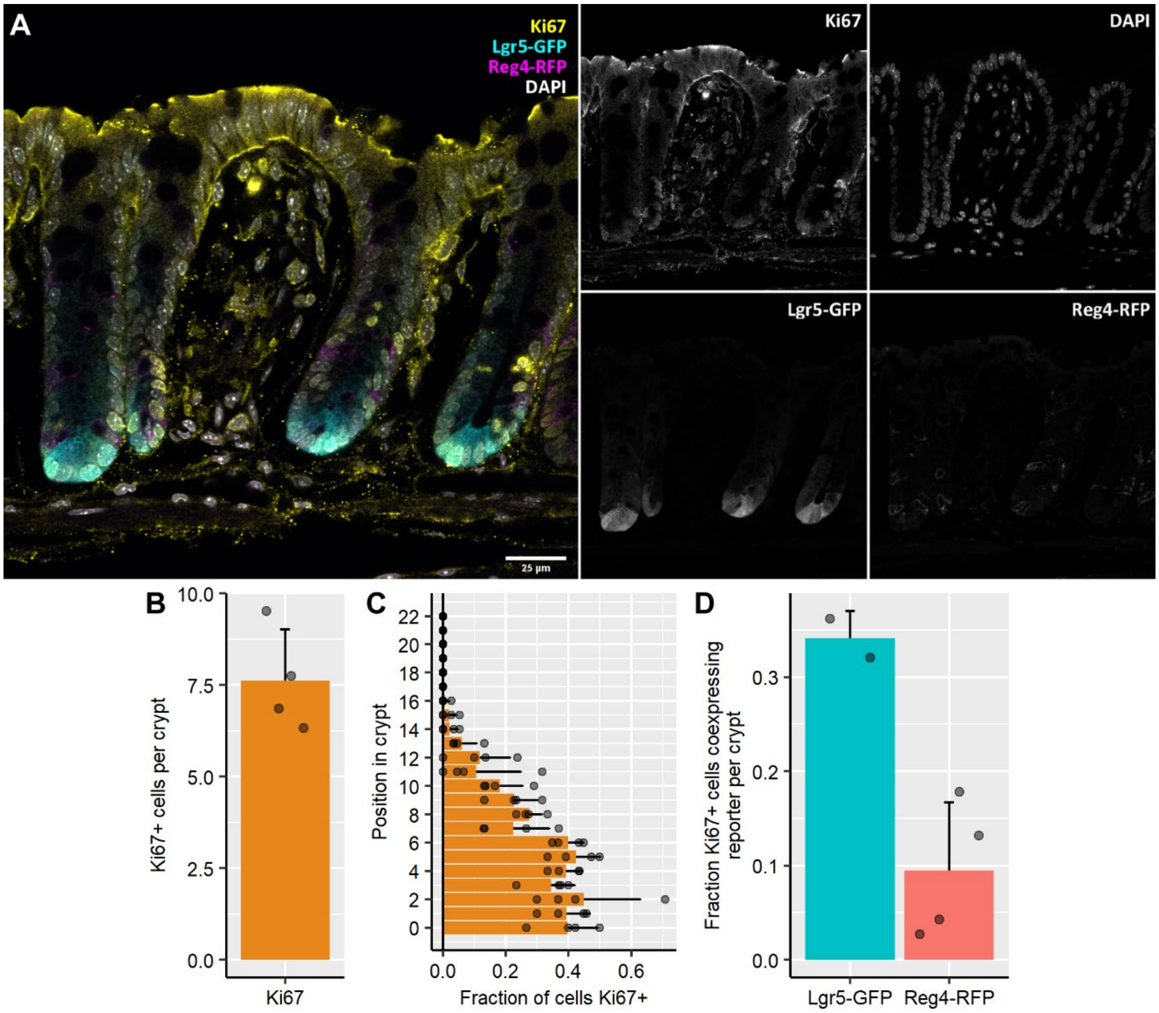

Figure 3.6. Ki67 crypt metrics and coexpression with Reg4 and Lgr5 reporters

A. Immunohistology of Ki67 in the colonic mucosa of an *Lgr5-GFP;Reg4-RFP* reporter mouse, with nuclei indicated by DAPI. B. Total Ki67+ cells per crypt. C. The fraction of Ki67+ cells relative to total cells counted per position is given per sample. D. The fraction of Ki67+ reporter cells is given as a fraction of total Ki67+ cells per sample. Barplots and error bars represent overall mean ± sd, with points indicating individual mouse means.

regions (Figure 3.6C). It is highly coexpressed with Lgr5-GFP+ cells, and lowly coexpressed with Reg4-RFP+ cells, suggesting that Reg4-lineage cells are largely post-mitotic (Figure 3.6D). This is in-line with our current understanding of secretory cell maturation, which suggests that secretory differentiation precludes further proliferation (Pellegrinet et al., 2011; Stamataki et al., 2011).

Histone H3 is phosphorylated in cells undergoing mitosis

Histone H3 is heavily phosphorylated specifically during metaphase of mitosis and meiosis, with rapid global dephosphorylation after its conclusion (Hans & Dimitrov, 2001). This makes phospho-Histone H3 (p-H3) a useful marker for probing cells undergoing mitosis, as it is less generally expressed than Ki67 and has a higher specificity (Figure 3.7A). In corollary, it is less useful for statistical aggregation as p-H3+ events are rarer, with only 1.0 p-H3+ cells per crypt in homeostasis (Figure 3.7B). Similarly to Ki67's distribution, p-H3 is found throughout the niche and TA regions of the crypt (Figure 3.7C), indicating its utility for assaying positionality of proliferation, although experimental power would have to be increased to compensate for the lower detection rate. Approximately one quarter of all p-H3+ cells coexpress with Lgr5-GFP (Figure 3.7D), which comports with the idea that several further divisions occur in the TA region where progenitors fate commit and differentiate. There is a negligible amount of p-H3 coexpression with Reg4-RFP, which corroborates the data from Ki67 indicating that Reg4-lineage cells are largely post-mitotic.

cKit is expressed in cells of the secretory lineage

cKit is a receptor tyrosine kinase found throughout the cell membrane of expressing cells (Figure 3.8A). cKit expression within the colonic epithelium is constrained to cells

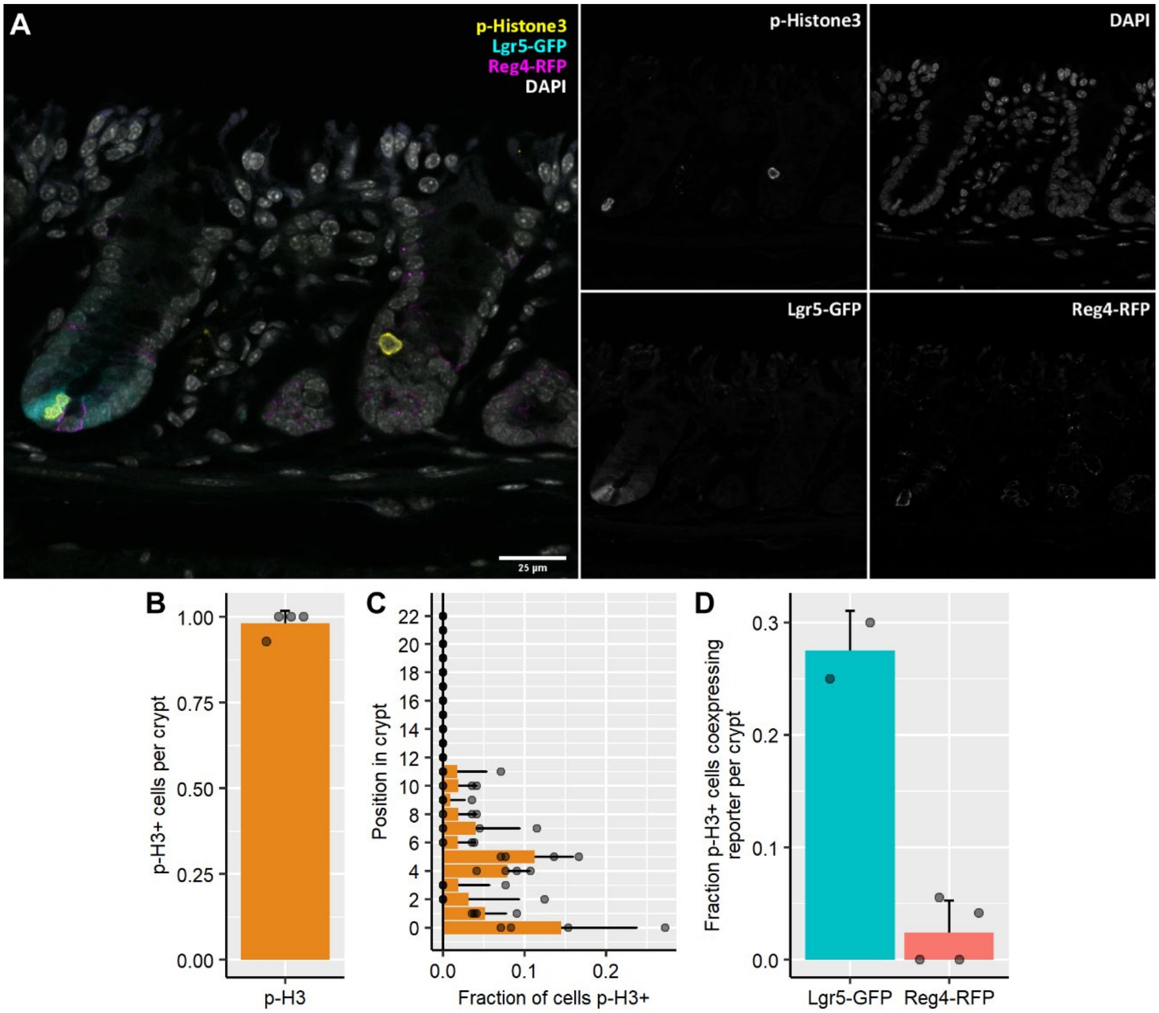

Figure 3.7. Phospho-Histone 3 (p-H3) crypt metrics and coexpression with Reg4 and Lgr5 reporters

A. Immunohistology of p-H3 in the colonic mucosa of an *Lgr5-GFP;Reg4-RFP* reporter mouse, with nuclei indicated by DAPI. B. Total p-H3+ cells per crypt. C. The fraction of p-H3+ cells relative to total cells counted per position is given per sample. D. The fraction of p-H3+ reporter cells is given as a fraction of total p-H3+ cells per sample. Barplots and error bars represent overall mean ± sd, with points indicating individual mouse means.

in the secretory lineage, and acts as a marker of supporting secretory cells in the early-to-midcrypt range of secretory cell development (Rothenberg et al., 2012). cKit can be detected in secretory cells from the crypt base to the upper regions of the crypt (Figure 3.8C), which makes it useful as a marker for cells in the secretory lineage that is compatible with fixed frozen tissue histology. This contrasts with the classical pan-secretory/goblet cell

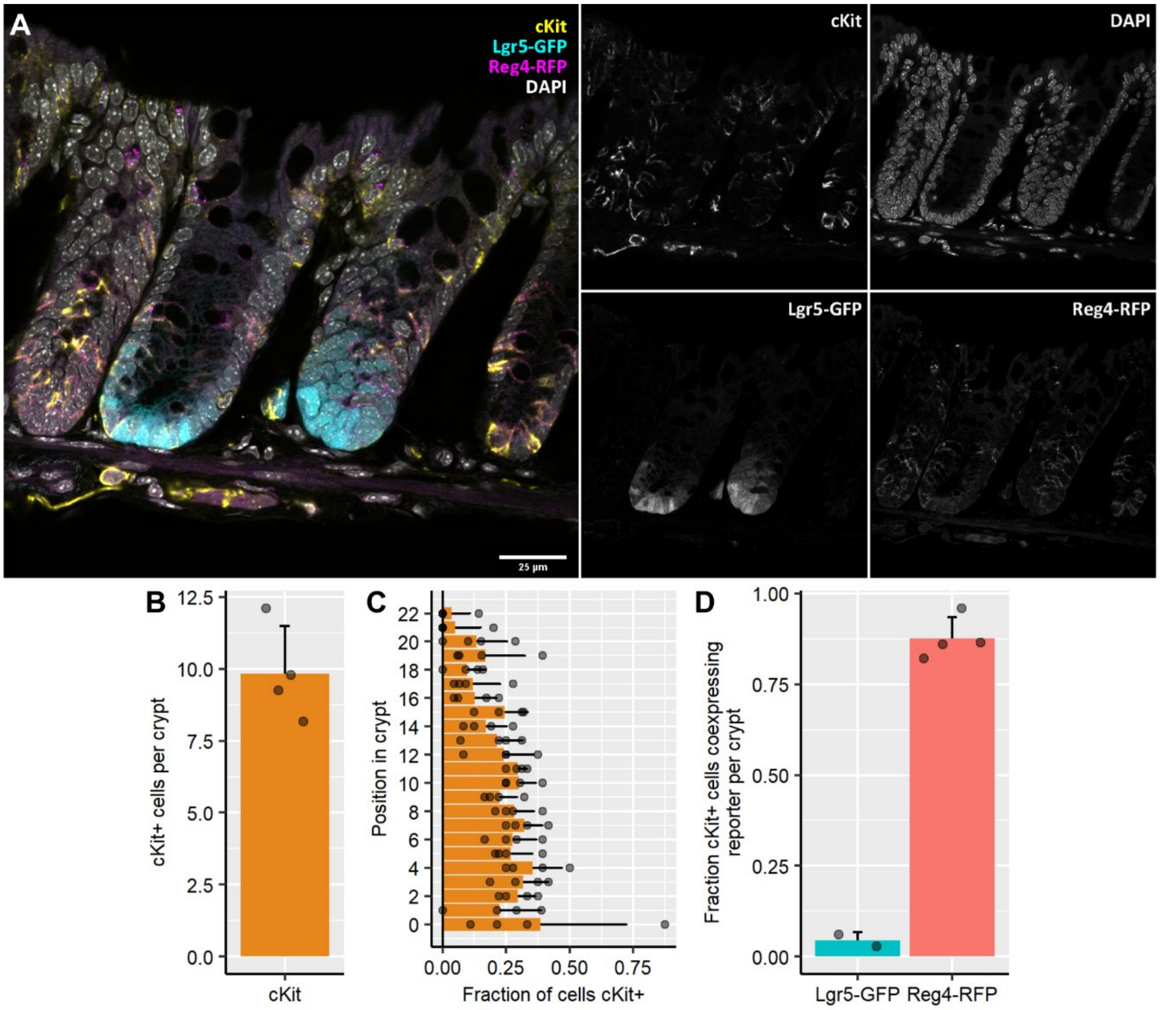

Figure 3.8. cKit crypt metrics and coexpression with Reg4 and Lgr5 reporters

A. Immunohistology of cKit in the colonic mucosa of an *Lgr5-GFP;Reg4-RFP* reporter mouse, with nuclei indicated by DAPI. B. Total cKit+ cells per crypt. C. The fraction of cKit+ cells relative to total cells counted per position is given per sample. D. The fraction of cKit+ reporter cells is given as a fraction of total cKit+ cells per sample. Barplots and error bars represent overall mean ± sd, with points indicating individual mouse means.

marker Muc2; currently available antibodies requires antigen retrieval which can damage other antigens and endogenous fluorophores, reducing the staining cross compatibility (Ramos-Vara & Miller, 2014).

Chromogranin A characterizes enteroendocrine cells

Enteroendocrine cells are a specialized class of several specific cell types that are all marked by expression of Chromogranin A (ChgA), a secretory protein associated with vesicular storage and release of hormone and neuropeptide payloads into the mucosa based on sensing of the environment through luminal chemosensation (Rindi et al., 2004; Yu et al., 2020). This functionality leads to a distinctive cell shape with a small chemosensory surface on the luminal side, and bulbous cell body marked by intense ChgA staining in the basolateral cytoplasm (Figure 3.9A). The enteroendocrine cell population helps to

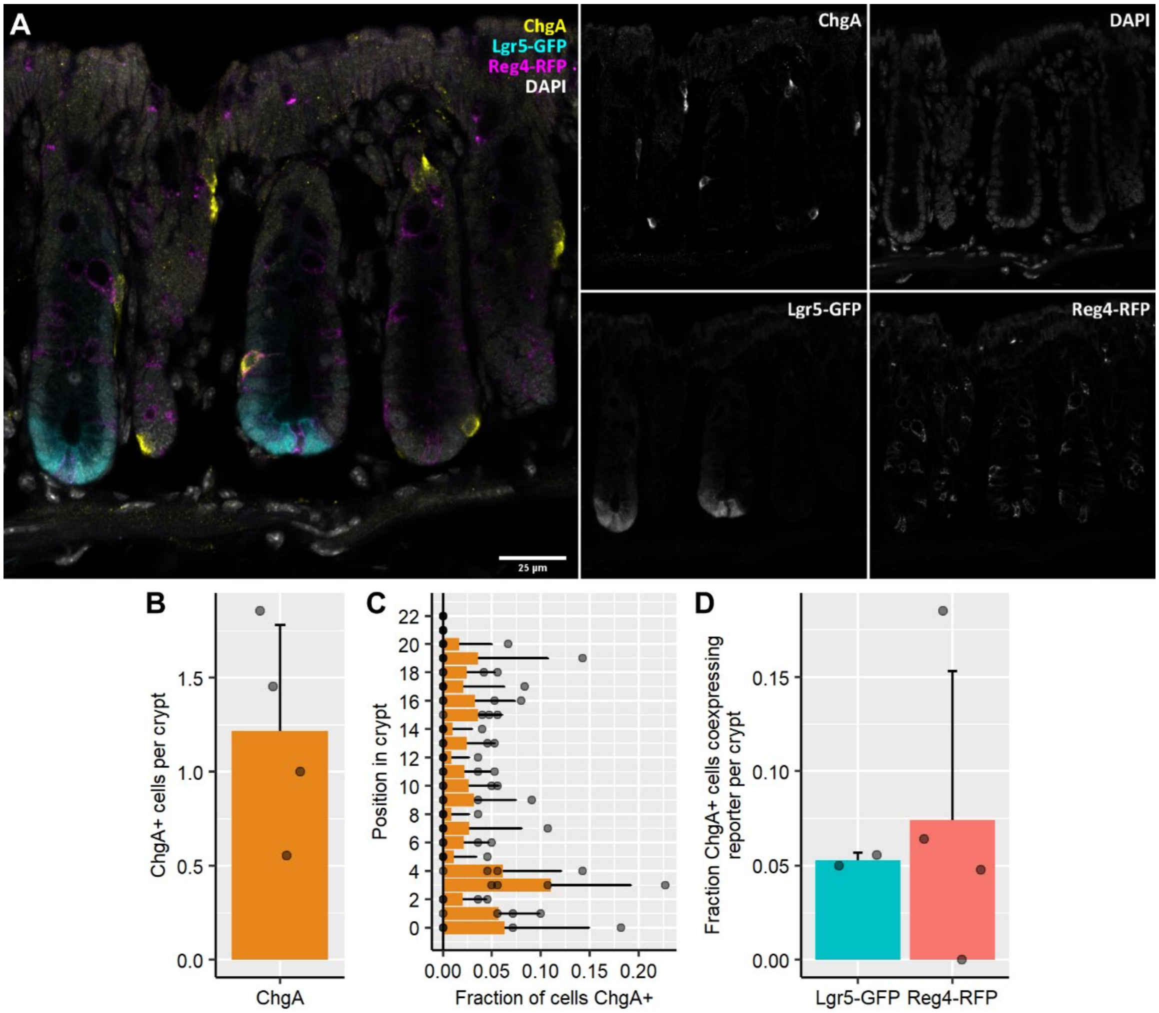

Figure 3.9. Enteroendocrine marker Chromogranin A (ChgA) crypt metrics and coexpression with Reg4 and Lgr5 reporters

A. Immunohistology of ChgA in the colonic mucosa of an *Lgr5-GFP;Reg4-RFP* reporter mouse, with nuclei indicated by DAPI. B. Total ChgA+ cells per crypt. C. The fraction of ChgA+ cells relative to total cells counted per position is given per sample. D. The fraction of ChgA+ reporter cells is given as a fraction of total ChgA+ cells per sample. Barplots and error bars represent overall mean ± sd, with points indicating individual mouse means.

maintain crypt homeostasis and secretory/absorptive cell population balancing (Mellitzer et al., 2010). Despite their essential role to the rest of the epithelium, they represent a sparse component of crypts, only comprising an average of 1.2 cells per crypt cross-section, which represents less than 3% of total crypt cells (Figure 3.9B). There is no apparent bias toward co-reporting with either Lgr5-GFP or Reg4-RFP (Figure 3.9D), the latter of which suggests that enteroendocrine cell development is distinctly separate from the major secretory cell maturation pathway. There is also no obvious bias in the position of enteroendocrine cells, suggesting that they are not directed to migrate or retain position in any given compartment (Figure 3.9C). This comes with a caveat that this data is underpowered given the sparsity of this cell type.

Dcamkl1 is expressed in tuft cells

Tuft cells are chemosensory epithelial cells that play roles in immunosensing and communication with the peripheral nervous system (Gerbe et al., 2012; O'Leary et al., 2019). These cells are marked by expression of Dcamkl1, a protein kinase associated with neuronal migration and transport that can be observed throughout the cytoplasm (Figure 3.10A). This marker also stains neural cells, which are visible in the mesenchyme between crypts. Tuft cells make up a small fraction of total crypt cells (Figure 3.10B) and have no indication of co-staining with Reg4-RFP (Figure 3.10D), indicating a cell lineage entirely independent of Reg4-associated secretory cell maturation. Tuft cells have no apparent specificity to any crypt region (Figure 3.10C), although the sparse data I present may not capture the true distribution of this cell type.

Increased villin expression characterizes colonocyte maturation

Villin is a cytoskeletal protein that acts to enhance branching of actin filaments,

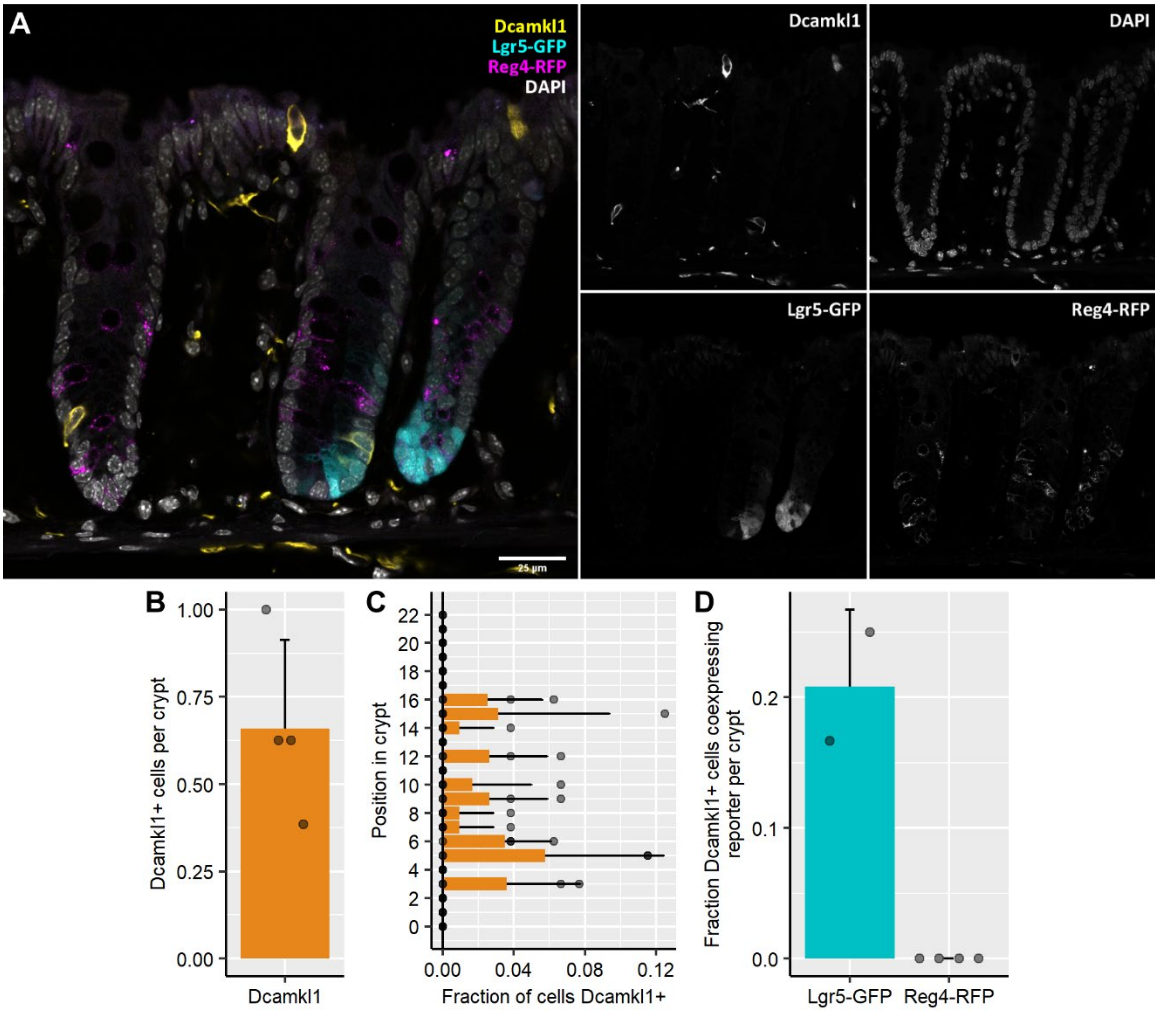

Figure 3.10. Tuft cell marker Dcamkl1 crypt metrics and coexpression with Reg4 and Lgr5 reporters

A. Immunohistology of Dcamkl1 in the colonic mucosa of an *Lgr5-GFP;Reg4-RFP* reporter mouse, with nuclei indicated by DAPI. B. Total Dcamkl1+ cells per crypt. C. The fraction of Dcamkl1+ cells relative to total cells counted per position is given per sample. D. The fraction of Dcamkl1+ reporter cells is given as a fraction of total Dcamkl1+ cells per sample. Barplots and error bars represent overall mean ± sd, with points indicating individual mouse means.

which gives rise to microvilli on the apical surface of columnar epithelia (West et al., 1988). All epithelial cells in the small intestine and colon express villin (Madison et al., 2002), although differentiated cells express it at an order of magnitude more than niche and differentiating cells (Figure 3.11A). This is supported by the lack of coexpression of cells co-expressing villin and Lgr5-GFP (Figure 3.11D). In contrast, Reg4-RFP+ cells harbor

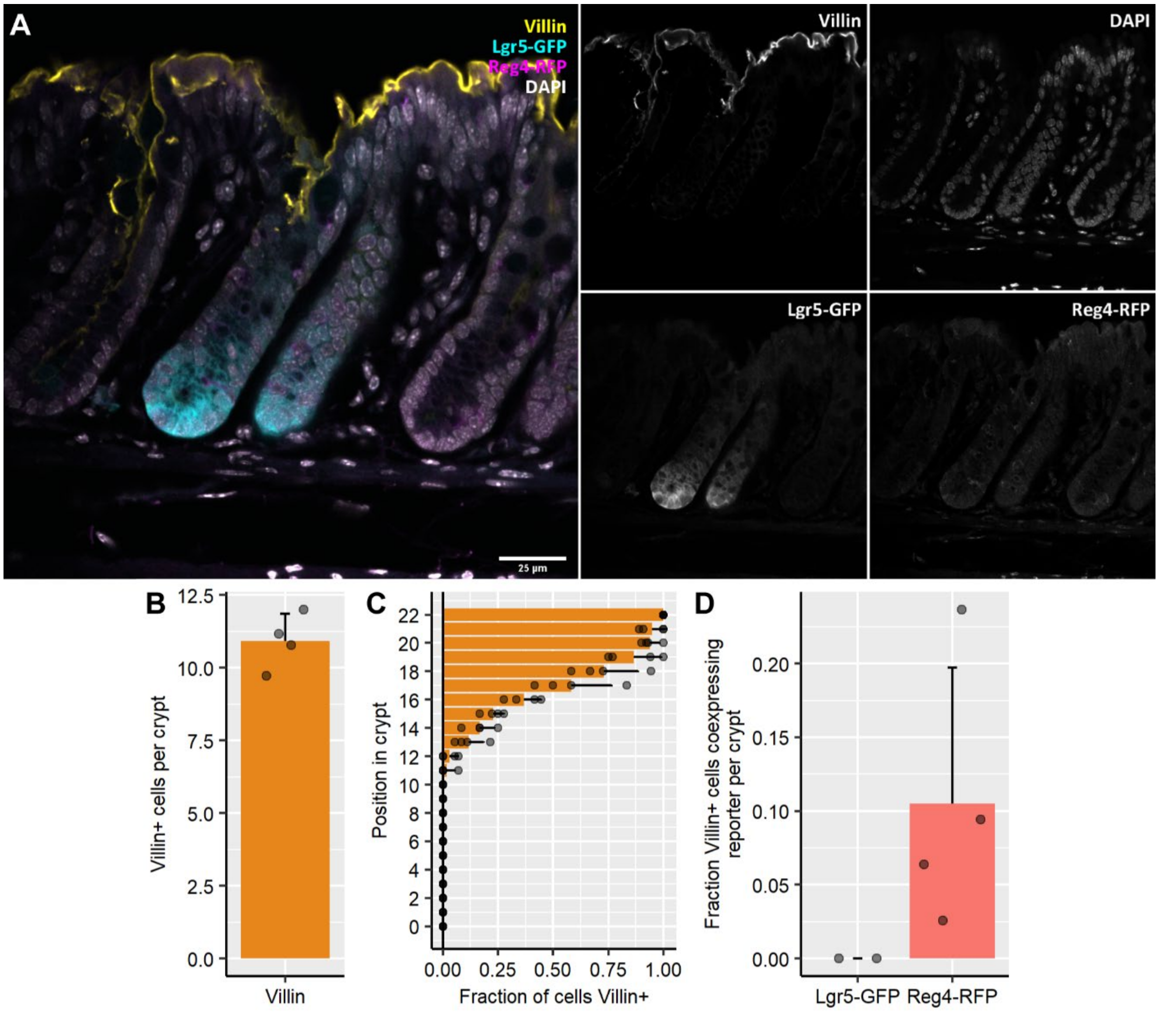

Figure 3.11. Villin is strongly expressed in mature colonocytes

A. Immunohistology of villin in the colonic mucosa of an *Lgr5-GFP;Reg4-RFP* reporter mouse, with nuclei indicated by DAPI. B. Total villin-high cells per crypt. C. The fraction of villin-high reporter cells is given as a fraction of total villin-high cells per sample. D. The fraction of villin-high cells relative to total cells counted per position is given per sample. Barplots and error bars represent overall mean ± sd, with points indicating individual mouse means.

high villin expression; demostrating the extent to which this reporter perdures to the top of the crypt axis, and the designation of the secretory cell type. While it is difficult to determine which specific cells harbor the lowest and highest villin expression, aggregating the statistics from manually determined thresholds for many crypts yield a curve suggesting an average crypt start position of 16-17 (from position zero in the base of the crypt) for “high villin” expression (Figure 3.11C).

Notch signaling and ligand expression

The Notch cell signaling pathway is the primary pathway determining secretory and absorptive lineages within the crypt, and is required for stem cell maintenance. This signaling pathway is modulated through juxtacrine signaling, requiring direct cell-cell contact between a Notch ligand-presenting cell and a receiving cell with activated Notch. Notch is activated by binding to one of these ligands, after which an ADAM protease cleaves the extracellular domain, allowing the transmembrane and intracellular domain to evert into the cell, whereupon gamma secretase cleaves the intracellular domain (NICD) which is trafficked to the nucleus to activate expression of downstream genes (Bray, 2016). A key component of this expression is a binary genetic circuit that begins with Atoh1 expression, causing downregulation of Notch receptor and upregulation of Notch ligands. Subsequent activation of Notch in adjacent cells causes expression of Hes1, a repressor of Atoh1. In the colonic epithelium, Hes1 activation is associated with stemness and absorptive lineages, while Atoh1 expression is associated with secretory lineages (Lo et al., 2017; Noah & Shroyer, 2013; VanDussen et al., 2012). Within the colonic epithelium, cleaved Notch1 can be observed most strongly in the cytosol bordering the basolateral membrane, with occasional punctate detection in nuclei (Figure 3.12A). These signals are most frequently detected within the stem cell and early TA compartments, corroborating its role in stem and progenitor cell maintenance (Figure 3.12C). While cleaved Notch1 has moderate co-expression with Lgr5-GFP, it rarely co-reports with Reg4-RFP, corroborating the idea that Reg4-lineage cells are associated with corollary ligands of the Notch pathway (Figure 3.12D).

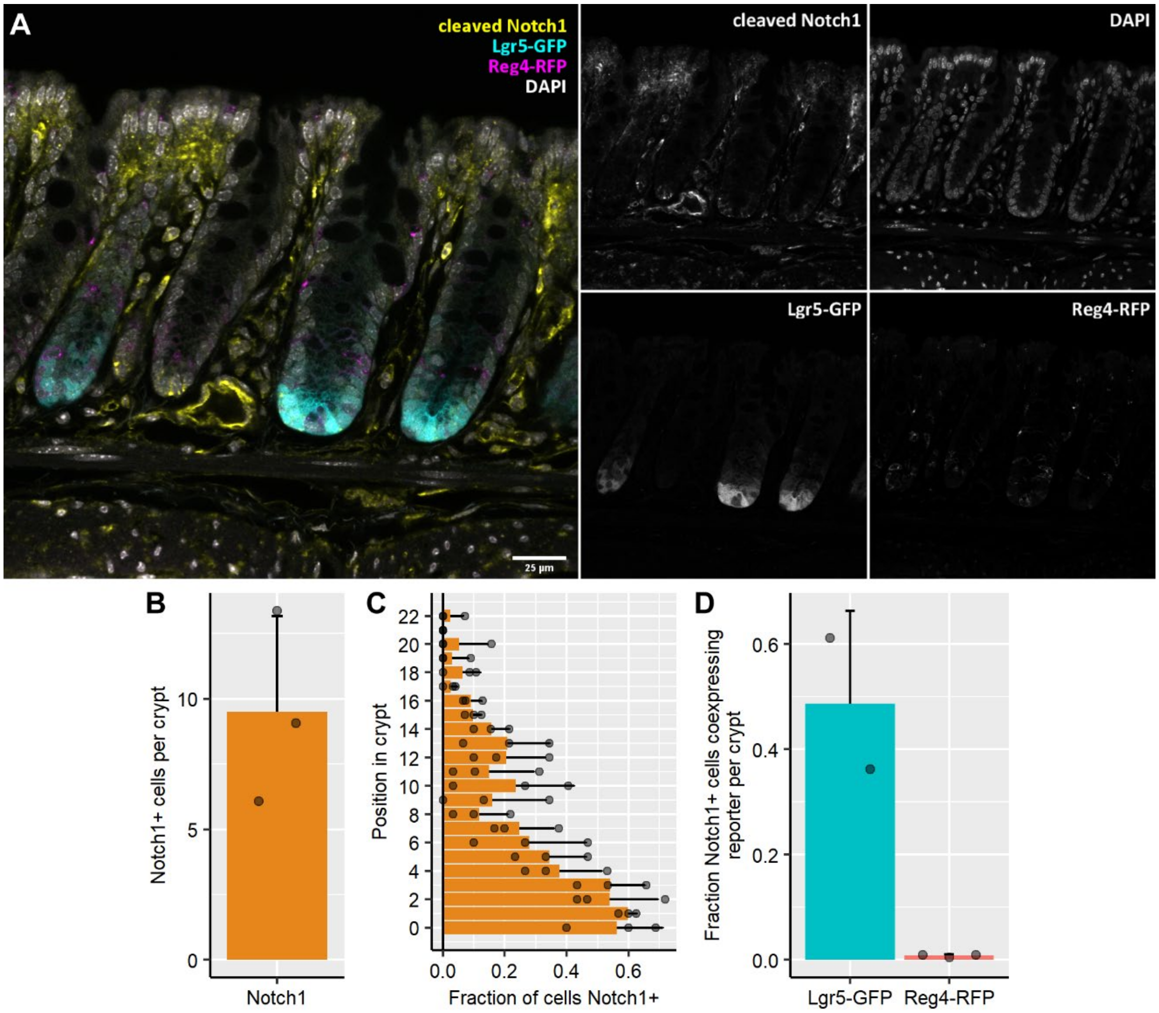

Figure 3.12. Cleaved Notch1 crypt metrics and coexpression with Reg4 and Lgr5 reporters

A. Immunohistology of cleaved Notch in the colonic mucosa of an *Lgr5-GFP;Reg4-RFP* reporter mouse, with nuclei indicated by DAPI. B. Total NTM+ cells per crypt. C. The fraction of Notch1+ cells relative to total cells counted per position is given per sample. D. The fraction of Notch1+ reporter cells is given as a fraction of total NTM+ cells per sample. Barplots and error bars represent overall mean ± sd, with points indicating individual mouse means.

The two classical Notch ligands present within the colonic epithelium are Dll1 and Dll4, which are expressed by subpopulations of secretory cells, while Notch1 is the primary Notch receptor (Pellegrinet et al., 2011; Rothenberg et al., 2012; Shimizu et al., 2014). Both ligands have transmembrane domains, indicated by their presence on cell membranes. Dll1 tends to localize most strongly to the basal membrane (Figure 3.13A), while Dll4 is broadly localized to the basolateral membrane in expressing cells (Figure 3.13B). Despite their functional redundancy, Dll1 and Dll4 are differentially expressed within the crypt, with Dll4-expressing cells having 1.3 times the prevalence of Dll1-expressing cells (Figure 3.13C). Dll4 is homogenously expressed across the crypt axis (Figure 3.13E), although Dll1's peak expression region is in the early TA region (Figure 3.13D). Since progenitors proliferate and begin to adopt the in this region, this suggests that Dll1 may play a heretofore unknown role in fate specification over the more ubiquitously expressed Dll4. As many types of colonic epithelial cells have various degrees of cell identity fluidity, this disparity may play a role in specifying aspects of that property of differentiation, modulating subtypes of cells that are more poorly classified at present. Both Dll1 and Dll4 highly co-report with Reg4-RFP, indicating that most Notch signaling is largely mediated through cells in the Reg4-lineage (Figure 3.13F).

The Eph/Ephrin axis is an essential component of crypt axis specification

The Eph family of proteins are receptor tyrosine kinases (RTKs) which are activated by dimerization through binding with their ligand, ephrins. Both of these protein families are transmembrane proteins, and are a notable subclass of RTKs as they require direct contact between receptor- and ligand-expressing cells. This also allows for reverse

---

Figure 3.13. Notch ligands Dll1 and Dll4 crypt metrics and coexpression with Reg4 and Lgr5 reporters

A. Immunohistology of Dll1 in the colonic mucosa of an *Lgr5-GFP;Reg4-RFP* reporter mouse, with nuclei indicated by DAPI. B. Immunohistology of Dll4 in the colonic mucosa of an *Lgr5-GFP;Reg4-RFP* reporter mouse, with nuclei indicated by DAPI. C. Total Dll1+ and Dll4+ cells per crypt. D. The fraction of Dll1+ cells relative to total cells counted per position is given per sample. E. The fraction of Dll4+ cells relative to total cells counted per position is given per sample. F. The fraction of co-reporting cells is given as a fraction of total Dll1+ or Dll4+ cells per sample. Barplots and error bars represent overall mean ± sd, with points indicating individual mouse means.

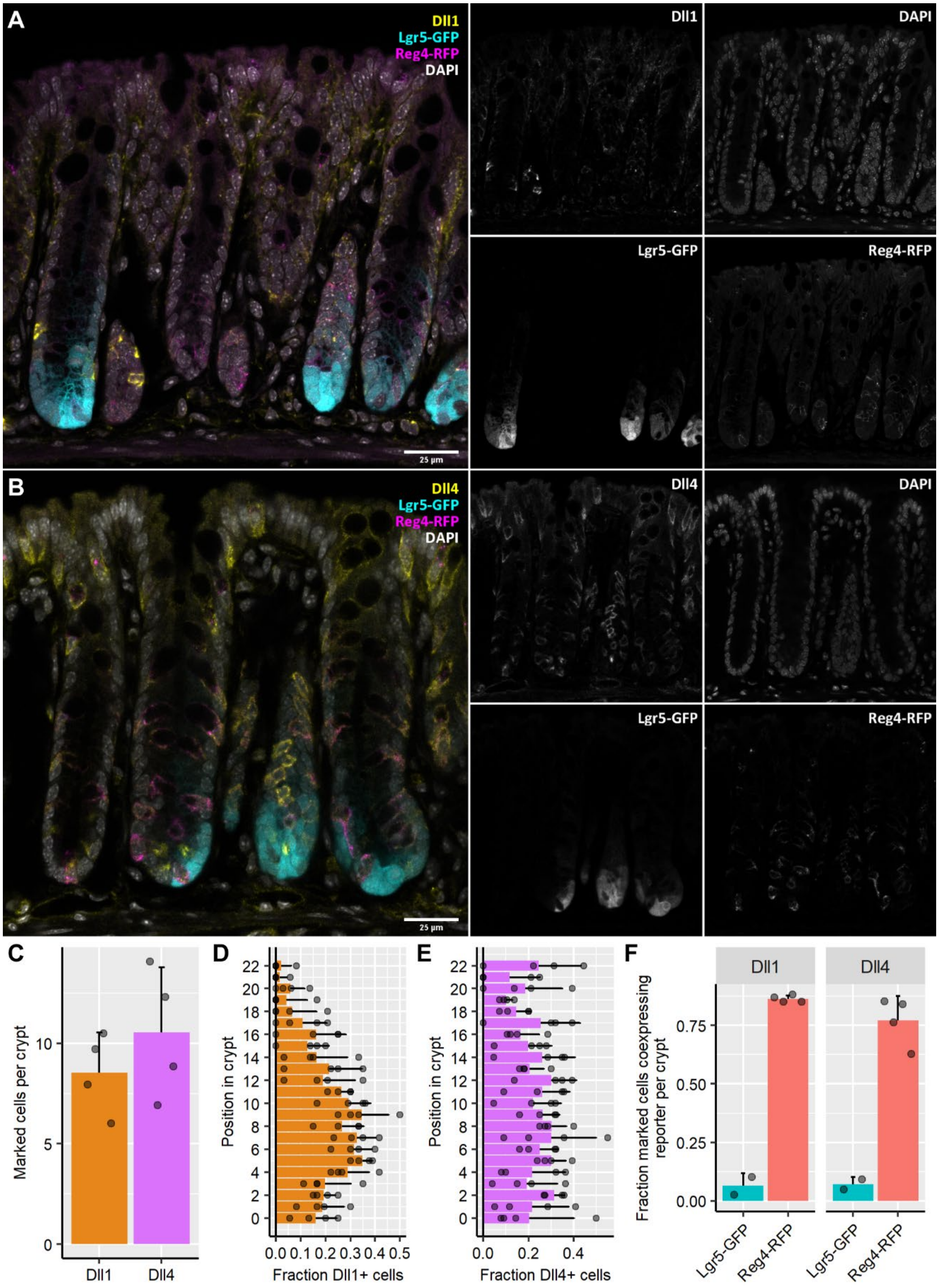
A
Dll1
Lgr5-GFP
Reg4-RFP
DAPI
25 µm
Dll1
DAPI
Lgr5-GFP
Reg4-RFP
B
Dll4
Lgr5-GFP
Reg4-RFP
DAPI
25 µm
Dll4
DAPI
Lgr5-GFP
Reg4-RFP
C
Marked cells per crypt
0
5
10
Dll1
Dll4
D
Position in crypt
0
2
4
6
8
10
12
14
16
18
20
22
Fraction Dll1+ cells
0.0 0.1 0.2 0.3 0.4 0.5
E
Position in crypt
0
2
4
6
8
10
12
14
16
18
20
22
Fraction Dll4+ cells
0.0 0.2 0.4
F
Fraction marked cells coexpressing reporter per crypt
0.00
0.25
0.50
0.75
Dll1
Dll4
Lgr5-GFP
Reg4-RFP
Lgr5-GFP
Reg4-RFP

RTK signaling to the ephrin-expressing cell (Perez White & Getsios, 2014). The primary Eph-associated proteins expressed in the colonic epithelium are EphB2, EphB3, and ephrin-B1. EphB signaling is associated with cell proliferation and migration in the colon, which indicates that this forms an essential component of crypt axis maintenance. I characterized EphB3 and ephrin-B1 expression as representative of the Eph-ephrin axis within the colonic epithelium. EphB3 expression is sharply situated at the base of crypts (Figure 3.14A,C), while ephrin-B1 starts to be strongly expressed after the mid-to-late TA region (Figure 3.14B,D), juxtaposing the polarized expression of these complementary proteins.

Integrin binding mediates basal adhesion and signaling

β4 integrin (Itgb4) is the β-subunit of the heterodimeric integrin α6β4, a basolaterally expressed laminin receptor which acts as a major component of epithelial-matrix interactions. Itgb4 heterodimerizes specifically with the α6 subunit, so it is used as proxy for the fully dimeric form. Itgb4 binds to matrix while transmitting binding signal to the expressing cell through the formation of hemidesmosomes, structural anchors that hold cells together with matrix or other cells (te Molder et al., 2021). Experimentally, the antibody for this protein acts as a powerful stain to delineate crypts from the rest of the

---

Figure 3.14. EphB3/ephrin-B1 axis in the colonic epithelium

A. Immunohistology of EphB3 in the colonic mucosa of an *Lgr5-GFP;Reg4-RFP* reporter mouse, with nuclei indicated by DAPI. B. Immunohistology of ephrin-B1 in the colonic mucosa of an Lgr5-GFP;Reg4-RFP reporter mouse, with nuclei indicated by DAPI. C. The fraction of EphB3+ cells relative to total cells counted per position is given per sample. D. The fraction of ephrin-B1+ cells relative to total cells counted per position is given per sample. Barplots and error bars represent overall mean ± sd, with points indicating individual mouse means.

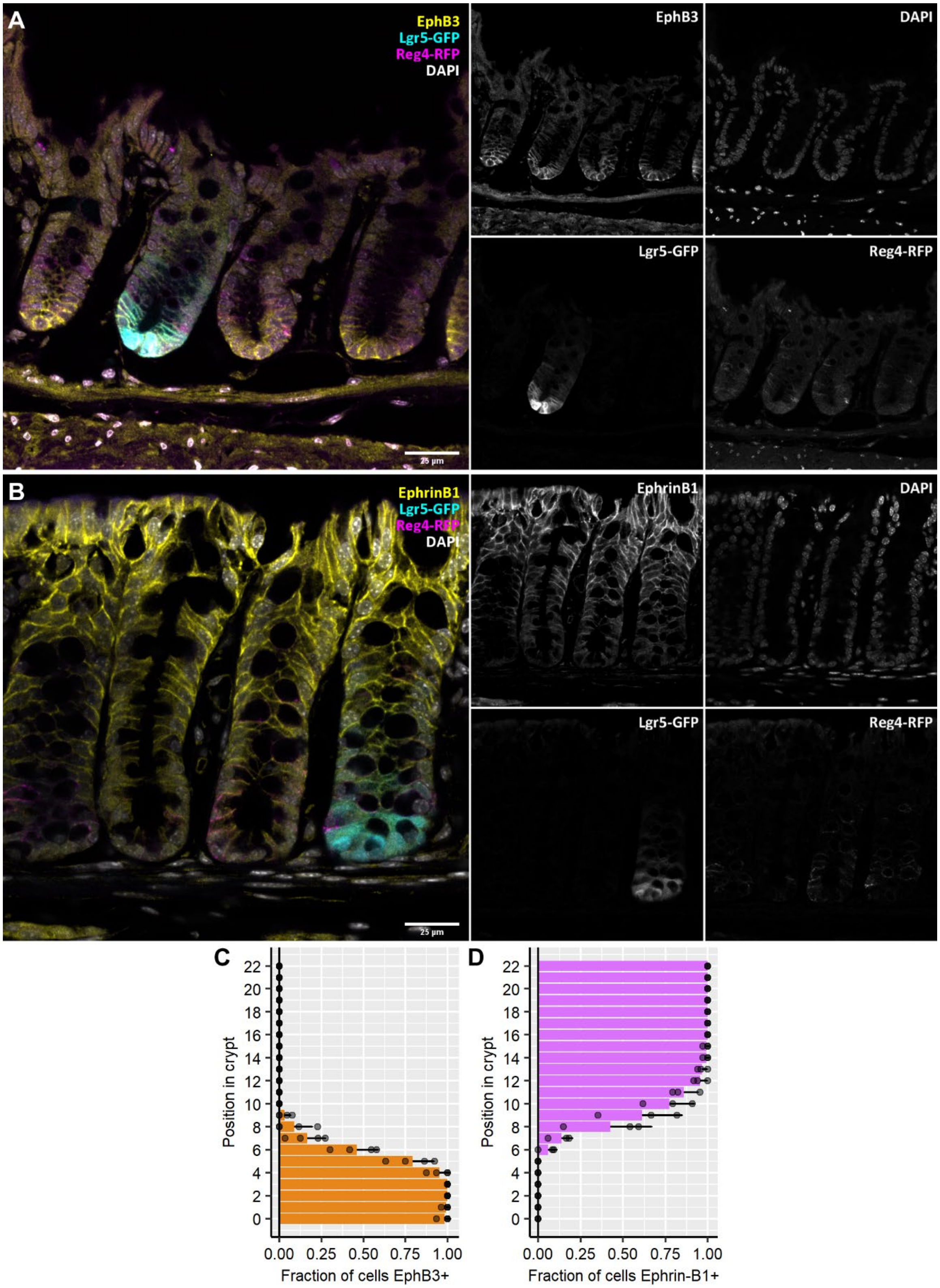
A
EphB3
Lgr5-GFP
Reg4-RFP
DAPI
25 µm
EphB3
DAPI
Lgr5-GFP
Reg4-RFP
B
EphrinB1
Lgr5-GFP
Reg4-RFP
DAPI
25 µm
EphrinB1
DAPI
Lgr5-GFP
Reg4-RFP
C
Position in crypt
0
2
4
6
8
10
12
14
16
18
20
22
0.00
0.25
0.50
0.75
1.00
Fraction of cells EphB3+
D
Position in crypt
0
2
4
6
8
10
12
14
16
18
20
22
0.00
0.25
0.50
0.75
1.00
Fraction of cells Ephrin-B1+

mucosa, as Itgb4 labels strongly and sharply to the basal edge of the epithelium (Figure 3.15). No statistics are presented in this data due to its largely ubiquitous nature in homeostasis. However, research suggests that Itgb4 may be differentially regulated in crypt-disruptive events such as fissioning, where a new crypt forms by either bifurcating or budding from an existing crypt (Langlands et al., 2016). As such, this marker may be useful for characterizing abnormalities in this process or other similar events governing crypt morphology.

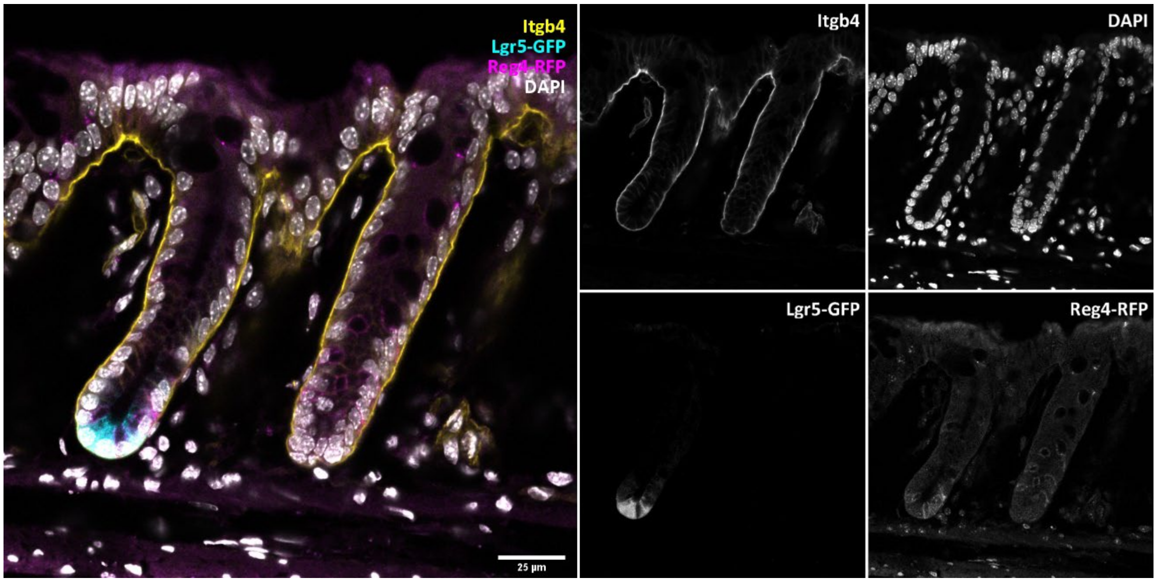

Figure 3.15. Beta-4 integrin (Itgb4) characterizes the basal interface of the colonic epithelium

Immunohistology of Itgb4 in the colonic mucosa of an *Lgr5-GFP;Reg4-RFP* reporter mouse, with nuclei indicated by DAPI.

Anoikis extrudes cells from the epithelium via a Caspase cascade

Cell death in the colonic epithelium is typically conducted through a process known as anoikis, a form of apoptosis in which a cell loses extracellular matrix contact to be sloughed into the lumen (Taddei et al., 2012). As with other forms of apoptosis, anoikis is characterized by a Caspase cascade, in which a series of caspase proteins are activated through proteolytic cleavage which represents a point of no return (Brentnall et al., 2013).

As such, detection of cleaved caspases can be used as an indicator of initiated apoptosis, as shown by cleaved Caspase 3 (c-Cas3) (Figure 3.16A). As this process rapidly causes cell blebbing and dissociation, marked cells often bear little resemblance to columnar epithelial cells. In homeostasis, anoikis is typically only rarely observed, with c-Cas3 only detectable in the uppermost luminal epithelium (Figure 3.16C).

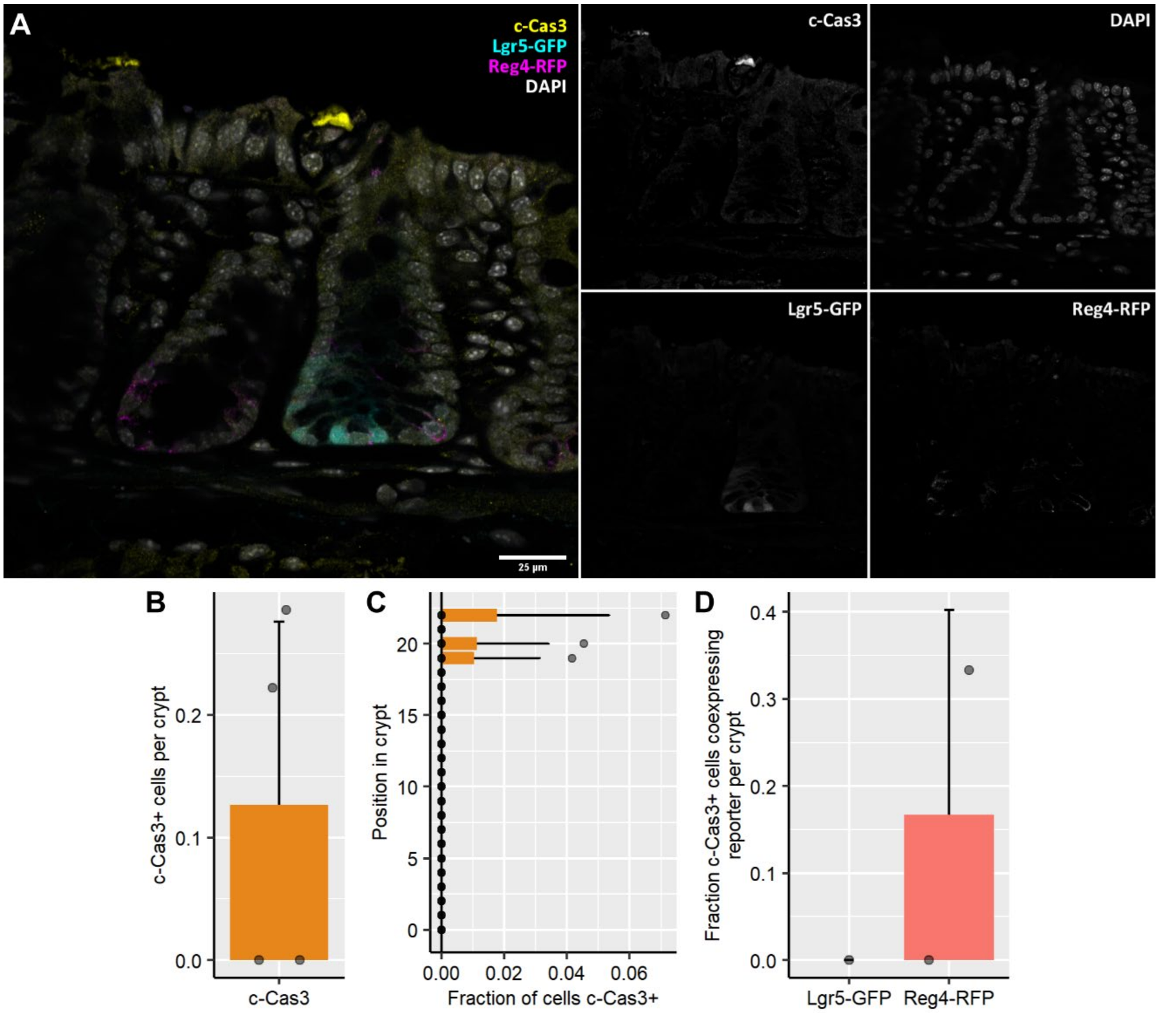

Figure 3.16. Cleaved Caspase 3 (c-Cas3) axis in the colonic epithelium

A. Immunohistology of c-Cas3 in the colonic mucosa of an *Lgr5-GFP;Reg4-RFP* reporter mouse, with nuclei indicated by DAPI. B. Total c-Cas3+ cells per crypt. C. The fraction of c-Cas3+ reporter cells is given as a fraction of total c-Cas3+ cells per sample. D. The fraction of c-Cas3+ cells relative to total cells counted per position is given per sample. Barplots and error bars represent overall mean ± sd, with points indicating individual mouse means.

Materials and Methods

Table 3.1. Key Resources

Designation	Source or reference	Identifiers	Additional information
Genetic reagents (*Mus musculus*)			
$Lgr5^{tm1(cre/ERT2)Cle}$/J, $Lgr5^{EGFP\text{-}IRES\text{-}creERT2}$	The Jackson Laboratory	Cat# JAX: 008875, RRID:IMSR_JAX:008875	
$Reg4^{tm1(HBEGF/DsRed)Cle}$/J, $Reg4^{DTR\text{-}Red}$	The Jackson Laboratory	Cat# JAX: 029705, RRID:IMSR_JAX:029705	
Antibodies			
Goat polyclonal anti-Reg4	R&D Systems	Cat# AF1379	IHC-F (1:100)*
Rabbit monoclonal anti-p-Histone 3	Cell Signaling Technology	Cat# 3377	IHC-F (1:250)*
Goat polyclonal anti-Ephrin-B1	R&D Systems	Cat# AF473	IHC-F (1:100)*
Goat polyclonal anti-EphB3	R&D Systems	Cat# AF432	IHC-F (1:400)*
Rabbit monoclonal anti-Villin	Abcam	Cat# ab130751	IHC-F (1:500)*
Rabbit polyclonal anti-Dcamkl1	Abcam	Cat# ab31704	IHC-F (1:1000)*
Rabbit polyclonal anti-ChgA	Abd Serotech	Cat# MCA845	IHC-F (1:500)*
Rabbit polyclonal anti-cleaved Cas3	Bioss	Cat# bs-0081R	IHC-F (1:200)*
Rat monoclonal anti-Itgb4	abcam	Cat# ab25254	IHC-F (1:500)*
Goat polyclonal anti-cKit	R&D Systems	Cat# AF1356	IHC-F (1:500)*
Rat monoclonal anti-Ki67	Thermo Fisher Scientific	Cat# 14-5698-82, RRID:AB_10854564	IHC-F (1:100)*
Goat polyclonal anti-Lrig1	R&D Systems	Cat# AF3688, RRID:AB_2138836	IHC-F (1:500)*
Rabbit monoclonal anti-Notch1	Cell Signaling Technology	Cat# 3608, RRID:AB_2153354	IHC-F (1:400)*
Sheep polyclonal anti-Dll1	R&D Systems	Cat# AF5026, RRID:AB_2092830	IHC-F (1:250)*
Goat polyclonal anti-Dll4	R&D Systems	Cat# AF1389, RRID:AB_354770	IHC-F (1:400)†
Sequence-based reagents			
RNAscope® Probe-Mm-Lgr5	Advanced Cell Diagnostics	Cat# 312171	
Commercial assays and kits			
RNAscope® Multiplex Fluorescent Reagent Kit v2	Advanced Cell Diagnostics	Cat# 323100	

Table 3.1 (Continued)

Designation	Source or reference	Identifiers	Additional information
Chemical compounds and drugs			
Blocking Buffer, 5% Bovine Serum Albumen, 0.3% Triton X-100, 1mM CaCl2 in Phosphate-Buffered Saline	This paper		* Use as blocking buffer/antibody diluent indicated for selected antibody applications
Dako Antibody Diluent, Background Reducing	Agilent	Cat# S302283-2	† Use as antibody diluent indicated for selected antibody applications
Dako Protein Block, Serum-Free	Agilent	Cat# X090930-2	† Use as blocking buffer indicated for selected antibody applications
DAPI	VWR	Cat# 89139-054	1 µg/mL PBS
Software and algorithms			
Fiji/ImageJ	PMID: 22743772	RRID:SCR_002285	
CryptCount	https://github.com/twheele3/ccproc		See Chapter 2
R; RStudio	R Project for Statistical Computing; RStudio	RRID:SCR_001905; RRID:SCR_000432	
Zen	Zeiss	RRID:SCR_013672	

Mice

Reg4$^{DTR\text{-}Red}$ (Jackson Laboratory (Jax), Bar Harbor, ME, USA) and *Reg4*$^{DTR\text{-}Red}$;*Lgr5*$^{EGFP\text{-}IRES\text{-}CreERT2}$ (Jax) mice were housed in a specific pathogen-free environment under strictly controlled light cycle conditions, fed a standard rodent lab chow, and provided water ad libitum. Mice were sacrificed at 6-8 weeks of age by direct cervical dislocation.

Histology

Colons dissected from mice were flushed with ice-cold PBS, flayed longitudinally, pinned flat, and then fixed in 4% PFA/PBS for 60 minutes at room temperature with light oscillation. Fixed colons were washed 3x5 minutes in PBS and incubated in 30% sucrose overnight at 4°C. Colons were sectioned transversely into 3-4 pieces then blocked in OCT in transverse order to preserve proximal-distal orientation of the tissue. 15 µm sections were taken on Superfrost™ Plus Slides (Fisher, Pittsburgh, PA, USA).

Immunohistochemistry

Slides were washed 3x3 minutes in PBS and blocked for 1 hour at room temperature in blocking buffer, then overnight at 4°C with primary antibody diluted in staining buffer. Slides were washed 3x3 minutes in PBS then stained with secondary antibody diluted in blocking buffer. Slides were washed 3x3 minutes in PBS, counterstained with DAPI, and mounted with N-propyl gallate mounting medium.

Imaging

Slides were imaged via confocal microscopy using a Zeiss LSM-880 system, with aperture set to software-calculated Airy unit for selected tracks. Imaging was constrained to regions of the tissue correlating to the distal half of the colon. Images were collected in z-stacks of 5-10 images taken 0.31-1.0 μm apart. Images presented were adjusted for brightness and contrast to scale to a visible range for significant features.

Statistics

Statistical analysis was performed using R. Morphometric data of blinded fluorescent images were hand annotated for crypts in Fiji (Schindelin et al., 2012) and processed in R for crypt structure using my own software CryptCount (https://github.com/twheele3/ccproc) (see Chapter 2). **Biological replicates** consisted of individual mice per treatment condition (n = 2 mice for Lgr5-GFP;Reg4-RFP, 4 mice for Reg4-RFP). 15-30 well-formed crypts (visible in cross-section from muscularis mucosa to lumen) were counted per marker per mouse.

Bridge to Chapter IV

Within this chapter I provided a breadth of data on different cell types and signaling pathways within the colonic epithelial niche. This provides a great amount of context as to how crypts function in homeostasis, with the next step to apply this model toward a significant issue regarding perturbation and recovery of the colon. While many models focus on downstream outcomes of systemic perturbation, one relatively unexplored aspect of crypt behavior to look at is the finer dynamics of reorganization during the onset of perturbing pressure, which has the potential to give insights into transitional states and how cell populations adapt (Bohin et al., 2020). Using the control data from this chapter as a starting point, I went on to perturb the colonic epithelium by ablating cells in the Reg4-lineage in order to probe a poorly understood event where crypts maintained proliferation while *Lgr5*+ stem cells were lost.

CHAPTER IV

ABLATION OF COLONIC EPITHELIAL REG+ SUPPORT CELLS INDUCES NOTCH-INDEPENDENT REGENERATION AND MESENCHYMAL REMODELING

*This chapter contains previously published co-authored material

Wheeler T.W., Zemper A.E. Ablation of Reg4+ support cells induces Notch-independent regeneration and mesenchymal remodeling. (In revisions, Life Science Alliance) Preprint doi: https://doi.org/10.1101/2022.01.28.478243

Author contributions: T.W.W. performed all experiments, data processing, and experimental design. T.W.W. and A.E.Z. wrote and edited the manuscript. A.E.Z. provided supervision, project administration, and funding.

Abstract

The colonic epithelium harbors a complex network of adult stem cells that integrate signals from many supporting cells to assist in their decision making. In this study, we ablate an epithelial secretory support cell population characterized by Reg4 expression, to investigate the systemic impact on stemness-related cell signaling pathways. Ablation of these cells results in a hyperproliferative state as well as paradoxical activation of Notch signaling, with the proliferative effect continuing even during Notch inhibition. Reg4+ cell ablation also causes an unexpected remodeling of the mesenchyme. We observe increased presence of Pdgfra-high fibroblasts and an expanded network of smooth muscle myofibroblasts, suggesting that Reg4-ablation reorganizes signaling between epithelium

and mesenchyme. These changes occur in the absence of any significant immunological inflammatory response. Our data demonstrate that Reg4+ cells are critical directors of homeostatic epithelial-mesenchymal signaling. Further, this ablation model is an *in vivo* system for probing cell-cell interactions in the colonic stem cell niche.

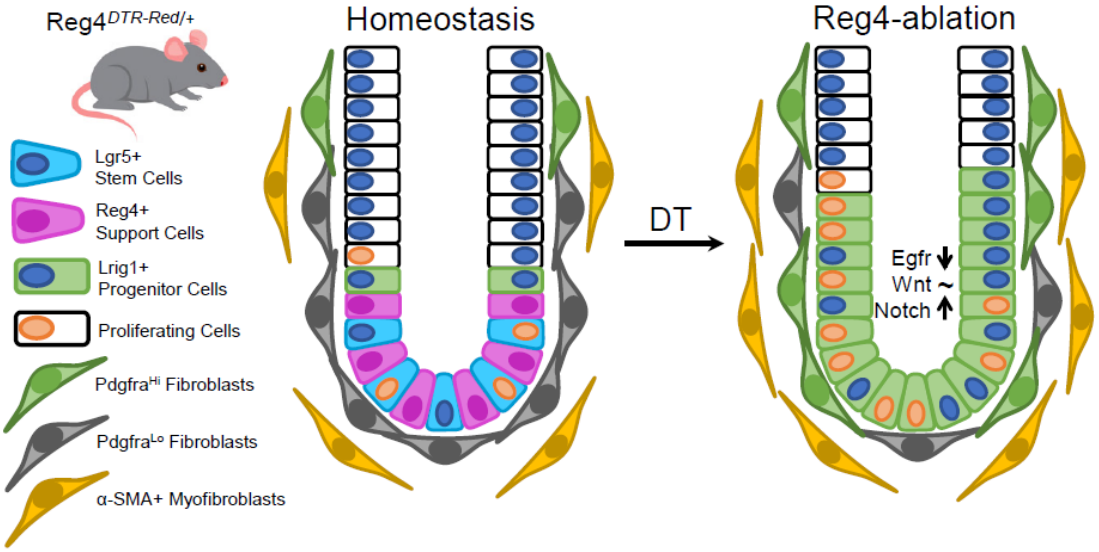

Figure 4.1. Graphical abstract, model for effects of Reg4-ablation

Introduction

Epithelial stem cells are present across many genera in biology (Chacón-Martínez et al., 2018) and generally, stem cells act as population drivers - they give rise to more differentiated daughter cells which are responsible for the day-to-day duties of a given tissue. These cells often integrate extrinsic cues from both adjacent epithelial cells and their non-epithelial microenvironment to make decisions. The cells immediately surrounding the stem cell comprise its “niche”, and the stem cells exchange information with these cells throughout their life span (Chacón-Martínez et al., 2018; Meran et al., 2017). For tissues that constantly regenerate like the skin (Chacón-Martínez et al., 2018), blood (Wei & Frenette, 2018) and gastrointestinal epithelium (Chacón-Martínez et al., 2018; Meran et al., 2017), these cellular decisions are critical to maintaining the life of the tissue throughout an organism’s lifespan. Cells within these tissues have evolved mechanisms for handling changes within their environment and are generally thought of as dynamically-regulated and highly adaptable. Environmental changes can come in many forms. For the skin, it may be a burn or a scrape, resolved by epidermal stem cells dividing to generate additional skin cells to cover the wound, in combination with an inflammatory response that mitigates infection (L. Chen et al., 2018). But how are these injuries sensed? Why do some environmental changes elicit stem cell-based responses that differ from others? In short, what drives this adaptation to promote tissue maintenance over tissue death? To answer these questions, it’s helpful to take a reductionist approach by eliminating individual signals or cell populations, and then measuring the response in the stem cells. This is the approach we have taken to understanding colon adaptability.

In the colon, the cellular structure is critical to its function. The columnar epithelium is arranged as a single layer, acting as a barrier to intestinal contents, and is composed of millions of crypts (Potten, 1998). These crypts are U-shaped invaginations that harbor the stem cells, and their niche, at the crypt-base (Meran et al., 2017). The stem cells are highly proliferative, dividing once per day in mice and in humans, to generate a continual supply of differentiated daughter cells that are responsible for colon function. These stem cells have a unique molecular marker, Leucine Rich Repeat Containing G Protein-Coupled Receptor 5 (Lgr5), that distinguishes them from the other cells in surrounding epithelium (Barker et al., 2007). The cells that live on either side of these stem cells are differentiated cells and they also express a unique marker called Regenerating Islet-Derived Protein 4 (Reg4). Reg4+ cells express a myriad of ligands that bind to the stem cells to instruct a number of cellular functions, including regulation of proliferation and restricting differentiation. Recently, it was shown that ablation of these Reg4+ cells led to loss of Lgr5 expression in the remaining cells in the niche, and instead of collapsing, the crypts retained their unique structure and the cells within them continued to proliferate (Sasaki et al., 2016). The authors posited the cells remaining in the crypt may differentiate in response to ablation of Reg4+ cells, however this suggestion is at odds with the proliferative response they observed. Our study investigates this unexpected proliferative response, and we show that in the face of acute disruption the stem niche can immediately adapt to persist and recover. We show this is accomplished by a paradoxical shift in cellular signaling programs in the remaining cells of the crypt, accompanied by the reorganization of critical mesenchymal cell populations.

Results

Reg4 ablation induces transient hyperproliferation

Ablation of Reg4+ cells was previously shown to induce a loss of Lgr5+ stem cells without the loss of crypt-based proliferation (Sasaki et al., 2016). As stem cell loss generally induces a lack of proliferation and eventual organ atrophy, we first sought to more fully resolve this unexpected impact of Reg4-ablation on colon stem cells and proliferation throughout the course of this 6-day time period. We used Reg4dsRed-DTR/+ mice to ablate Reg4+ cells via daily diphtheria toxin (DT) injections as previously described (Sasaki et al., 2016), examining daily time points in a 6-day time course (Figure 4.2A). Control mice were injected with phosphate buffered saline (PBS) vehicle. As with the previous study, we observe the loss of Lgr5 expression by the 6th day of DT-driven Reg4+ cell ablation (Figure 4.2C,C’). We also observe an increase in total cell number per crypt, (Figure 4.2B), with the average cells per crypt cross-section increasing from 43 cells/crypt in vehicle to an average maximum of 53 at day 5 of Reg4-ablation. The driver of hyperplasia, cellular proliferation, increases soon after the start of time course (Figure 4.2D), with a significant increase in proliferation between 2-4 days of daily DT injections. The average maximum proliferation we observe is 33 Ki67+ cells/crypt at the 3-day timepoint, compared to an average of 11 Ki67+ cells/crypt in vehicle-injected controls (Figure 4.2D'). These data define a specific time course of hyperproliferation in response to ablation of Reg4+ cells within the first week of ablation.

Reg4 ablation expands a hyperproliferative progenitor cell pool

We sought the source of this transient hyperproliferation, by examining the progenitor epithelial cell pool to determine whether it is transiently expanding in response to Reg4-ablation, or whether an existing stem cell pool simply increases its proliferation

---

Figure 4.2. Reg4-ablation induces transient hyperproliferation.

(A) Overview of Reg4-ablation time course, with diphtheria toxin (DT) or Vehicle (Veh; PBS) administered via intraperitoneal injection daily. Mice were sacrificed 24 hours after last injection, and colonic tissue collected 1-6 days after the start of injections. Vehicle injections were administered for 4 days. Diagram colors correspond to graph time points. **(B)** Total cells per well-formed crypt cross-section were measured across all stains (100-200 crypts per mouse). **(C)** *In-situ* hybridization for stem cell marker *Lgr5* (green) indicates marker Ki67 (green) indicates a significant increase in proliferation increases significantly in response to Reg4-ablation, quantified in **D'**. **(E)** Immunofluorescence for progenitor marker Lrig1 (green) indicates a significantly expanded progenitor compartment during Reg4-ablation, quantified in **E'**. Nuclei are stained with DAPI (magenta). Graphs represent mean ± sd of mouse means, with individual mice represented as points. 15-25 crypts were measured per mouse for immunofluorescence and *in-situ* hybridization (n = 2-5 mice/group). Significance is calculated by nested Tukey test using crypts as random effect. *p*-values indicated: $* < 0.05$, $** < 0.01$, $*** < 0.001$. All scale bars indicate 10 μm. **(F)** Western blot of purified mucosal protein indicates a 1.5-fold increase in Lrig1 in 3-day DT treated tissue compared to vehicle (n = 8 mice/group). GAPDH is used as a loading control. Significance indicated by *p*-value on graph, calculated by two-tailed unpaired Student's t-test.

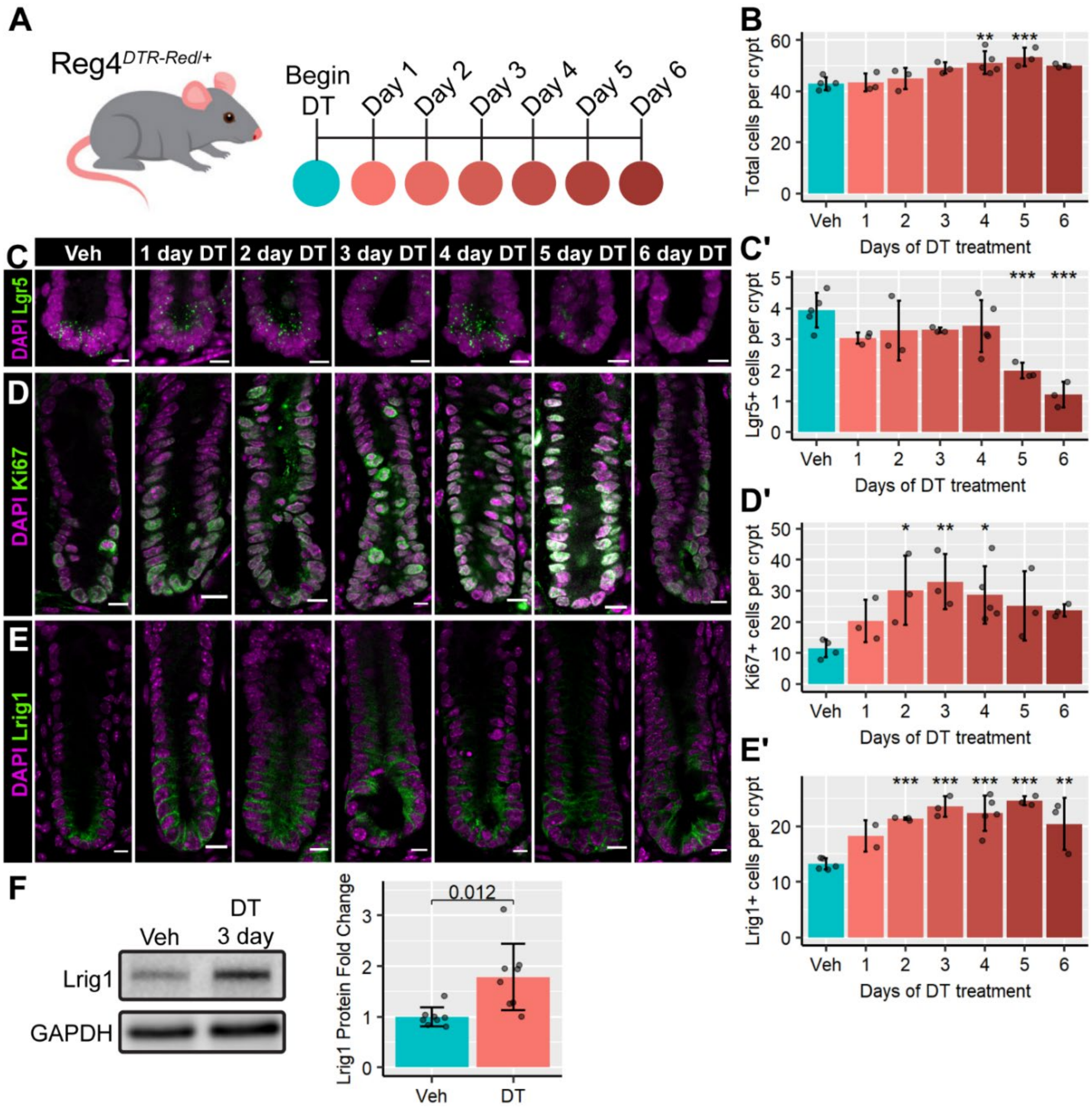

rate. To address whether there were any dynamic, day-to-day changes to the pool of stem cells, we first examined the expression of *Lgr5*, which we observe is ultimately lost by day 6. We find no significant changes to the number of *Lgr5*+ cells until the 5-6 day time point when expression diminished (Figure 4.2C), which concurred with the previous study characterizing Reg4+ cells as support cells of the Lgr5+ cell population (Sasaki et al., 2016). We next examined the expression of Lrig1, an established stem and early progenitor cell marker in the colon (Powell et al., 2012). We see a significant increase in Lrig1-

expressing (Lrig1+) cells and we observe this increased Lrig1+ population is maintained at an average of 1.7-fold above the vehicle-injected animals during this hyperproliferative phase (days 2-4) of Reg4-ablation (Figure 4.2E). This increase in Lrig1 expression was also verified by western blot, where Lrig1 is increased 1.5-fold at 3 days of Reg4-ablation (Figure 4.2F). To determine if Lrig1+ cells were responsible for the hyperproliferation we observe, we labeled proliferative cells within the crypt using a 2-hour pulse of 5-ethynyl-2'-deoxyuridine (EdU) on day 3 of Reg4-ablation (Figure 4.3A). These mice have a 5.3-fold increase in total EdU-labeled cells per crypt (Figure 4.3B), which agrees with the increase in Ki67 expression we observe (Figure 4.2D, D'). This expansion of EdU+ cells is concentrated within the Lrig1-expressing region of the crypt (Figure 4.3C). We quantified the EdU+;Lrig1+ cells and find the mitotic index of the Lrig1+ region increased from 0.12 in vehicle to 0.38 in the ablated crypts (Figure 4.3D). Taken together, our data suggest

---

Figure 4.3. The hyperproliferation in Reg4-ablation is constrained to an expanded Lrig1-expressing region

(A) Colonic tissue from Reg4-DTR-Red/+ mice treated with Vehicle (Veh) or diphtheria toxin (DT) daily for 3 days, followed by a 2-hour trace of 5-ethynyl-2'-deoxyuridine (EdU) before mice were sacrificed. In the colored panels, representative images of DT and veh treated tissue were examined for the presence of proliferating cells (EdU labeling, magenta), nuclei by DAPI staining (white), and progenitor compartment by immunofluorescence for Lrig1 (green). Single color stains for Lrig1 and Edu are shown in the white-on-black panels. All scale bars indicate 25 μm. **(B)** Comparison of total EdU+ cells per crypt between Veh and DT. **(C)** EdU+ cells per crypt that do not coexpress Lrig1 (Lrig1-) or do coexpress Lrig1 (Lrig1+). **(D)**. Comparison of the fraction of total cells that proliferated (mitotic index) between Veh and DT in the Lrig1+ region. n = 4 mice/group, 40-60 crypts per mouse. Graphs represent mean ± sd of mouse means, with individual mice represented as points. Significance indicated by *p*-values on graphs, determined by nested Tukey Test using crypts as random effect.

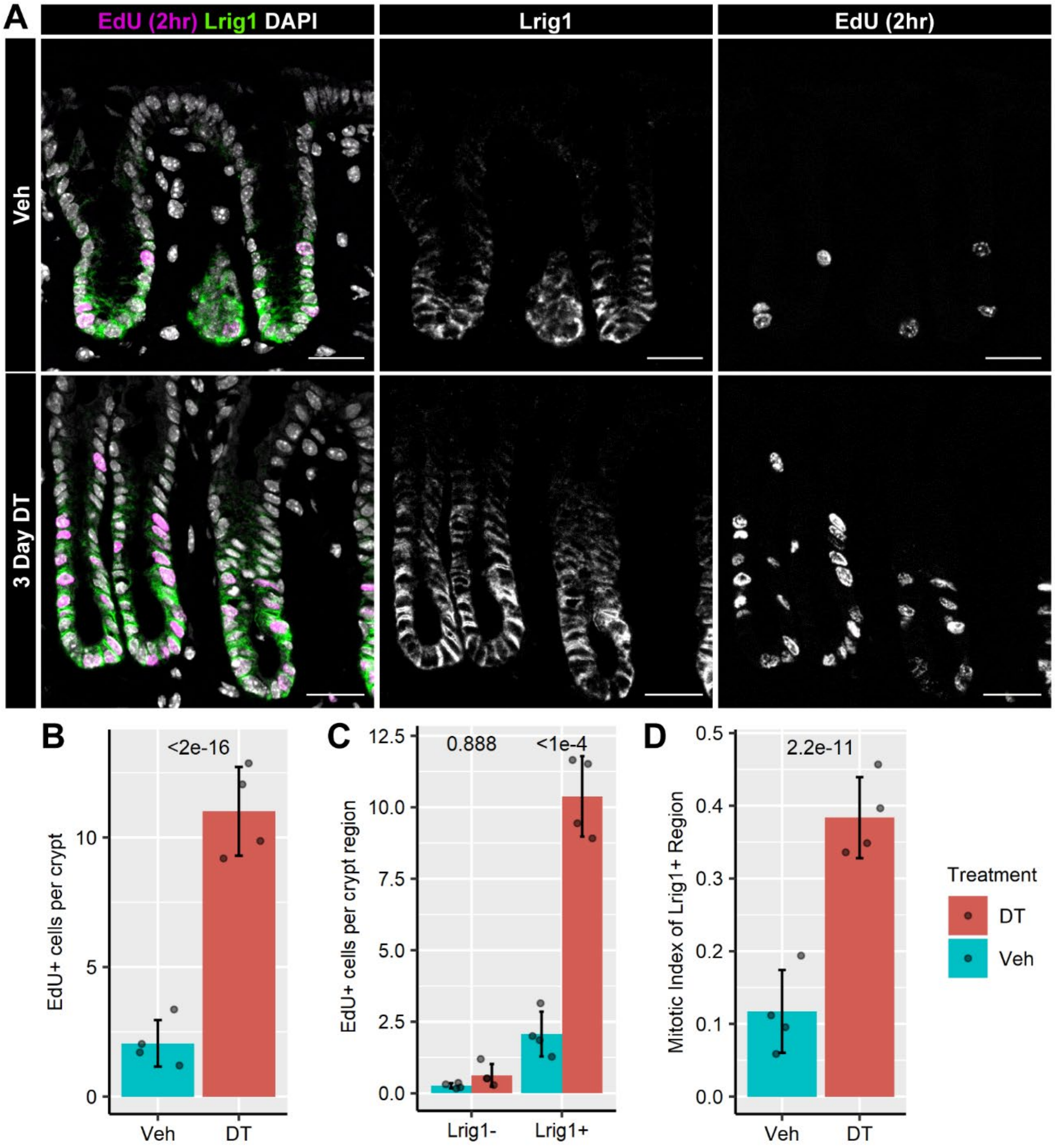

that crypt epithelial progenitor proliferation is significantly altered from homeostasis and the hyperproliferative response to Reg4+ cell ablation occurs in a dedicated pool of Lrig1+ cells.

Reg4 ablation does not induce an inflammatory response

As epithelial hyperproliferation and hyperplasia are hallmarks of gut injury and repair (Davies et al., 2009; Zhang et al., 2012), we wondered whether this phenotype might be due to the stress of ablation inducing a macrophage-based inflammatory response that is also characteristic of injury models (L. Chen et al., 2018). To address this, we probed ablated tissues for expression of the macrophage marker F4/80, to determine if macrophage infiltration occurred after ablation (Figure 4.4A), as typical of inflammation after injury (Jones et al., 2018). In comparing vehicle-treated with DT-treated tissue, we see no significant difference from 1-4 days of treatment, using colons from mice subjected to dextran sodium sulfate (DSS) treatment as a positive control of macrophage infiltration (Novak et al., 2016). DSS-treated mice have a 2.3-fold increase in mean intensity of F4/80 compared to vehicle (Figure 4.4). We do observe significant macrophage infiltration at 5-6 days after Reg4-ablation, but not until after the peak of hyperproliferation. Our results show that the expansion in proliferation in this model occurs in the absence of a classic macrophage-driven inflammatory response.

Signaling pathways affecting stem cell maintenance are perturbed during Reg4 ablation

As epithelial hyperproliferation and hyperplasia are often driven by changes in specific cellular signaling programs, we next asked which signaling pathways were specifically perturbed in response to Reg4-ablation at the peak of proliferation (day 3). In the colon, there are numerous critical cell signaling pathways that guide stem cell decision making, and we prioritized three of these pathways in our analyses: Wnt (Nusse & Clevers, 2017), Epidermal growth factor receptor (Egfr) (Dubé et al., 2018), and Notch (Pellegrinet et al., 2011). Wnt signaling is required for crypt-based proliferation (Nusse & Clevers, 2017), so we hypothesized that Wnt signaling would be increased immediately

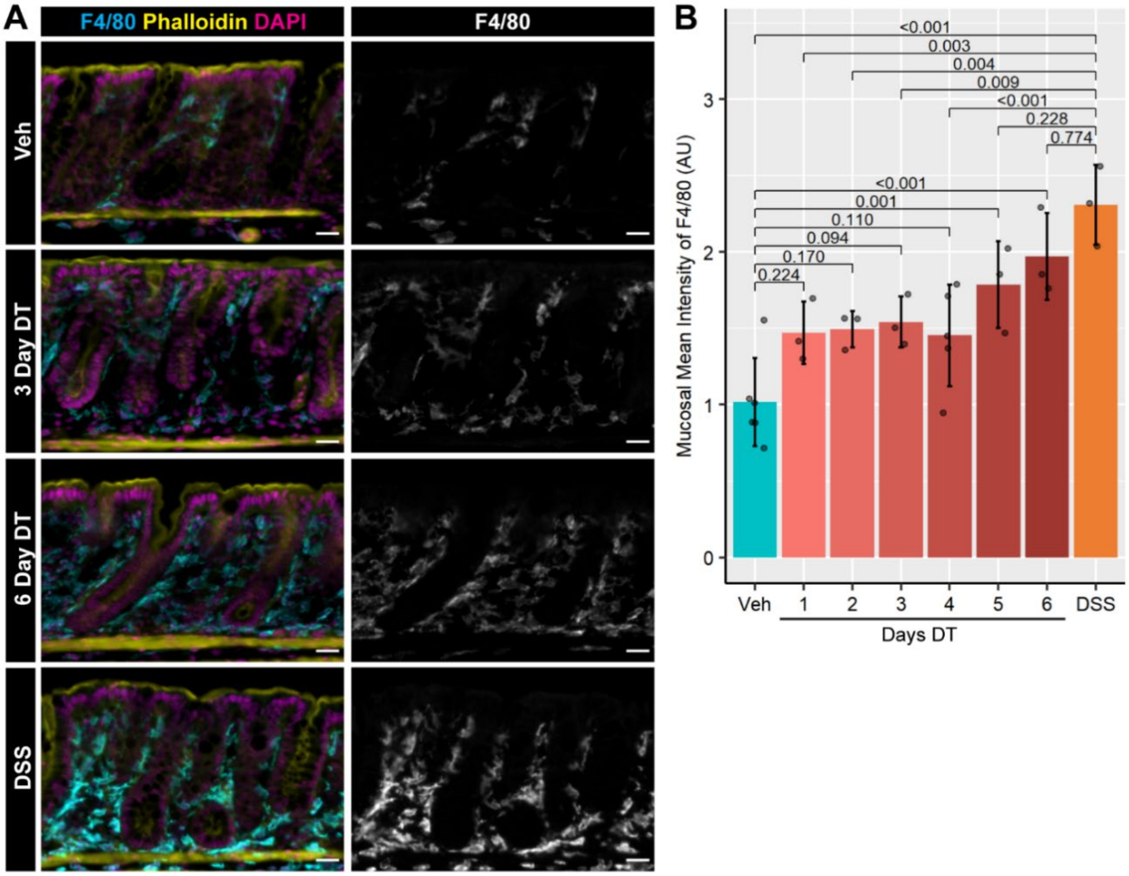

Figure 4.4. Macrophage-driven inflammation is not significantly increased in the initial proliferative response to Reg4-ablation

(A) Colonic tissue from Reg4-DTR/+ mice treated diphtheria toxin (DT), comparing to mice treated with vehicle (Veh) for 4 days as a negative control, and mice treated with 3% dextran sulfate sodium (DSS) in drinking water for 7 days followed by 3 days of recovery as a positive control for elevated macrophage infiltration. Presence of macrophages is indicated by F4/80 immunofluorescence (cyan), epithelial brush border is indicated by phalloidin immunofluorescence (yellow), and nuclei indicated by DAPI staining (magenta). Representative Images shown are from mice treated for 3 and 6 days with DT. Macrophage infiltration for all mice is in the single color (white on black) panels. **(B)** Quantification of mean intensity of F4/80 staining in total mucosal area across all groups indicates no significant difference between Vehicle and DT-treated mice, contrasted with significantly increased staining in DSS-treated tissue. Graphs represent mean ± sd of mouse means, with individual mice represented as points. n=3-5 mice/group, 5-7 images per mouse, with each image capturing 0.302 ± 0.060 mm^2 mucosal area (mean ± sd). Significance indicated by *p*-values on graphs, determined by nested Tukey Test using images as random effect. All scale bars indicate 25 µm.

after Reg4-ablation due to the increase in the progenitor pool. An increase in variance of the Wnt signaling mediator, non-phospho-β-catenin (active), is detected in Reg4-ablated colonic tissue cell lysates (Figure 4.5A), suggesting perturbed Wnt pathway activation. Despite this, the downstream expression of Wnt targets remain relatively unchanged at this 3-day timepoint, with no significant changes to *Lgr5*+ cells (Figure 4.2C), *Lgr5* transcription (Figure 4.7), or cMyc patterning (Figure 4.8). As Reg4+ support cells provide Egfr and Notch support to the stem cells (Sasaki et al., 2016), we expected that these pathways would be significantly downregulated in the epithelium after Reg4-ablation. We find that Reg4-ablation causes a significant reduction in Egfr pathway activation (Figure 4.5A). While total Egfr expression is not significantly changed, phospho-Egfr expression (activated Egfr) decreases to 0.6-fold from expression levels in vehicle-treated mice. The downstream mediators of Egfr signaling, Erk1/2, are also significantly less expressed and activated, with Erk1/2 expression reduced to 0.7-fold and phospho-Erk1/2 reduced to 0.5-fold that of vehicle. We probed for Notch signaling using Notch1 NTM (Notch transmembrane-intracellular fragment) and NICD (Notch intracellular domain) as

---

Figure 4.5. Reg4-ablation perturbs stemness-associated pathways

(A) Left panel: Western blot analysis comparing colonic mucosal tissue treated with Vehicle (Veh) or diphtheria toxin (DT) for 3 days. Egfr pathway proteins are detected with Egfr, p-Egfr, Erk1/2 and p-Erk1/2. Wnt signaling is detected by the presence of activated (non-phos) β-catenin, and Notch signaling was assessed by the detection of activated Notch1 (Notch1 transmembrane domain (NTM) and Notch1 intracellular domain (NICD)). Right panel: quantification of Western blot expression data (n=5-8 mice/group). GAPDH is used as a loading control. Significance indicated by *p*-values on graph, calculated by two-tailed unpaired Student’s t-test. **(B)** Immunofluorescence for Notch ligand Dll1 (green) indicates a reduction in Dll1-expressing crypt cells during Reg4-ablation time course, quantified in **B’**. **(C)** Immunofluorescence for Notch ligand Dll4 (green) indicates a reduction in Dll4-expressing crypt cells during Reg4-ablation time course, quantified in **C’**. Nuclear staining indicated by DAPI (magenta). Graphs represent mean ± sd of mouse means, with individual mice represented as points. 15-25 crypts were measured per mouse (n = 3-5 mice/group). Significance is calculated by nested Tukey test using crypts as random effect. *p*-values indicated: * < 0.05, ** < 0.01, *** < 0.001. All scale bars indicate 10 μm.

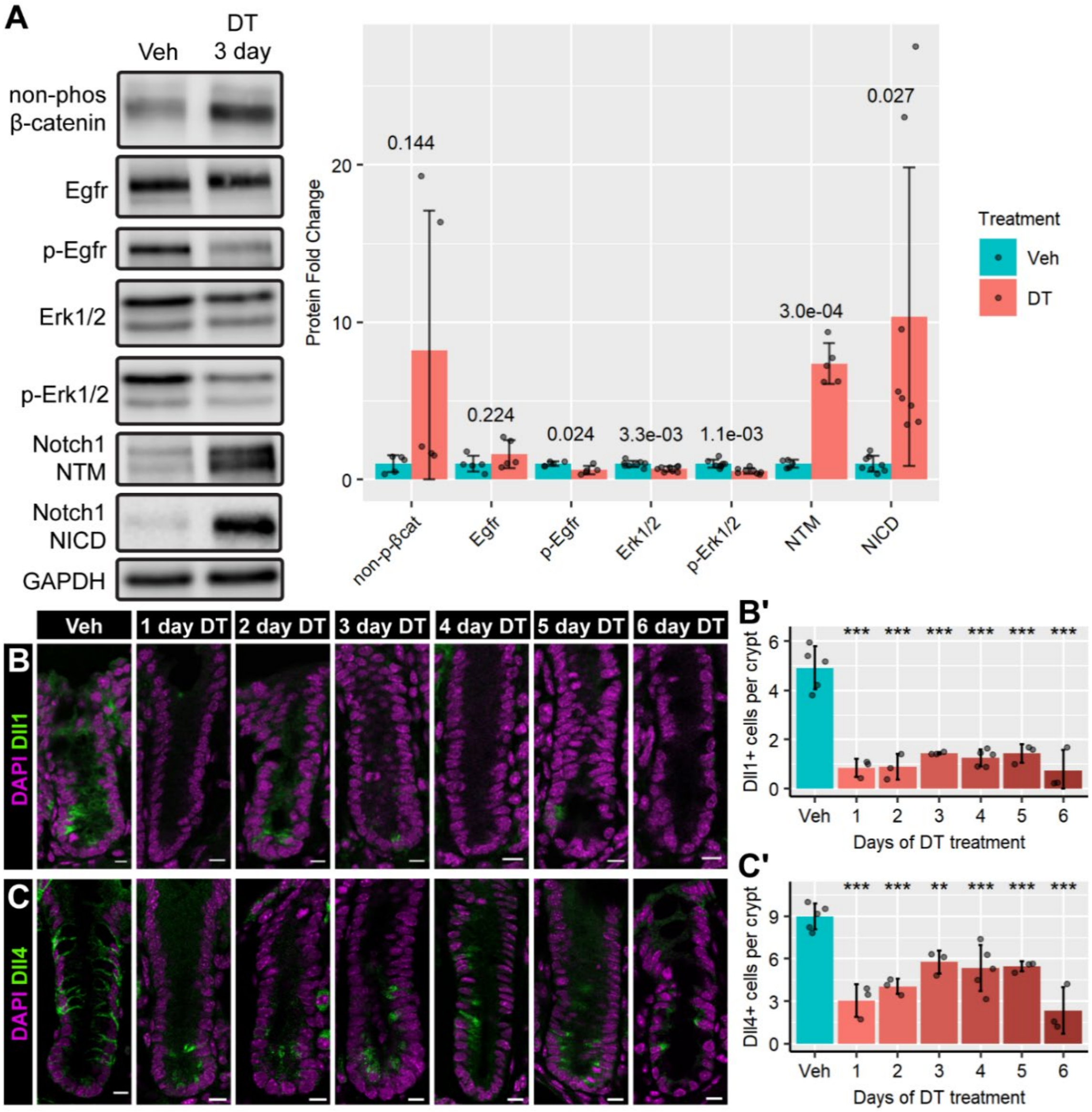

indicators of activated Notch (Zhdanovskaya et al., 2021), and find that Reg4-ablation causes a significant increase in both (Figure 4.5A). These findings of continued Notch signaling are especially notable as Reg4-lineage cells are thought to be the primary expressors of Dll1 and Dll4 (Figures 4.6, 4.7), the two primary Notch ligands expressed in the colonic epithelium (Pellegrinet et al., 2011). In Reg4-ablation, the number of cells expressing Notch ligands Dll1 and Dll4 are significantly decreased (Figure 4.5B,C)

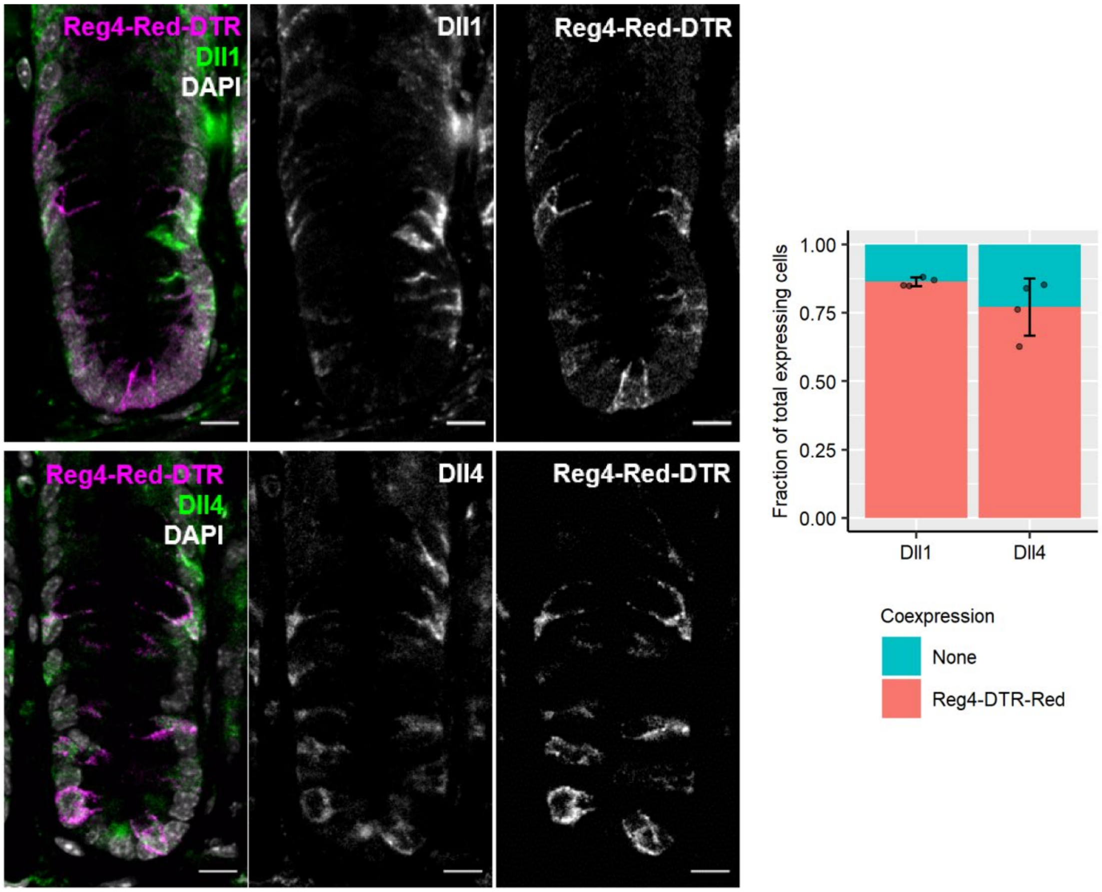

Figure 4.6. Notch ligand expression in the colonic crypt

Colonic tissue from Reg4-DTR-Red/+ mice. Notch ligands Dll1 and Dll4 are indicated by immunofluorescence (green), with Reg4-DTR-Red fluorescence indicated (magenta), and nuclei stained with DAPI (gray). Dll1 and Dll4 are primarily expressed by cells from a Reg4+ lineage (Reg4-DTR-Red) in the colonic epithelium, constituting 79% and 76% of total ligand-expressing cells, respectively (n=4 mice). Scale bars indicate 10 µm.

across all timepoints. Despite the loss of Notch ligands, we show continued Notch activation based on transcription of the Notch-activated transcriptional regulator *Hes1* (Figure 4.7) (Liang et al., 2019). Taken together, our results suggest signaling pathways affecting stem cell maintenance are perturbed during Reg4 ablation.

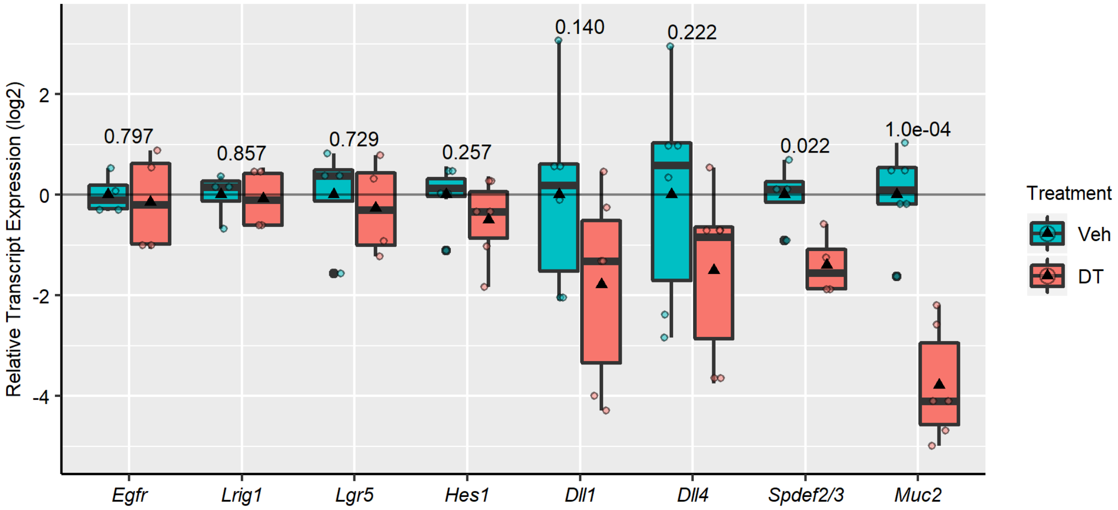

Figure 4.7. Reg4-ablation causes no significant change to relative transcription of several stemness-associated pathways, but reduces secretory transcription

qRT-PCR was performed on mucosal purified RNA from colonic tissue from Reg4-DTR-Red mice after 3 days of vehicle (veh) or diphtheria toxin (DT). No significant effect is observed in stemness-linked pathways (*Egfr*, *Lrig1*, *Lgr5*, *Hes1*), but relative transcription of secretory markers *Spdef2/3* and *Muc2* are significantly reduced. Boxplots represent quartiles with triangles as group mean (n=4-6 mice/group). Statistics taken with two-tailed unpaired Student's t-test, *p*-values indicated on graph.

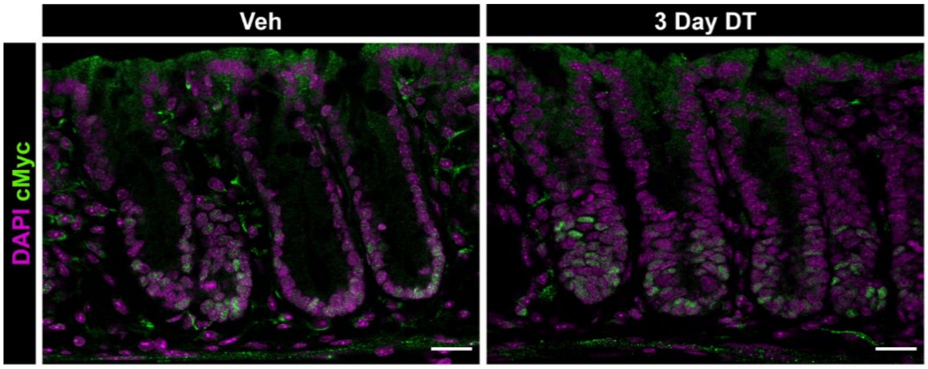

Figure 4.8. Patterning of cMyc, a downstream Wnt target gene, is not distinctly changed by Reg4-ablation

Colonic tissue from Reg4-DTR-Red/+ mice treated with vehicle (Veh) or diphtheria toxin (DT) for 3 days. Immunofluorescence of cMyc (green) shows no distinct changes in qualitative expression levels between Veh and DT. Nuclei are indicated by DAPI staining (magenta). Scale bars indicate 25 µm.

Notch signaling is dispensable for the colon's proliferative response to Reg4-ablation

Notch regulation is associated with proliferation in the intestinal tract (Bohin et al., 2020; Droy-Dupré et al., 2012; Pellegrinet et al., 2011), thus our next step was to test whether Notch activation was necessary for Reg4-ablation induced hyperproliferation. We conducted a dual time course of Reg4-ablation and Notch inhibition using the pan-Notch inhibitor Dibenzazepine (DBZ) (Bohin et al., 2020; Droy-Dupré et al., 2012) in a staggered time course (Figure 4.9A). We initiated Reg4-ablation 24 hours prior to Notch inhibition in order to initiate the proliferative trajectory. At 24 hours after ablation, we injected DT and DBZ for a subsequent 2 days to allow Notch inhibition to take effect. Two hours before

Figure 4.9. Notch inhibition does not downregulate hyperproliferation during Reg4-ablation

(A) Overview of dual Reg4-ablation and Notch inhibition time course to ablate Reg4-DTR-Red-expressing cells with diphtheria toxin (DT) and inhibit Notch signaling with γ-secretase inhibitor XX dibenzazepine (DBZ), followed by a 2-hour trace of 5-ethynyl-2'-deoxyuridine (EdU) before sacrifice. **(B)** Representative images of colonic tissue with EdU labeling (cyan) to detect proliferation, epithelial brush border by phalloidin immunofluorescence (yellow) and nuclei by DAPI staining (magenta). Arrows indicate examples of obvious secretory cells, visible as more bulbous cells highlighted by phalloidin. **(C)** Western blot of Notch1 intracellular domain fragment (NICD) shows successful inhibition of Notch by DBZ with and without DT, contrasting with Veh and DT (n=2 mice/group). GAPDH is used as a loading control. Significance indicated by *p*-value on graph, calculated by two-tailed unpaired Student's t-test. **(D)** Comparison of total proliferation (EdU+) cells per crypt between all conditions, indicating significant differences between the DT treatment axis (n=4-6 mice/group). **(E)** A graph of mouse weights, relative to starting weight, over the time course. Precipitous weight loss occurs in DT+DBZ treatment compared to Veh and DT treatment alone. Veh and DT group data taken across all mice from study (n = 4 (DT, DT+DBZ) 28 (Veh) 43 (DT)). Significance comparisons indicated by *p*-values on graph, calculated by two-tailed unpaired Student's t-test. **(F)** The fraction of proliferating cells per position relative to crypt base (position 0) is compared between DT and DT+DBZ treatments (n=4 mice/group). The proliferative region is shifted significantly higher on the crypt axis in DT+DBZ treated mice compared to DT. For immunofluorescence, 15-25 crypts measured per mouse. Graphs represent mean ± sd of mouse means, with individual mice represented as points. Significance indicated by *p*-values on graphs, determined by nested Tukey Test using crypts as random effect. All scale bars indicate 25 μm.

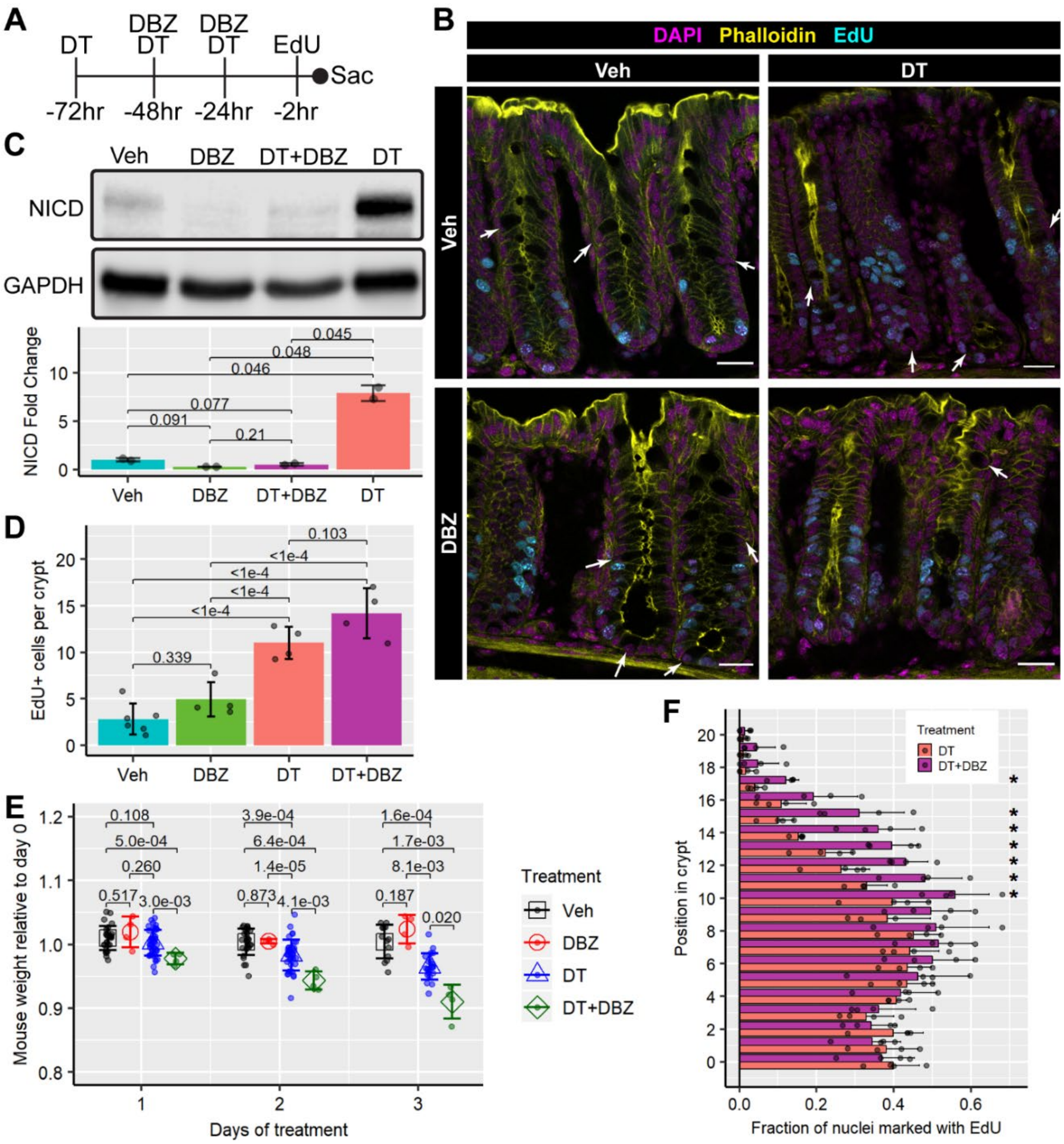

sacrifice, we administered an EdU pulse to capture the proliferation occurring at that time. We observe intact gross mucosal and crypt morphology in all experimental conditions of this time course, although the distribution of visible secretory cells varied greatly by condition. DBZ-treated crypts show an increased density of secretory cells compared to vehicle, while DT-treated crypts show reduced secretory cell density irrespective of DBZ treatment (Figure 4.9B). Activated Notch1 is reduced in DBZ-treated mice, even with DT treatment (Figure 4.9C). We find that DBZ treatment alone does not cause a significant change to proliferation or body weight relative to vehicle (Figure 5D,E), and DT+DBZ treatment does not significantly increase proliferation relative to DT alone (Figure 4.9D), though body weight declines significantly faster in dual treatment compared to all other groups (Figure 4.9E). Despite the lack of significant change to total proliferation within crypts following Notch inhibition, we detect a significant shift in the location of proliferative cells, comparing Reg4-ablated mice with and without Notch inhibition. With respect to cell position from crypt base (position 0), proliferation shifts further up in crypts treated with DT+DBZ relative to DT alone (Figure 4.9D). Together, our results demonstrate Notch signaling is dispensable for hyperproliferation induced by Reg4-ablation, and inhibition of Notch signaling after Reg4-ablation causes proliferation to occur higher in the crypts.

The mesenchyme is remodeled during Reg4 ablation

Mesenchymal cells that surround the crypts are a critical component of colonic stem cell regulation (David et al., 2020; Degirmenci et al., 2018; Stzepourginski et al., 2017). We wondered whether mesenchymal cells, as a niche component, are also affected by Reg4-ablation. Groups of stem cell- ‘supporting’ and - ‘antagonizing’ fibroblasts were recently characterized based on expression of Platelet-derived growth factor receptor-α (Pdgfra)-low and -high expression, respectively. Pdgfra-high fibroblasts normally localize to the luminal surface of the colon in homeostasis (David et al., 2020). Using this marker, we examined patterns of Pdgfra expression relative to the crypt axis in ablated mice and find Pdgfra-high fibroblasts additionally localize to the crypt base (Figure 4.10A). To quantify this, we counted the number of epithelial cells, that are also adjacent to Pdgfra-high fibroblasts in the bottom half of crypts. Starting at Day 1 after ablation, the epithelial cells within this lower crypt compartment are 3 times as likely to be adjacent to Pdgfra-high fibroblasts, compared to vehicle-treated mice (Figure 4.10B). We also assayed the tissues for the expression of crypt-adjacent myofibroblasts that express α-smooth muscle actin (α-SMA) (Speca, 2012). We find that purified mucosal protein from Reg4-ablated tissue contains a 2.2-fold increase in α-SMA (Figure 4.10C). Comparing α-SMA and Pdgfra patterning to each other, we find that their expression patterns are distinct (Figure 4.10A). Our data show that mesenchymal cell relocation is cell-type dependent after Reg4-ablation. These patterns were consistent across all timepoints, suggesting that ablation of Reg4+ cells rapidly induces fibroblast remodeling within the adjacent mesenchyme.

Figure 4.10. Reg4-ablation induces mesenchymal remodeling

(A) Colonic tissue from Reg4-DTR/+ mice treated diphtheria toxin (DT) daily for 1-6 days, compared to mice treated with vehicle (veh) for 4 days. Representative images show stromal fibroblasts indicated by Pdgfra immunofluorescence (green), structural myofibroblasts indicated by α-SMA immunofluorescence (magenta) and nuclei by DAPI staining (gray). Pdgfra-expressing stromal cells are detected as a distinct set of cells from α-SMA+ myofibroblasts. White-on-black images for Pdgfra and α-SMA are shown beneath the colored panel. In the single color panels, Pdgfra high-expressing cells (white) are apparent in DT-treated tissue around the crypt base (marked with arrows). α-SMA+ myofibroblasts (white) are present throughout the mucosa in all tissues. Scale bars indicate 25 µm. **(B)** Lower-crypt epithelial cells (below dotted line) adjacent to Pdgfra-high stromal cells are significantly increased at all time points of DT treatment. Graphs represent mean ± sd of mouse means, with individual mice represented as points. 15-25 crypts were measured per mouse (n = 3-5 mice/group). Significance is calculated by nested Tukey test using crypts as random effect. *p*-values indicated: * < 0.05, ** < 0.01, *** < 0.001. **(C)** Representative Western blot analysis of mucosal purified protein shows significant fold increase of α-SMA in mucosal isolate of 3-day DT treated tissue (quantification in right panel: n=5 mice/group). GAPDH is used as a loading control. Significance indicated by *p*-value on graph, calculated by two-tailed unpaired Student’s t-test.

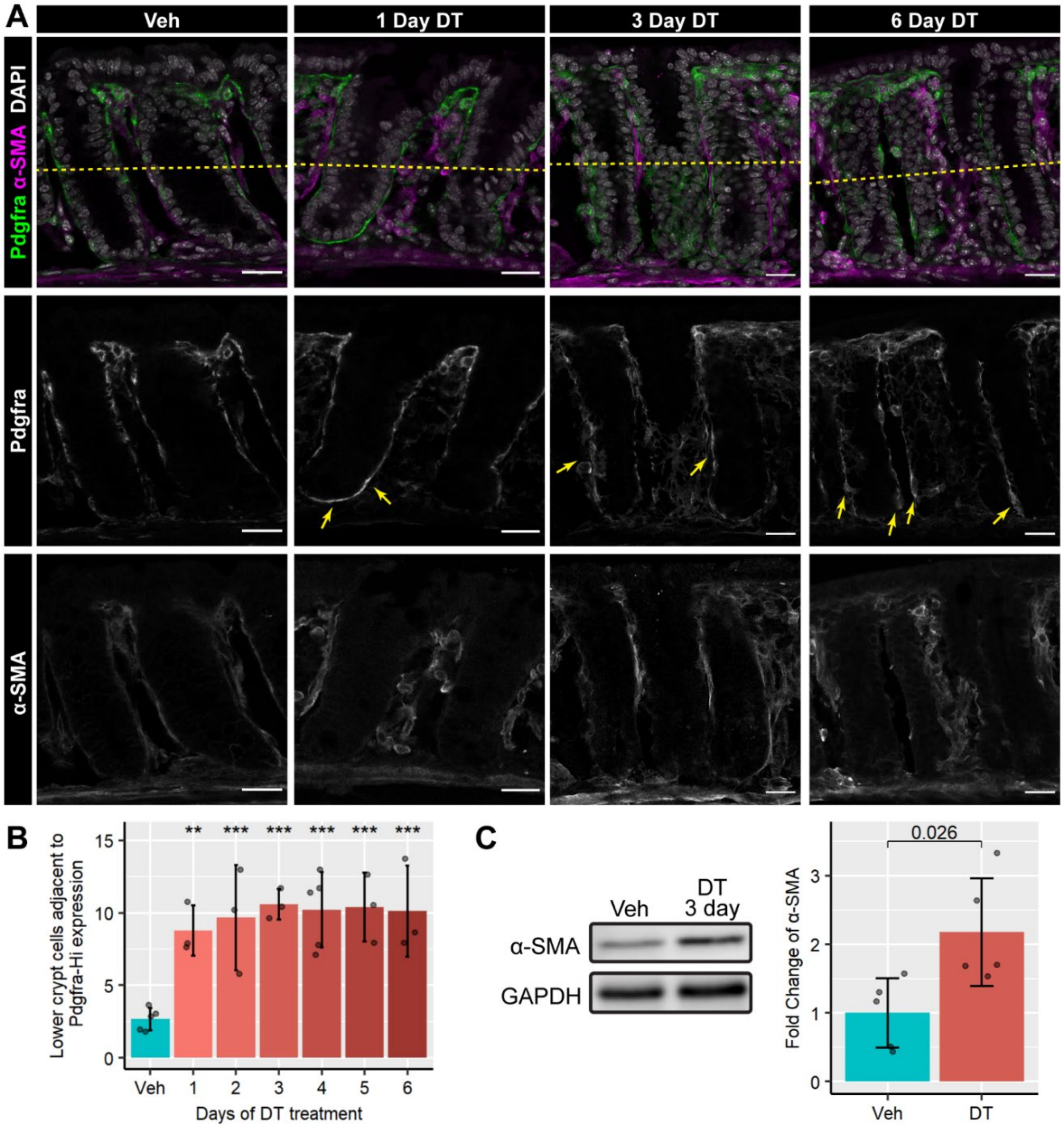

Discussion

In our study, we investigated induced ablation of Reg4+ secretory support cells and showed that in the face of acute disruption, the stem niche can immediately adapt to persist and recover. This recovery is achieved by induced epithelial hyperproliferation and expansion of an epithelial progenitor pool, and is accompanied by a paradoxical shift in cellular signaling programs in the remaining cells of the crypt and the reorganization of critical mesenchymal cell populations.

Reg4+ cells in the colon are often compared to the Paneth cells in the small intestine (van Es et al., 2019), as both are secretory support cells localized to the stem cell niche (Sasaki et al., 2016; van Es et al., 2019). Previous epithelial DTR ablation models in the gastrointestinal tract do not report a proliferative response to ablation (Castillo-Azofeifa et al., 2019; Tian et al., 2011; van Es et al., 2019), suggesting the response we observe is specific to colonic stem cells losing their epithelial support population. Our data suggests that Reg4+ cells are a distinct support cell population and have a distinct role that is different from that of the Paneth cell role in the small intestine. One open question our study does not address is whether the hyperproliferative response to Reg4-ablation is induced by loss of factors supplied by Reg4+ cells, or the act of ablating Reg4+ cells itself. Future studies resolving this question would provide useful insights into both the mechanisms underlying colonic epithelial homeostasis, as well as refine the applicability of this experimental model. We additionally find that *Spdef2/3* and *Muc2* are significantly downregulated by Reg4-ablation (Figure 4.7), and both are key components of the colon's secretory lineage (Qin et al., 2021). This aids in characterizing the systemic impact of Reg4-ablation by illuminating the extent to which the broader secretory lineage is perturbed in this model. This is also contrasted with Paneth cell ablation in the small intestine, in which reserve secretory cells are readily able to compensate for the loss of Paneth cells (van Es et al., 2019); this notable difference in compensatory mechanism may explain some of the systemic response we observe and this represents an important area of future research.

We find that the Reg4-ablation model produces a transient hyperproliferative response reminiscent of other colonic injury models (Kiesler et al., 2015; Mizoguchi et al., 2020) yet it does this in the absence of many of the systemic effects that confound those models and prevent further analysis of molecular mechanisms that drive colonic homeostasis. By contrast, Reg4-ablated colons retain gross crypt and organ morphology, with no significant immune response during the acute period, which often follows tissue injury and obfuscates molecular analysis. Indeed, the Reg4-ablation model permits the dissection of the mechanisms underlying a proliferative response to injury, without other confounding factors present in existing models that induce systemic inflammation.

Disruption of the secretory lineage is associated with many other dysfunctions within gut injury models, and rescue of secretory cells improves the outcome after injury (Shinoda et al., 2010; Z.-J. Sun et al., 2018). These modes of injury are also linked to mesenchymal differentiation leading to fibrosis (Usunier et al., 2021), but it remains poorly understood how epithelial injury causes fibroblasts to promote fibrogenic activity. Our observations of altered fibroblast patterning in response to Reg4-ablation suggest that this system may be similar to other gut injury models in some respects. However, our data indicate that the Reg4-ablation is more of a “reductionist” model for epithelium-mediated colonic fibroblast activation, as the activation happens in absence of an inflammatory response. This model may aid in resolving less-understood mechanisms of fibroblast activation, compared to general injury models which have acute inflammation associated with them. Similar phenotypes are observed in colitis models, where extensive fibrosis is observed (Gregorio et al., 2017). These forms of fibrosis are linked to chronic bowel diseases (Speca, 2012), so a better understanding of the mechanisms through which fibroblast activation occurs may elucidate underlying pathways and help to develop strategies to mitigate fibrotic formation.

There are numerous cell signaling changes after Reg4-ablation. With regards to Wnt signaling, we observe fluctuations in active β-catenin after Reg4-ablation. As β-catenin is a structural protein, adherens junction remodeling that happens after Reg4-ablation may play a part in this phenomenon (Grainger & Willert, 2018). If it is an indicator of Wnt signaling perturbation, this change would likely come from surrounding fibroblasts that supply Wnt ligands (David et al., 2020), since epithelial cells do not express Wnt signaling ligands in the colon (Sasaki et al., 2016). Indeed, the changes we observe in β-catenin activation may be driven in part by the shift we detect in the fibroblasts after ablation. We observe Pdgfra-high fibroblasts shift to the crypt-base in response to Reg4-ablation, and these cells have previously been shown to express noncanonical Wnts and Bmp ligands (David et al., 2020). This shift in signaling would have a profound effect on epithelial cells if the shifted crypt base fibroblasts have similar expression to Pdgfra-high fibroblasts in homeostasis. Whether this shift in these mesenchymal cells directly causes the proliferative changes seen in the epithelial cells, represents a critical avenue for future research. To our knowledge, this is the first example of discrete, directed changes in the epithelial cell population causing a shift in mesenchymal cell localization. It will be important to define the mechanism for the translocation of these cells in future studies.

With respect to Notch signaling, we observe that Reg4-ablation induces a significant increase in Notch1 in the form of both NTM and NICD. Treatment with the γ-secretase inhibitor, DBZ, is sufficient to mitigate this increased Notch1 activation, suggesting that the increased Notch activation we see in Reg4-ablation is mediated through a canonical pathway. It remains unclear as to which process mediates this activation in spite of the loss of the majority of colon-specific Notch ligands, especially as we observe a paradoxical increase in activated Notch1. We noted a precipitous decline in body weight of Reg4-ablated mice treated with DBZ, suggesting that there are systemic redundancies between Reg4-expressing cells and Notch signaling within the mouse, although the colonic mucosa remains competent for proliferation. Within the colon, there was one notable change with respect to the localization of proliferation along the crypt axis. Normally the crypt base is the site of peak proliferation, as seen in homeostasis and Reg4-ablation. However, Notch-inhibited Reg4-ablated crypts have proliferation at the mid-crypt region and this may implicate Notch signaling as a component of crypt axis regulation. In summary, our data demonstrate the Reg4-ablation model as a novel model for the exploration of epithelial-mesenchymal signaling and Notch dysregulation.

Materials and Methods

Table 4.1. Key Resources

Designation	Source or reference	Identifiers	Additional information
Genetic reagents (*Mus musculus*)			
C57BL/6J	The Jackson Laboratory	Cat# JAX: 000664, RRID:IMSR_JAX:000664	
$Reg4^{tm1(HBEGF/DsRed)Cle}$/J, $Reg4^{DTR-Red}$	The Jackson Laboratory	Cat# JAX: 029705, RRID:IMSR_JAX:029705	
Antibodies			
Rat monoclonal anti-Ki67	Thermo Fisher Scientific	Cat# 14-5698-82, RRID:AB_10854564	IHC-F (1:100)‡
Goat polyclonal anti-Lrig1	R&D Systems	Cat# AF3688, RRID:AB_2138836	WB (1:1000)* IHC-F (1:500)‡
Rabbit polyclonal anti-EGFR (phosphoY1068)	Abcam	Cat# ab5644, RRID:AB_305012	WB (1:2000)*
Rabbit monoclonal anti-EGFR	Abcam	Cat# ab52894, RRID:AB_869579	WB (1:2000)†
Rabbit polyclonal anti-ERK1/2	Bioss	Cat# bs-0022R, RRID:AB_10855763	WB (1:2000)*
Rabbit monoclonal anti-ERK1/2 (phospho p44/42)	Cell Signaling Technology	Cat# 4370, RRID:AB_2315112	WB (1:2000)†
Rat monoclonal anti-F4/80	eBioscience	Cat# 14-4801-85	IHC-F (1:500)‡
Mouse anti-Smooth Muscle Actin (α-SMA)	Agilent	Cat# M0851, RRID:AB_2223500	WB (1:1000)* IHC-F (1:500)‡
Rabbit monoclonal anti-non-phospho (Active) β-Catenin (Ser45)	Cell Signaling Technology	Cat# 19807, RRID:AB_2650576	WB (1:2000)†
Rabbit monoclonal anti-Notch1	Cell Signaling Technology	Cat# 3608, RRID:AB_2153354	WB (1:1000)* IHC-F (1:400)‡

Table 4.1 (Continued)

Designation	Source or reference	Identifiers	Additional information
Antibodies (continued)			
Rabbit monoclonal anti-Cleaved Notch1 (Val1744)	Cell Signaling Technology	Cat# 4147, RRID:AB_2153348	WB (1:1000)†
Rabbit monoclonal anti-GAPDH	Cell Signaling Technology	Cat# 2118, RRID:AB_561053	WB (1:10000)*
Sheep polyclonal anti-Dll1	R&D Systems	Cat# AF5026, RRID:AB_2092830	IHC-F (1:250)‡
Goat polyclonal anti-Dll4	R&D Systems	Cat# AF1389, RRID:AB_354770	IHC-F (1:400)§
Rabbit monoclonal anti-cMyc	Cell Signaling Technology	Cat# 5605, RRID:AB_1903938	IHC-F (1:500)‡
Sequence-based reagents			
RNAscope® Probe- Mm-Lgr5	Advanced Cell Diagnostics	Cat# 312171	
Actin qRT-PCR primers	This paper		(fp) TACCACCATGTACCCAGGCA; (rp) CTCAGGAGGAGCAATGATCTTGAT
Lrig1 qRT-PCR primers	This paper		(fp) CACAGTGGCTCTGCTGTATG; (rp) CAGTCCCACTGTAAGGATGG
Lgr5 qRT-PCR primers	This paper		(fp) GGAAGCGCTACAGAATTTGA; (rp) AGGCGTAGTCTGCTATGTGG
Egfr qRT-PCR primers	This paper		(fp) GTGATGGGGATGTGATCATT; (rp) AGCATAAAGGATTGCAGACG
Hes1 qRT-PCR primers	PrimerBank	PrimerBank ID: 6680205a1	(fp) CCAGCCAGTGTCAACACGA; (rp) AATGCCGGGAGCTATCTTTCT
Dll1 qRT-PCR primers	PrimerBank	PrimerBank ID: 6681197a1	(fp) CAGGACCTTCTTTCGCGTATG; (rp) ACTGCCGCTATTCTTGTCCC
Dll4 qRT-PCR primers	PrimerBank	PrimerBank ID: 9506547a1	(fp) TTCCAGGCAACCTTCTCCGA; (rp) ACTGCCGCTATTCTTGTCCC
Spdef2/3 qRT-PCR primers	This paper		(fp) TTGGATGAGCACTCGCTAGA; (rp) AGCCGGTACTGGTGTTCTGT
Muc2 qRT-PCR primers	This paper		(fp) GGTCCAGGGTCTGGATCACA; (rp) GCTCAGCTCACTGCCATCTG
Commercial assays and kits			
Pierce™ BCA Protein Assay Kit	Thermo Fisher Scientific	Cat# 23227	
PVDF Transfer Membrane, 0.45 μm	Thermo Fisher Scientific	Cat# 88518	
RNeasy Plus Mini Kit	Qiagen	Cat# 74134	
Maxima H Minus First Strand cDNA Synthesis Kit	Thermo Fisher Scientific	Cat# K1651	
PowerUp SYBR Green Master Mix	Applied Biosystems	Cat# A25742	
RNAscope® Multiplex Fluorescent Reagent Kit v2	Advanced Cell Diagnostics	Cat# 323100	
Chemical compounds and drugs			
Diphtheria Toxin from *Corynebacterium diphtheriae*	Millipore Sigma	Cat# D0564	
Pierce® RIPA buffer	Thermo Fisher Scientific	Cat# 89900	
Pierce™ Protease Inhibitor Mini Tablets, EDTA-free	Thermo Fisher Scientific	Cat# A32955	
PhosSTOP™	Roche	Cat# 4906845001	
γ-Secretase Inhibitor XX Dibenzazepine; DBZ	BioVision	Cat# 2649, CAS# 209984-56-5	
5-Ethynyl-2′-deoxyuridine; EdU	Sigma Aldrich	Cat# 900584	
Dextran Sulfate Sodium	Sigma Aldrich	Cat# D8906	

Table 4.1 (Continued)

Designation	Source or reference	Identifiers	Additional information
Chemical compounds and drugs (continued)			
Blocking Buffer, 5% Nonfat dry milk, 0.1% Tween-20, Tris-Buffered Saline	This paper		* Use as blocking buffer/antibody diluent indicated for selected antibody applications
Blocking Buffer, 5% Bovine Serum Albumen, 0.3% Triton X-100, 1mM CaCl2 in Phosphate-Buffered Saline	This paper		‡ Use as blocking buffer/antibody diluent indicated for selected antibody applications
Blocking Buffer, 5% Bovine Serum Albumen, 0.1% Tween-20, Tris-Buffered Saline	This paper		† Use as blocking buffer/antibody diluent indicated for selected antibody applications
Dako Antibody Diluent, Background Reducing	Agilent	Cat# S302283-2	§ Use as antibody diluent indicated for selected antibody applications
Dako Protein Block, Serum-Free	Agilent	Cat# X090930-2	§ Use as blocking buffer indicated for selected antibody applications
DAPI	VWR	Cat# 89139-054	1 µg/mL PBS
Software and algorithms			
Fiji/ImageJ	PMID: 22743772	RRID:SCR_002285	
CryptCount	https://github.com/twheele3/ccproc		An R package that translates user-made image annotations of crypts to processable count formats.
R; RStudio	R Project for Statistical Computing; RStudio	RRID:SCR_001905; RRID:SCR_000432	
Image Studio Lite	LI-COR	RRID:SCR_013715	
Zen	Zeiss	RRID:SCR_013672	
NIS-Elements	Nikon	RRID:SCR_014329	

Mice

C57BL/6 (Jackson Laboratory (Jax), Bar Harbor, ME, USA) and Reg4-dsRed-DTR (Jax) mice were housed in a specific pathogen-free environment under strictly controlled light cycle conditions, fed a standard rodent lab chow and provided water ad libitum. Mice were sacrificed at 8-10 weeks of age by direct cervical dislocation. **Reg4-ablation**. Reg4-dsRed-DTR mice were administered Diphtheria toxin (CalBiochem, Billerica, MA, USA) at 50µg/kg body weight in 0.2mL PBS vehicle daily via intraperitoneal (IP) injection for 1-6 days of treatment, and were sacrificed 24 hours after last injection. Reg4-dsRed-DTR or C57BL/6 mice were administered 0.2mL PBS vehicle by IP injection for 4 days as a control group. Notch inhibition. Mice were administered γ-Secretase Inhibitor XX Dibenzazepine (DBZ) (BioVision #2649) at 10µmol/kg body weight (vehicle 0.5% (w/v) hydroxypropylmethyl cellulose, 0.1% (v/v) Tween-80, ddH_2O) daily by IP injection for two days prior to sacrifice. 5-ethynyl-2'-deoxyuridine (EdU) tracing. Mice were treated with 2mg EdU (Sigma-Aldrich, St. Louis, MO, USA) in 0.2mL DMSO/PBS vehicle by IP injection 2 hours prior to sacrifice. Treatment with dextran sodium sulfate (DSS). DSS (Sigma-Aldrich) was dissolved in filtered drinking water and supplied ad libitum to C57Bl/6 mice for 7 days. Drinking water was switched to normal water on Day 8, then mice were sacrificed on Day 11 and colons were dissected for histology. All procedures were approved and performed in accordance with the policies of the University of Oregon Institutional Animal Care and Use Committee.

Histology

Colons dissected from mice were flushed with ice-cold PBS, flayed, and pinned flat, then fixed in 4% PFA/PBS for 60 minutes at room temperature with light oscillation. Fixed colons were washed 3x5 minutes in PBS and incubated in 30% sucrose overnight at 4°C, then blocked in OCT. 15 μm sections were taken on Superfrost™ Plus Slides (Fisher, Pittsburgh, PA, USA). **Immunohistochemistry.** Slides were washed 3x3 minutes in PBS and blocked for 1 hour at room temperature in blocking buffer, then overnight at 4°C with primary antibody diluted in staining buffer. Slides were washed 3x3 minutes in PBS then stained with secondary antibody diluted in blocking buffer. Slides were washed 3x3 minutes in PBS, counterstained with DAPI, and mounted with N-propyl gallate mounting medium. Slides were imaged via confocal microscopy using a Zeiss LSM-880 (Zeiss, Oberkochen, Germany) system for morphimetry, or a Nikon Eclipse/Ds-Ri2 (Nikon, Tokyo, Japan) for mean intensity analysis. ***In-situ*** hybridization. Sections were labeled for *Lgr5* using RNAscope® Probe- Mm-Lgr5 (Advanced Cell Diagnostics (ACD), Newark, CA, USA) using RNAscope® Multiplex Fluorescent Reagent Kit v2 (ACD) as per manufacturer recommended protocol for fixed frozen sample (ACD TN 320535 Rev A, 323100-USM). In brief, slides were washed briefly in 1xPBS then boiled for 5 minutes in 1x Target Retrieval buffer, followed by two brief washes in ddH2O then once in 95% EtOH. Slides were dried then dammed with an ImmEdge hydrophobic barrier pen, then incubated with Protease III for 15 minutes at 40°C. Slides were washed briefly in ddH2O, then incubated at 40°C in sequence with Probe-Mm-Lgr5 (2 hours), AMP 1 (30 minutes), AMP 2 (30 minutes), AMP 3 (15 minutes), HRP-C1 (15 minutes), Opal-650 (1:2000 in TSA buffer) (30 minutes), with 2x2 minute washes with 1x Wash Buffer between hybridization steps. Slides were counterstained with DAPI and mounted with N-propyl gallate mounting medium. Slides were imaged via confocal microscopy using a Zeiss LSM-880 system.

Mucosal Tissue Isolation

Samples of isolated mucosal tissue were prepared from mice treated with either DT or vehicle daily for 3 days. The distal half of the colon was dissected out, flushed, flayed, and cut into 1-cm pieces and placed in 1 mM EDTA/5 mM DTT/PBS to incubate for 40 minutes on ice with gentle oscillation. Supernatant was decanted and replaced with 30mM EDTA/PBS, and the samples were incubated for 8 minutes at 37C with gentle agitation every 2 minutes. Supernatant was decanted and replaced with ice-cold PBS, and mucosal tissue was dissociated from muscle tissue by hand agitation (shaking at approx. 120 beats per minute for 1 minute intervals) until there were no apparent changes in turbidity. Visible muscle tissue was removed and dissociated mucosal tissue was pelleted at 1000xRCF at 4°C.

Western Blot

Isolated mucosal tissue was digested with 300uL Pierce® RIPA buffer (ThermoFisher, Waltham, MA, USA) treated with Pierce™ Protease Inhibitor Mini Tablets, EDTA-free (Thermo) and PhosSTOP™ (Roche, Basel, Switzerland) by syringing repeatedly through a 22-ga needle. Suspension was then centrifuged at for 5 minutes at 5000xRCF, then 5 minutes at 14000xRCF to clarify supernatant. Protein content was measured by BCA assay (ThermoFisher) to load 25µg of protein per western blot lane. Western blots were run with freshly prepared 10% acrylamide gels at 125 V and transferred to 0.45µm-pore PVDF membranes (ThermoFisher) at 55 V for 18 hours on ice. Membranes were dried, washed briefly with TBST, then blocked with specified blocking buffer for 1hr RT and incubated overnight with primary antibody diluted in blocking buffer at 4°C with light oscillation. Membranes were washed 3x3 minutes in TBST, then incubated for 1 hour in HRP-conjugated secondary antibody diluted in blocking buffer. Membranes were washed 3x3 minutes in TBST, then incubated for 5 minutes with Cytiva Amersham™ ECL™ Prime Western Blotting Detection Reagent (Cytiva, Marlsborough, MA, USA) prior to imaging for chemifluorescence on a LI-COR Odyssey Fc Imaging System (LI-COR, Lincoln, NE, USA). Membranes were stripped and restained up to 3 times, washing 2x10 minutes with mild stripping buffer (1.5% glycine, 0.1% SDS, 1% Tween-20, pH 2.2 in PBS), then 2x10 minutes with PBS and 2x5 minutes with TBST before re-blocking. Antibody and blocking conditions are described in Key Resources Table. Protein fold change was calculated versus vehicle by batch correcting based on vehicle response between membranes, normalizing to GAPDH expression as a loading control, then normalizing to vehicle mean.

qRT-PCR

Total RNA was isolated from mucosal tissue pellets using RNeasy Plus Mini Kit (Qiagen, Hilden, Germany). First strand cDNA was synthesized using 2 μg of total RNA using Maxima H Minus Kit according to manufacturer instructions (ThermoFisher). qRT-PCR was performed using PowerUp SYBR Green Master Mix (Applied Biosystems, Waltham, MA, USA) according to the manufacturer's recommendations, and run using a Bio-Rad CFX96 Real-Time System (Bio-Rad, Hercules, CA, USA). Each target was run with three technical replicates per sample. The relative target gene mRNA levels were normalized to actin expression. Primers used are listed in Key Rescources Table.

Statistical analysis

Statistical analysis was performed using R. Morphometric data of blinded fluorescent images were hand annotated for crypts in Fiji (Schindelin et al., 2012) and processed in R for crypt structure using lab-produced software CryptCount (https://github.com/twheele3/ccproc). **Biological replicates** consisted of individual mice per treatment condition (n = 2-5 for immunofluorescence and *in situ* hybridization, 5-8 for WB and qRT-PCR). 15-30 well-formed crypts (visible in cross-section from muscularis mucosa to lumen) were counted per marker per mouse, and tested by Tukey test using crypts as random effect. WB and qRT-PCR were analyzed by unpaired two-tailed Student's t-test.

CHAPTER V

CONCLUSIONS AND FUTURE DIRECTIONS

In this dissertation I have presented a framework for mechanistic analysis of the epithelial niche, created an atlas of many significant immunohistology markers within that niche, and identified a novel experimental application for support cell ablation that can further our understanding of how this epithelial system functions. In all aspects of my research, I have laid the groundwork for the success of future study of this system, from creating analytical tools to summarizing the state of this model to opening novel and significant avenues of inquiry.

In Chapter 2, I presented an argument for a higher standard of data collection with respect to crypts, and a method for acquiring data to this standard with little increase in effort over traditional data collection methods in the field of crypt biology. This approach represents an important move forward for analysis of crypts. While most of the analyses used with this data in this dissertation are considered field-standard, the approaches to collecting this data are usually done with the specific format of the result in mind. This creates a great amount of inflexibility in data analysis, as any recontextualization of results usually requires re-analysis of image data. For instance, if I set out with the goal of quantifying goblet cells, I might start by counting all visible instances per mucosal area or per crypt. If I later realized that there seemed to be a strong positional bias toward the base of crypts, I would have to go back and re-analyze my images to include positional information, effectively redoing all my previous work. With this algorithm-based method, I only have to annotate the image file once, and can then pull out and aggregate my data with respect to position within the crypt as well as relative to the crypt itself. Another aspect of this sort of flexible data collection is to set up for future success. The algorithm I created collects a significant amount of geometric metadata in addition to its primary job of structuring data in a connected network model. It may be difficult to predict how and when this may be of use, but as demonstrated by my aggregate statistics (Figure 3.1), the data is in a format that may allow for creative and novel analyses that I did not anticipate when creating these tools.

In Chapter 3, I presented an extensive set of histological data characterizing the murine distal colonic epithelium. This presents an atlas of control data that can be useful for any crypt biologist designing an experimental cohort. While any experimentation would need its own control set of data to control for myriad factors including histological and technical variance in counting, it provides a general statistical framework to set expectations of cell type frequencies and certain interesting and probable pathways within the crypt. This established set of prior data could be used for power analysis, which while an essential component of other smaller organismal models, tends to be underutilized in mouse sciences due to the relative difficulty in acquiring biological replicates, especially in the case of multi-transgenic cross breedings. One additional factor adding value to this atlas: It is rare for a breadth of relevant markers to be presented in a unified format, acquired using roughly equivalent parameters and techniques. This gives a stronger point of reference when comparing disparate markers than by stitching together separate data points aggregated by different biologists from literature. A final point of importance is that this data is taken from colonic crypts. Despite extensive work in colorectal cancer biology, there has been a paucity of characteristic data for colonic crypt homeostasis. Most literature on crypt homeostasis is taken with respect to the small intestine, with occasional inclusions of colonic crypt data. Yet small intestinal crypt dynamics are significantly different from colonic crypts, despite their strong overlap in underlying pathways (Almet et al., 2020; McCarthy et al., 2020). Therefore, the work I present here can be considered novel for the purpose of providing a broad amount of primary characterization data for colonic crypts, to an extent typically seen only in secondary literature.

In Chapter 4, I presented experimental data characterizing the crypt and mucosal response to the ablation of Reg4+ support cells. Over the course of these experiments, I made several novel observations, including a transient hyperproliferative state, an unexpected increase in Notch signaling, and remodeling of mesenchymal cell populations. My observations of transient hyperproliferation represent novel insights in two regards. Firstly, my observation of ablation-induced hyperproliferation marks a divergence from other crypt ablation models using DTR transgenic mice (Castillo-Azofeifa et al., 2019; Tian et al., 2011; van Es et al., 2019), indicating that this phenotype is occurring specifically due to the ablation of Reg4-lineage cells. Secondly, my data is presented in a time course with a novel degree of resolution, showing a clearly resolved peak and subsequent reduction (Figure 4.2), whereby contrast most crypt studies that use an effector molecule will fixate on a single timepoint to contrast with their control, similar to my later EdU trace targeting the peak of hyperproliferation (Figure 4.3). By presenting data from the time course between the start of Reg4-ablation and the loss of *Lgr5*+ cells, I show an added dimension of the nuances involved in shifting crypt dynamics after specific perturbations. This does come with a caveat that this manner of time course overview is most applicable when the effector is rapid, complete, and systemic with its penetrance. This has been demonstrated in the case of diphtheria toxin for this application relative to the resolution of my time course (Holmes, 2000; Sasaki et al., 2016), otherwise, any observed dynamics may be due to the gradualness in shift to an affected state. The increase in cleaved Notch that I observed (Figure 4.5A) represents a paradoxical activation that I have been unable to account for. Despite the fact that it seems to be dispensable to the proliferative phenotype (Figure 4.9), it still represents a novel observation that has potential to yield insights into noncanonical Notch signaling initiation, as my probes for Notch ligands suggest that this should not occur by an extrinsic ligand-binding route of activation (Figure 4.5B,C). This may prove to be of clinical significance, as intrinsic activation of Notch signaling has been linked to tumorigenesis (Fazio & Ricciardiello, 2016; Y. Zhao et al., 2016). Finally, my observations on mesenchymal remodeling yield another novel axis of experimental potential (Figure 4.10). Epithelial-mesenchymal communication is well understood to be a critical component of crypt maintenance (Brügger et al., 2020; Cotton et al., 2017; Stzepourginski et al., 2017), but the bulk of this knowledge is in the mesenchymal-to-epithelial signaling direction. Less understood is how epithelial cells may influence the mesenchyme, especially post-development when mesenchymal remodeling can be linked to chronic disease states characterized by fibrosis (Speca et al., 2012; Usunier et al., 2021; S. Zhao et al., 2020). My data identifies Reg4-ablation as a strong candidate model for probing the epithelial-to-mesenchymal signaling axis, as Reg4-ablation in the colon is specific to a portion of the epithelial secretory lineage and causes remodeling in mesenchymal myofibroblasts and stromal cells. This provides an avenue to experimentally probe mechanisms that drive this remodeling, and therefore potentially uncover specific molecular mechanisms of how the epithelium may modulate the mesenchyme. This could uncover new mechanistic bases for treatment and prevention of fibrosis as well as potentially unveiling other underlying causes for chronic bowel syndromes that could be linked to mesenchymal remodeling.

In conclusion, this dissertation has addressed several outstanding questions or issues within the field of murine crypt biology by describing tools to enhance statistical rigor within the field, presenting a novel atlas of the colonic crypt, and experimentally describing several significant phenotypes with respect to Reg4-ablation, all of which leave promising starting points for the future studies exploring the molecular underpinnings of cell division, movement, differentiation and death in colonic crypt.

APPENDICES

ABBREVIATIONS

αSMA – alpha Smooth Muscle Actin

DBZ - γ-Secretase Inhibitor XX Dibenzazepine

DSS – dextran sodium sulfate

DT – diphtheria toxin

DTR – diphtheria toxin receptor

DTT - dithiothreitol

EDTA - ethylenediaminetetraacetic acid

EdU – 5-ethynyl-2’-deoxyuridine

FISH – fluorescence in situ hybridization

IEC – intestinal epithelial cell

NICD – Notch1 intracellular domain

NTM – Notch1 transmembrane domain

OCT – Optimal Cutting Temperature compound

PBS - phosphate-buffered saline solution

PFA - paraformaldehyde

qRT-PCR – quantitative real-time PCR

RT - room temperature

TA – transit amplifying

TBST - Tris-buffered saline with 0.1% Tween-20

Veh – vehicle

WB – Western blot

REFERENCES CITED

Adamatzky, A. (2013). On growing connected β -skeletons. *Computational Geometry*, *46*(6), 805–816. https://doi.org/10.1016/j.comgeo.2012.11.009

Almet, A. A., Maini, P. K., Moulton, D. E., & Byrne, H. M. (2020). Modeling perspectives on the intestinal crypt, a canonical system for growth, mechanics, and remodeling. *Current Opinion in Biomedical Engineering*, *15*, 32–39. https://doi.org/10.1016/j.cobme.2019.12.012

Barker, N., van Es, J. H., Kuipers, J., Kujala, P., van den Born, M., Cozijnsen, M., Haegebarth, A., Korving, J., Begthel, H., Peters, P. J., & Clevers, H. (2007). Identification of stem cells in small intestine and colon by marker gene Lgr5. *Nature*, *449*(7165), 1003–1007. https://doi.org/10.1038/nature06196

Bohin, N., Keeley, T. M., Carulli, A. J., Walker, E. M., Carlson, E. A., Gao, J., Aifantis, I., Siebel, C. W., Rajala, M. W., Myers, M. G., Jones, J. C., Brindley, C. D., Dempsey, P. J., & Samuelson, L. C. (2020). Rapid Crypt Cell Remodeling Regenerates the Intestinal Stem Cell Niche after Notch Inhibition. *Stem Cell Reports*, *15*(1), 156–170. https://doi.org/10.1016/j.stemcr.2020.05.010

Bonis, V., Rossell, C., & Gehart, H. (2021). The Intestinal Epithelium – Fluid Fate and Rigid Structure From Crypt Bottom to Villus Tip. *Frontiers in Cell and Developmental Biology*, *9*. https://doi.org/10.3389/fcell.2021.661931

Bray, S. J. (2016). Notch signalling in context. *Nature Reviews Molecular Cell Biology*, *17*(11), 722–735. https://doi.org/10.1038/nrm.2016.94

Brentnall, M., Rodriguez-Menocal, L., De Guevara, R. L., Cepero, E., & Boise, L. H. (2013). Caspase-9, caspase-3 and caspase-7 have distinct roles during intrinsic apoptosis. *BMC Cell Biology*, *14*(1), 32. https://doi.org/10.1186/1471-2121-14-32

Brügger, M. D., Valenta, T., Fazilaty, H., Hausmann, G., & Basler, K. (2020). Distinct populations of crypt-associated fibroblasts act as signaling hubs to control colon homeostasis. *PLOS Biology*, *18*(12), e3001032. https://doi.org/10.1371/journal.pbio.3001032

Castillo-Azofeifa, D., Fazio, E. N., Nattiv, R., Good, H. J., Wald, T., Pest, M. A., Sauvage, F. J., Klein, O. D., & Asfaha, S. (2019). Atoh1 + secretory progenitors possess renewal capacity independent of Lgr5 + cells during colonic regeneration. *The EMBO Journal*, *38*(4). https://doi.org/10.15252/embj.201899984

Chacón-Martínez, C. A., Koester, J., & Wickström, S. A. (2018). Signaling in the stem cell niche: regulating cell fate, function and plasticity. *Development*, *145*(15). https://doi.org/10.1242/dev.165399

Chen, L., Deng, H., Cui, H., Fang, J., Zuo, Z., Deng, J., Li, Y., Wang, X., & Zhao, L. (2018). Inflammatory responses and inflammation-associated diseases in organs. *Oncotarget*, *9*(6), 7204–7218. https://doi.org/10.18632/oncotarget.23208

Chen, Z., Downing, S., & Tzanakakis, E. S. (2019). Four Decades After the Discovery of Regenerating Islet-Derived (Reg) Proteins: Current Understanding and Challenges. *Frontiers in Cell and Developmental Biology*, *7*. https://doi.org/10.3389/fcell.2019.00235

Cotton, J. L., Li, Q., Ma, L., Park, J. S., Wang, J., Ou, J., Zhu, L. J., Ip, Y. T., Johnson, R. L., & Mao, J. (2017). YAP/TAZ and Hedgehog coordinate growth and patterning in gastrointestinal mesenchyme. *Developmental Cell*, *43*(1), 35. https://doi.org/10.1016/J.DEVCEL.2017.08.019

Dahlhamer, J. M., Zammitti, E. P., Ward, B. W., Wheaton, A. G., & Croft, J. B. (2016). Prevalence of Inflammatory Bowel Disease Among Adults Aged ≥18 Years — United States, 2015. *MMWR. Morbidity and Mortality Weekly Report*, *65*(42), 1166–1169. https://doi.org/10.15585/mmwr.mm6542a3

David, M. B., Valenta, T., Fazilaty, H., Hausmann, G., & Basler, K. (2020). Distinct populations of crypt-associated fibroblasts act as signaling hubs to control colon homeostasis. *PLoS Biology*, *18*(12). https://doi.org/10.1371/journal.pbio.3001032

Davies, P. S., Powell, A. E., Swain, J. R., & Wong, M. H. (2009). Inflammation and Proliferation Act Together to Mediate Intestinal Cell Fusion. *PLoS ONE*, *4*(8), e6530. https://doi.org/10.1371/journal.pone.0006530

Degirmenci, B., Valenta, T., Dimitrieva, S., Hausmann, G., & Basler, K. (2018). GLI1-expressing mesenchymal cells form the essential Wnt-secreting niche for colon stem cells. *Nature*, *558*(7710), 449–453. https://doi.org/10.1038/s41586-018-0190-3

Droy-Dupré, L., Vallée, M., Bossard, C., Laboisse, C. L., & Jarry, A. (2012). A multiparametric approach to monitor the effects of γ-secretase inhibition along the whole intestinal tract. *Disease Models & Mechanisms*, *5*(1), 107–114. https://doi.org/10.1242/dmm.007591

Dubé, P. E., Liu, C. Y., Girish, N., Washington, M. K., & Polk, D. B. (2018). Pharmacological activation of epidermal growth factor receptor signaling inhibits colitis-associated cancer in mice. *Scientific Reports*, *8*(1), 9119. https://doi.org/10.1038/s41598-018-27353-w

Eichele, D. D., & Kharbanda, K. K. (2017). Dextran sodium sulfate colitis murine model: An indispensable tool for advancing our understanding of inflammatory bowel diseases pathogenesis. *World Journal of Gastroenterology*, *23*(33), 6016–6029. https://doi.org/10.3748/wjg.v23.i33.6016

Fazio, C., & Ricciardiello, L. (2016). Inflammation and Notch signaling: a crosstalk with opposite effects on tumorigenesis. *Cell Death & Disease*, *7*(12), e2515–e2515. https://doi.org/10.1038/cddis.2016.408

Gerbe, F., Legraverend, C., & Jay, P. (2012). The intestinal epithelium tuft cells: specification and function. *Cellular and Molecular Life Sciences*, *69*(17), 2907–2917. https://doi.org/10.1007/s00018-012-0984-7

Grainger, S., & Willert, K. (2018). Mechanisms of Wnt signaling and control. *Wiley Interdisciplinary Reviews: Systems Biology and Medicine*, *10*(5), e1422. https://doi.org/10.1002/wsbm.1422

Gregorio, J. Di, Sferra, R., Speca, S., Vetuschi, A., Dubuquoy, C., Desreumaux, P., Pompili, S., Cristiano, L., Gaudio, E., Flati, V., & Latella, G. (2017). Role of glycogen synthase kinase-3β and PPAR-γ on epithelial-to-mesenchymal transition in DSS-induced colorectal fibrosis. *PLoS ONE*, *12*(2). https://doi.org/10.1371/JOURNAL.PONE.0171093

Hans, F., & Dimitrov, S. (2001). Histone H3 phosphorylation and cell division. *Oncogene*, *20*(24), 3021–3027. https://doi.org/10.1038/sj.onc.1204326

Harnack, C., Berger, H., Antanaviciute, A., Vidal, R., Sauer, S., Simmons, A., Meyer, T. F., & Sigal, M. (2019). R-spondin 3 promotes stem cell recovery and epithelial regeneration in the colon. *Nature Communications*, *10*(1). https://doi.org/10.1038/s41467-019-12349-5

Holmes, R. K. (2000). Biology and Molecular Epidemiology of Diphtheria Toxin and the tox Gene. *The Journal of Infectious Diseases*, *181*(s1), S156–S167. https://doi.org/10.1086/315554

Ingham-Dempster, T., Walker, D. C., & Corfe, B. M. (2017). An agent-based model of anoikis in the colon crypt displays novel emergent behaviour consistent with biological observations. *Royal Society Open Science*, *4*(4), 160858. https://doi.org/10.1098/rsos.160858

Jones, G.-R., Bain, C. C., Fenton, T. M., Kelly, A., Brown, S. L., Ivens, A. C., Travis, M. A., Cook, P. C., & MacDonald, A. S. (2018). Dynamics of Colon Monocyte and Macrophage Activation During Colitis. *Frontiers in Immunology*, *9*. https://doi.org/10.3389/fimmu.2018.02764

Kagawa, Y., Horita, N., Taniguchi, H., & Tsuneda, S. (2014). Modeling of stem cell dynamics in human colonic crypts in silico. *Journal of Gastroenterology*, *49*(2), 263–269. https://doi.org/10.1007/s00535-013-0887-x

Kiesler, P., Fuss, I. J., & Strober, W. (2015). Experimental Models of Inflammatory Bowel Diseases. *Cellular and Molecular Gastroenterology and Hepatology*, *1*(2), 154–170. https://doi.org/10.1016/j.jcmgh.2015.01.006

Kim, E., Davidson, L. A., Zoh, R. S., Hensel, M. E., Patil, B. S., Jayaprakasha, G. K., Callaway, E. S., Allred, C. D., Turner, N. D., Weeks, B. R., & Chapkin, R. S. (2016). Homeostatic responses of colonic LGR5+ stem cells following acute in vivo exposure to a genotoxic carcinogen. *Carcinogenesis*, *37*(2), 206–214. https://doi.org/10.1093/carcin/bgv250

Kim, T.-H., Saadatpour, A., Guo, G., Saxena, M., Cavazza, A., Desai, N., Jadhav, U., Jiang, L., Rivera, M. N., Orkin, S. H., Yuan, G.-C., & Shivdasani, R. A. (2016). Single-Cell Transcript Profiles Reveal Multilineage Priming in Early Progenitors Derived from Lgr5 + Intestinal Stem Cells. *Cell Reports*, *16*(8), 2053–2060. https://doi.org/10.1016/j.celrep.2016.07.056

King, J. B., von Furstenberg, R. J., Smith, B. J., McNaughton, K. K., Galanko, J. A., & Henning, S. J. (2012). CD24 can be used to isolate Lgr5+ putative colonic epithelial stem cells in mice. *American Journal of Physiology. Gastrointestinal and Liver Physiology*, *303*(4), G443-52. https://doi.org/10.1152/ajpgi.00087.2012

Langlands, A. J., Almet, A. A., Appleton, P. L., Newton, I. P., Osborne, J. M., & Näthke, I. S. (2016). Paneth Cell-Rich Regions Separated by a Cluster of Lgr5+ Cells Initiate Crypt Fission in the Intestinal Stem Cell Niche. *PLoS Biology*, *14*(6). https://doi.org/10.1371/journal.pbio.1002491

Leung, C., Tan, S. H., & Barker, N. (2018). Recent Advances in Lgr5 + Stem Cell Research. *Trends in Cell Biology*, *28*(5), 380–391. https://doi.org/10.1016/j.tcb.2018.01.010

Liang, S., Li, X., & Wang, X. (2019). Notch Signaling in Mammalian Intestinal Stem Cells: Determining Cell Fate and Maintaining Homeostasis. *Current Stem Cell Research & Therapy*, *14*(7), 583–590. https://doi.org/10.2174/1574888X14666190429143734

Lo, Y. H., Chung, E., Li, Z., Wan, Y. W., Mahe, M. M., Chen, M. S., Noah, T. K., Bell, K. N., Yalamanchili, H. K., Klisch, T. J., Liu, Z., Park, J. S., & Shroyer, N. F. (2017). Transcriptional Regulation by ATOH1 and its Target SPDEF in the Intestine. *CMGH*, *3*(1), 51–71. https://doi.org/10.1016/j.jcmgh.2016.10.001

Madison, B. B., Dunbar, L., Qiao, X. T., Braunstein, K., Braunstein, E., & Gumucio, D. L. (2002). cis Elements of the Villin Gene Control Expression in Restricted Domains of the Vertical (Crypt) and Horizontal (Duodenum, Cecum) Axes of the Intestine. *Journal of Biological Chemistry*, *277*(36), 33275–33283. https://doi.org/10.1074/jbc.M204935200

McCarthy, N., Kraiczy, J., & Shivdasani, R. A. (2020). Cellular and molecular architecture of the intestinal stem cell niche. *Nature Cell Biology*, *22*(9), 1033–1041. https://doi.org/10.1038/s41556-020-0567-z

Meineke, F. A., Potten, C. S., & Loeffler, M. (2001). Cell migration and organization in the intestinal crypt using a lattice-free model. *Cell Proliferation*, *34*(4), 253–266. https://doi.org/10.1046/j.0960-7722.2001.00216.x

Mellitzer, G., Beucher, A., Lobstein, V., Michel, P., Robine, S., Kedinger, M., & Gradwohl, G. (2010). Loss of enteroendocrine cells in mice alters lipid absorption and glucose homeostasis and impairs postnatal survival. *Journal of Clinical Investigation*, *120*(5), 1708–1721. https://doi.org/10.1172/JCI40794

Meran, L., Baulies, A., & Li, V. S. W. (2017). Intestinal Stem Cell Niche: The Extracellular Matrix and Cellular Components. *Stem Cells International*, *2017*, 1–11. https://doi.org/10.1155/2017/7970385

Mizoguchi, E., Low, D., Ezaki, Y., & Okada, T. (2020). Recent updates on the basic mechanisms and pathogenesis of inflammatory bowel diseases in experimental animal models. *Intestinal Research*, *18*(2), 151–167. https://doi.org/10.5217/ir.2019.09154

Noah, T. K., & Shroyer, N. F. (2013). Notch in the Intestine: Regulation of Homeostasis and Pathogenesis. *Http://Dx.Doi.Org/10.1146/Annurev-Physiol-030212-183741*, *75*, 263–288. https://doi.org/10.1146/ANNUREV-PHYSIOL-030212-183741

Novak, S., Drenjancevic, I., Vukovic, R., Kellermayer, Z., Cosic, A., Tolusic Levak, M., Balogh, P., Culo, F., & Mihalj, M. (2016). Anti-Inflammatory Effects of Hyperbaric Oxygenation during DSS-Induced Colitis in BALB/c Mice Include Changes in Gene Expression of *HIF-1* α , Proinflammatory Cytokines, and Antioxidative Enzymes. *Mediators of Inflammation*, *2016*, 1–19. https://doi.org/10.1155/2016/7141430

Nusse, R., & Clevers, H. (2017). Wnt/β-Catenin Signaling, Disease, and Emerging Therapeutic Modalities. *Cell*, *169*(6), 985–999. https://doi.org/10.1016/j.cell.2017.05.016

O'Leary, C. E., Schneider, C., & Locksley, R. M. (2019). Tuft Cells—Systemically Dispersed Sensory Epithelia Integrating Immune and Neural Circuitry. *Annual Review of Immunology*, *37*(1), 47–72. https://doi.org/10.1146/annurev-immunol-042718-041505

Otsuka, K., & Suzuki, K. (2016). Differences in Radiation Dose Response between Small and Large Intestinal Crypts. *Radiation Research*, *186*(3), 302–314. https://doi.org/10.1667/RR14455.1

Pellegrinet, L., Rodilla, V., Liu, Z., Chen, S., Koch, U., Espinosa, L., Kaestner, K. H., Kopan, R., Lewis, J., & Radtke, F. (2011). Dll1- and Dll4-mediated notch signaling are required for homeostasis of intestinal stem cells. *Gastroenterology*, *140*(4), 1230-1240.e7. https://doi.org/10.1053/j.gastro.2011.01.005

Perez White, B. E., & Getsios, S. (2014). Eph receptor and ephrin function in breast, gut, and skin epithelia. *Cell Adhesion & Migration*, *8*(4), 327–338. https://doi.org/10.4161/19336918.2014.970012

Potten, C. S. (1998). Stem cells in gastrointestinal epithelium: numbers, characteristics and death. *Philosophical Transactions of the Royal Society of London. Series B: Biological Sciences*, *353*(1370), 821–830. https://doi.org/10.1098/rstb.1998.0246

Poulin, E. J., Powell, A. E., Wang, Y., Li, Y., Franklin, J. L., & Coffey, R. J. (2014). Using a new Lrig1 reporter mouse to assess differences between two Lrig1 antibodies in the intestine. *Stem Cell Research*, *13*(3), 422–430. https://doi.org/10.1016/j.scr.2014.09.002

Powell, A. E., Wang, Y., Li, Y., Poulin, E. J., Means, A. L., Washington, M. K., Higginbotham, J. N., Juchheim, A., Prasad, N., Levy, S. E., Guo, Y., Shyr, Y., Aronow, B. J., Haigis, K. M., Franklin, J. L., & Coffey, R. J. (2012). The Pan-ErbB Negative Regulator Lrig1 Is an Intestinal Stem Cell Marker that Functions as a Tumor Suppressor. *Cell*, *149*(1), 146–158. https://doi.org/10.1016/j.cell.2012.02.042

Qin, T., Yang, J., Huang, D., Zhang, Z., Huang, Y., Chen, H., & Xu, G. (2021). DOCK4 stimulates MUC2 production through its effect on goblet cell differentiation. *Journal of Cellular Physiology*, *236*(9), 6507–6519. https://doi.org/10.1002/jcp.30325

Ramos-Vara, J. A., & Miller, M. A. (2014). When Tissue Antigens and Antibodies Get Along. *Veterinary Pathology*, *51*(1), 42–87. https://doi.org/10.1177/0300985813505879

Rindi, G., Leiter, A. B., Kopin, A. S., Bordi, C., & Solcia, E. (2004). The "normal" endocrine cell of the gut: Changing concepts and new evidences. *Annals of the New York Academy of Sciences*, *1014*(1), 1–12. https://doi.org/10.1196/annals.1294.001

Rothenberg, M. E., Nusse, Y., Kalisky, T., Lee, J. J., Dalerba, P., Scheeren, F., Lobo, N., Kulkarni, S., Sim, S., Qian, D., Beachy, P. A., Pasricha, P. J., Quake, S. R., & Clarke, M. F. (2012). Identification of a cKit+ colonic crypt base secretory cell that supports Lgr5+ stem cells in mice. *Gastroenterology*, *142*(5), 1195. https://doi.org/10.1053/j.gastro.2012.02.006

Sasaki, N., Sachs, N., Wiebrands, K., Ellenbroek, S. I. J., Fumagalli, A., Lyubimova, A., Begthel, H., van den Born, M., van Es, J. H., Karthaus, W. R., Li, V. S. W., López-Iglesias, C., Peters, P. J., van Rheenen, J., van Oudenaarden, A., & Clevers, H. (2016). Reg4 + deep crypt secretory cells function as epithelial niche for Lgr5 + stem cells in colon. *Proceedings of the National Academy of Sciences*, *113*(37), E5399–E5407. https://doi.org/10.1073/pnas.1607327113

Schindelin, J., Arganda-Carreras, I., Frise, E., Kaynig, V., Longair, M., Pietzsch, T., Preibisch, S., Rueden, C., Saalfeld, S., Schmid, B., Tinevez, J.-Y., White, D. J., Hartenstein, V., Eliceiri, K., Tomancak, P., & Cardona, A. (2012). Fiji: an open-source platform for biological-image analysis. *Nature Methods*, *9*(7), 676–682. https://doi.org/10.1038/nmeth.2019

Serrano Martinez, P., Giuranno, L., Vooijs, M., & Coppes, R. P. (2021). *The Radiation-Induced Regenerative Response of Adult Tissue-Specific Stem Cells: Models and Signaling Pathways*. https://doi.org/10.3390/cancers13040855

Shewchuk, J. R. (1996). *Triangle: Engineering a 2D quality mesh generator and Delaunay triangulator* (pp. 203–222). https://doi.org/10.1007/BFb0014497

Shimizu, H., Okamoto, R., Ito, G., Fujii, S., Nakata, T., Suzuki, K., Murano, T., Mizutani, T., Tsuchiya, K., Nakamura, T., Hozumi, K., & Watanabe, M. (2014). Distinct expression patterns of Notch ligands, Dll1 and Dll4, in normal and inflamed mice intestine. *PeerJ*, *2*(1), e370. https://doi.org/10.7717/peerj.370

Shinoda, M., Shin-Ya, M., Naito, Y., Kishida, T., Ito, R., Suzuki, N., Yasuda, H., Sakagami, J., Imanishi, J., Kataoka, K., Mazda, O., & Yoshikawa, T. (2010). Early-stage blocking of Notch signaling inhibits the depletion of goblet cells in dextran sodium sulfate-induced colitis in mice. *Journal of Gastroenterology*, *45*(6), 608–617. https://doi.org/10.1007/s00535-010-0210-z

Snippert, H. J., van der Flier, L. G., Sato, T., van Es, J. H., van den Born, M., Kroon-Veenboer, C., Barker, N., Klein, A. M., van Rheenen, J., Simons, B. D., & Clevers, H. (2010). Intestinal Crypt Homeostasis Results from Neutral Competition between Symmetrically Dividing Lgr5 Stem Cells. *Cell*, *143*(1), 134–144. https://doi.org/10.1016/j.cell.2010.09.016

Speca, S. (2012). Cellular and molecular mechanisms of intestinal fibrosis. *World Journal of Gastroenterology*, *18*(28), 3635. https://doi.org/10.3748/wjg.v18.i28.3635

Speca, S., Giusti, I., Rieder, F., & Latella, G. (2012). Cellular and molecular mechanisms of intestinal fibrosis. *World Journal of Gastroenterology : WJG*, *18*(28), 3635. https://doi.org/10.3748/WJG.V18.I28.3635

Stamataki, D., Holder, M., Hodgetts, C., Jeffery, R., Nye, E., Spencer-Dene, B., Winton, D. J., & Lewis, J. (2011). Delta1 Expression, Cell Cycle Exit, and Commitment to a Specific Secretory Fate Coincide within a Few Hours in the Mouse Intestinal Stem Cell System. *PLoS ONE*, *6*(9), e24484. https://doi.org/10.1371/journal.pone.0024484

Stzepourginski, I., Nigro, G., Jacob, J.-M., Dulauroy, S., Sansonetti, P. J., Eberl, G., & Peduto, L. (2017). CD34 + mesenchymal cells are a major component of the intestinal stem cells niche at homeostasis and after injury. *Proceedings of the National Academy of Sciences*, *114*(4), E506–E513. https://doi.org/10.1073/pnas.1620059114

Sun, X., & Kaufman, P. D. (2018). Ki-67: more than a proliferation marker. *Chromosoma*, *127*(2), 175–186. https://doi.org/10.1007/s00412-018-0659-8

Sun, Z.-J., Zhang, Y.-Z., Liu, F., Chen, J.-J., Chen, D.-X., Liu, H.-B., Liang, L., & Han, H. (2018). A fusion protein composed of the DSL domain of Dll1 and RGD motif protects cryptic stem cells in irradiation injury. *Bioscience Reports*, *38*(2). https://doi.org/10.1042/BSR20171255

Taddei, M., Giannoni, E., Fiaschi, T., & Chiarugi, P. (2012). Anoikis: an emerging hallmark in health and diseases. *The Journal of Pathology*, *226*(2), 380–393. https://doi.org/10.1002/path.3000

te Molder, L., de Pereda, J. M., & Sonnenberg, A. (2021). Regulation of hemidesmosome dynamics and cell signaling by integrin α6β4. *Journal of Cell Science*, *134*(18). https://doi.org/10.1242/jcs.259004

Tian, H., Biehs, B., Warming, S., Leong, K. G., Rangell, L., Klein, O. D., & de Sauvage, F. J. (2011). A reserve stem cell population in small intestine renders Lgr5-positive cells dispensable. *Nature*, *478*(7368), 255–259. https://doi.org/10.1038/nature10408

Usunier, B., Brossard, C., L’Homme, B., Linard, C., Benderitter, M., Milliat, F., & Chapel, A. (2021). HGF and TSG-6 Released by Mesenchymal Stem Cells Attenuate Colon Radiation-Induced Fibrosis. *International Journal of Molecular Sciences*, *22*(4), 1790. https://doi.org/10.3390/ijms22041790

van Es, J. H., Wiebrands, K., López-Iglesias, C., van de Wetering, M., Zeinstra, L., van den Born, M., Korving, J., Sasaki, N., Peters, P. J., van Oudenaarden, A., & Clevers, H. (2019). Enteroendocrine and tuft cells support Lgr5 stem cells on Paneth cell depletion. *Proceedings of the National Academy of Sciences*, *116*(52), 26599–26605. https://doi.org/10.1073/pnas.1801888117

VanDussen, K. L., Carulli, A. J., Keeley, T. M., Patel, S. R., Puthoff, B. J., Magness, S. T., Tran, I. T., Maillard, I., Siebel, C., Kolterud, Å., Grosse, A. S., Gumucio, D. L., Ernst, S. A., Tsai, Y. H., Dempsey, P. J., & Samuelson, L. C. (2012). Notch signaling modulates proliferation and differentiation of intestinal crypt base columnar stem cells. *Development*, *139*(3), 488–497. https://doi.org/10.1242/DEV.070763/-/DC1

Wei, Q., & Frenette, P. S. (2018). Niches for Hematopoietic Stem Cells and Their Progeny. *Immunity*, *48*(4), 632–648. https://doi.org/10.1016/j.immuni.2018.03.024

West, A. B., Isaac, C. A., Carboni, J. M., Morrow, J. S., Mooseker, M. S., & Barwick, K. W. (1988). Localization of villin, a cytoskeletal protein specific to microvilli, in human ileum and colon and in colonic neoplasms. *Gastroenterology*, *94*(2), 343–352. https://doi.org/10.1016/0016-5085(88)90421-0

Xi, Y., & Xu, P. (2021). Global colorectal cancer burden in 2020 and projections to 2040. *Translational Oncology*, *14*(10), 101174. https://doi.org/10.1016/j.tranon.2021.101174

Yu, Y., Yang, W., Li, Y., & Cong, Y. (2020). Enteroendocrine Cells: Sensing Gut Microbiota and Regulating Inflammatory Bowel Diseases. *Inflammatory Bowel Diseases*, *26*(1), 11–20. https://doi.org/10.1093/ibd/izz217

Zhang, Y., Dubé, P. E., Washington, M. K., Yan, F., & Polk, D. B. (2012). ErbB2 and ErbB3 regulate recovery from dextran sulfate sodium-induced colitis by promoting mouse colon epithelial cell survival. *Laboratory Investigation*, *92*(3), 437–450. https://doi.org/10.1038/labinvest.2011.192

Zhao, S., Dejanovic, D., Yao, P., Bhilocha, S., Sadler, T., Schirbel, A., West, G., Doyon, G., Lopez, R., Mao, R., Kurada, S., Ouali, S. El, Grassl, G., Fox, P. L., Cruise, M., Worthley, D. L., De La Motte, C., Fiocchi, C., & Rieder, F. (2020). *Selective deletion of MyD88 signaling in Î±-SMA positive cells ameliorates experimental intestinal fibrosis via post-transcriptional regulation*. https://doi.org/10.1038/s41385-020-0259-9

Zhao, Y., Qiao, X., Tan, T. K., Zhao, H., Zhang, Y., Liu, L., Zhang, J., Wang, L., Cao, Q., Wang, Y., Wang, Y., Wang, Y. M., Lee, V. W. S., Alexander, S. I., Harris, D. C. H., & Zheng, G. (2016). Matrix metalloproteinase 9-dependent Notch signaling contributes to kidney fibrosis through peritubular endothelial–mesenchymal transition. *Nephrology Dialysis Transplantation*, gfw308. https://doi.org/10.1093/ndt/gfw308

Zhdanovskaya, N., Firrincieli, M., Lazzari, S., Pace, E., Scribani Rossi, P., Felli, M. P., Talora, C., Screpanti, I., & Palermo, R. (2021). Targeting Notch to Maximize Chemotherapeutic Benefits: Rationale, Advanced Strategies, and Future Perspectives. *Cancers*, *13*(20), 5106. https://doi.org/10.3390/cancers13205106